Multi-proxy Evidence of Southward Migration of the Intertropical Convergence Zone During Heinrich Stadial 1

A Thesis

SUBMITTED TO THE FACULTY OF

UNIVERSITY OF MINNESOTA

BY

Wyatt K. Hansen

IN PARTIAL FULFILLMENT OF THE REQUIREMENTS

FOR THE DEGREE OF

MASTER OF SCIENCE

Advisor: R. Lawrence Edwards

August 2023

University of Minnesota, Twin Cities

Acknowledgments

I owe many people my gratitude for their guidance and support during the last two years; without them, my research and thesis would not exist. First, thanks to everyone who reviewed my thesis; your feedback was essential to the quality of this paper. Thanks to my committee members, Dr. Joshua Feinberg, and Dr. Xinyuan Zheng. Thanks to Dr. Peter Chutcharavan and Dr. Plinio Jaqueto for their paper recommendations and mentorship. Thanks to Dr. Katee Wendt for her initial work and vital feedback on my project. Thanks to Dr. Nicolás Stríkis for hosting me in Brazil, taking me to outstanding sites, and teaching me the fundamentals of cave fieldwork. Thanks to Dr. Yuval Burstyn for his expertise, time, and help in acquiring my trace element data and its analysis. A huge thanks to Dylan Parmenter, for his continuous encouragement, friendship, and advice. Lastly, I would like to thank my advisor, Dr. Larry Edwards, for his guidance and patience in my academic development.

Dedication

This thesis is dedicated to Alexis, my cats, and my family.

Abstract:

Heinrich event 1 (H1) and its associated stadial period (HS1) resulted in an aridification in the northern hemisphere subtropics and wetter conditions in the Southern Hemisphere subtropics (Deplazes et al.,2013; Wang et al., 2001). Pluvial periods in Northeast (NE) Brazil (Auler et al., 2004) associated with Heinrich Stadials are characterized by a two-phased increase in rainfall amount and a transition to a wetter and more diverse vegetation regime (Dupont et al., 2010) attributed to a southward shift of the Intertropical Convergence Zone (ITCZ). This two-phased structure is well documented from palynological and sediment core records but lacks the high-precision dating required to fully understand the exact timing and duration of the pluvial period. This issue is shared with IPCC models which have a difficult time characterizing the precipitation response in the tropics to modern climate change. By fully understanding past pluvial responses to climate forcings, climate models and mitigation strategies can be improved.

Heinrich tuned growth intervals of speleothems in Toca da Barriguda cave in NE Brazil capture past pluvial periods. This study presents the U-Th dated speleothem record, TBR-14, from Toca Da Barriguda in NE Brail during HS1. The main growth interval of TBR-14 extended from 17,029 ±76 years B.P. (before 1950 A.D.) to 15,850 ±90 years B.P. The record consists of oxygen isotopes ($\delta^{18}O$), trace elements, and confocal fluorescence during the pluvial period. The resulting record reveals the timing and structure of the NE Brazil pluvial anomaly associated with HS1 at an unprecedented resolution and precision. $\delta^{18}O$ displays a two-phased shift in values

related to the latitudinal range of the ITCZ. The oxygen isotope structure is characterized by an initial wet period lasting until 16,166 ± 61 years B.P (-4 to -6 ‰ δ^{18}O), followed by a wetter period ending at 15,850 ± 90 years B.P (-6 to -8 ‰ δ^{18}O).

The onset of the wetter period occurred abruptly with a dramatic drop in δ^{18}O (~1.4‰) in two years. The fluorescent banding structure, prior calcite precipitation (PCP) indices, and phosphorus/calcium (P/Ca) ratios indicate that the transition resulted in the wettest period of NE Brazil during HS1. The isotopic drop occurs, within error, at the same time and rate that China shifts abruptly to a drier climate (Treble et al., 2007). On a broader timescale, PCP indices, P/Ca, and confocal banding depict decreased aridity and precipitation changes. These changes are consistent with the ecological bridge hypothesis, which attributes vegetational changes recorded in regional records for the cause of periodic species exchange between the Atlantic and Amazon Rainforests.

Contents:

Abstract:.....iii
List of Figures vii
Introduction:.....1
Paleoclimatic Significance of TBR-14:.....1
Study Area:.....3
Modern day climate/vegetation:.....7
Background:.....9
Heinrich Events:.....9
Mechanisms:.....14
Impacts of H1:.....19
ITCZ During Heinrich Stadials:.....24
δ18O:.....26
Trace Elements:.....29
Confocal Banding:.....35
Uranium – Thorium Dating:.....38
Methods:.....41
U-Th Dating:.....41
Age Depth Model:.....44
Oxygen and Carbon Isotopes:.....44
Confocal Image Acquisition:.....45
Confocal Band Counting:.....49
Trace Metals:.....50
Results:.....55
U-Th Dating:.....55
Oxygen Isotopes:.....56
Trace Elements:.....57
Fluorescence and Phosphorus:.....61
Band Counting:.....66
Discussion:.....67
Movement of the ITCZ Inferred From $\delta^{18}O$ (Comparison with other records).....67
Section 1:.....76

Bright Confocal Growth Package: 78
Section 3: 82
16.1 ka BP event: 85
Conclusion: 90
References: 93
Supplementary Figures: 102

List of Figures

1. Plan view of TBV and TBR cave....4
2. Monthly average temperature and precipitation values for Petrolina, NE Brazil....7
3. Biomes of Northeast Brazil and the surrounding area....9
4. Detrital carbonate present in marine sediment cores in the North Atlantic....11
5. Marine ice cliff instability model....18
6. NE Brazil speleothem growth periods compared to global records....20
7. $\delta^{18}O$ as a function of ITCZ proximity in South America....29
8. Conceptual model of PCP....33
9. Oxygen isotopes from TBV-40 in NE Brazil during HS4....37
10. Conceptual graph of disequilibrium dating....40
11. TBR-14 sample sections for trace metal analysis....53
12. Oxcal age-depth model....55
13. *$\delta^{18}O$ values of TBR-14*....*57*
14. TBR-14 *Ba/Ca, Sr/Ca, and Mg/Ca values throughout the main growth period*....*58*
15. *Confocal image of pluvial transition*....*63*
16. *Fluorescent band intensity and phosphorous concentrations*....*64*
17. *$\delta^{18}O$, Ba/Ca, and P/Ca during pluvial transition*....*65*
18. Comparison of marine core GeoB3910-2 and speleothem record....71
19. Comparison of TBR-14 to Chinese and South American records....74
20. TBR-14 dataset synopsis....75
21. Oxygen isotope drop with confocal overlay....81

List of supplemental figures:

1. *Ceiling rock pendants in TBR cave*....*102*
2. *Example of WICOUNT*....*103*
3. Trace metal concentrations throughout the whole record....104
4. *Fluorescent band intensity and phosphorous throughout the whole record*....*105*
5. Example of speleothem growth hiatus....106
6. Example of annual signal loss in confocal fluorescence....107
7. Confocal fluorescence scan of TBR-14 HS1 record....108
8. Example of PCA....109

List of Tables and Equations:

Tables:

Table 1: *Uranium-Thorium dating results of TBR-14*……....54

Table 2: *Brightness, P, Ba/Ca, Sr/Ca, and Mg/Ca ratios*……..*60*

Table 3: Bands counted compared to U/Th based age model……*66*

Equations:

Equation 1: Definition of $\delta^{18}O$……..….*26*

Equation 2: Counting Statistics……*38*

Equation 3: U-Th Age Calculation……*41*

Equation 4: Sample Size for U-Th Dating……..*42*

Introduction:

Paleoclimatic Significance of TBR-14:

Heinrich stadial 1 (HS1,14.5-17.5 ka BP), a millennial-scale climatic event characterized by a weak Atlantic Meridional Overturning Circulation (AMOC) system, extreme atmospheric cooling, and the reorganization of atmospheric circulation, had far-reaching consequences for global climate. These impacts were exacerbated during Heinrich event 1, an episode that occurred during the Henrich stadial which was marked by mass iceberg discharge into the North Atlantic. In paleoclimate records from across the globe, the consequences of the stadial and event manifest as a two-phased shift in climate, with the northern subtropics becoming drier and the southern subtropics becoming wetter (Wang et al., 2001; Broecker et al., 2009; Wang et al., 2004). The weakening of the East Asian summer monsoon system (EASM) and the displacement of the ITCZ southwards towards Northeast (NE) Brazil are two of the most prominent examples. During Heinrich stadials, the two regions experienced climate change simultaneously through a climate teleconnection. By investigating this teleconnection, the inner workings of the global climate system response to HS1 climatic forcings can be better understood.

Speleothem records from across China display a two-phased shift to a weaker monsoon and drier climate through a 2‰ increase in $\delta^{18}O$ at ~16.07 ka BP (Wang et al., 2001; Liang et al., 2020). Secondary Ionization Mass Spectrometry (SIMS) analysis of

the YT speleothem record from Hulu Cave determined that the main shift occurred over 6 years with the majority of it occurring over just 2 years (Treble et al., 2007). The rate of precipitation changes documented in the YT speleothem record is unprecedented in paleoclimatology and can serve as a valuable analogue for how modern-day climate change may alter monsoon intensity or tropical precipitation. The isotopic shift has been observed in other Chinese speleothem records, but the two-year shift detected in YT cannot be quantified in those records due to the lack of sub-decadal temporal resolution.

This study presents an absolutely dated U-Th speleothem paleoclimate record spanning HS1 for a stalagmite (TBR-14) from Toca da Barriguda in NE Brazil. The $\delta^{18}O$ record of TBR-14 has a two-phased structure and isotopic shift that is opposite of the structure shown in Chinese records. TBR-14 has a high growth rate (~180 um/year) and distinct fluorescent banding which, when combined with precise uranium-thorium (U-Th) dates, can provide sub-annual resolution around the oxygen isotopic shift. By leveraging the climactic teleconnection between China and NE Brazil, I will use this record to test if the findings of Treble et al. (2007) are applicable throughout the tropics and determine if the 16.07 ka BP $\delta^{18}O$ excursion represents a global event.

NE Brazil is a region of particular interest for ecological and biological study, as it may have served as a bridge for plant and animal species exchange between the Amazon and Atlantic Rainforest during HS1 (Arz et al., 1999; Costa et al., 2003; Dupont et al., 2010). The U-Th dated TBR-14 oxygen isotope record can be used to constrain the timing and duration of the precipitation changes necessary for tropical species

exchange. Trace elements and confocal fluorescence banding can bolster climate interpretations by providing point source accounts of changes in aridity, climate, and soil organic matter (SOM) transport. Overall, the TBR-14 multi-proxy record can provide a comprehensive understanding of climate change in NE Brazil supportive of the ecological bridge hypothesis.

Study Area:

This study investigates the stalagmite sample TBR-14 from Toca da Barriguda Cave (TBR), located at (10°08′26″S, 40°51′08″W), 13 km east of the village of Laje Dos Negros in the northern section of Bahia state, Northeast Brazil (Figure 3). TBR is part of the Precambrian São Francisco Craton. The geology of the cave entrance is dolomitic carbonate, which consists of the Salitre formation from the Una group (Klimchouk et al., 2016). Currently, 34 km of TBR has been mapped, making it one of the longest caves in the Southern Hemisphere. TBR is adjacent to Toca da Boa Vista (TBV), the longest cave in the Southern Hemisphere, with over 125 km mapped (Figure 1). TBR may be connected to TBV due to its proximity but this connection has not been established (Auler & Smart, 2003).

Speleogenesis, the process of cave formation, is important to understand for cave-based research. Unlike epigenic caves, which form from the intrusion of surface waters, TBR is a hypogenic cave formed from acidic waters and gases that originate below the surface (Auler & Smart 2003). In epigenic caves, passages often mimic surface topography. The hypogenic nature of TBR is evident by the stark contrast

between the cave's intricate network of passageways and the flat, monotonous terrain of the surface (Auler & Smart, 2003). The absence of fluvial features on the walls, the labyrinth-like layout of TBR, ceiling rock pendants (Supplemental Figure 1), and sharp height variability between passages and chambers support a hypogenic origin for TBR speleogenesis.

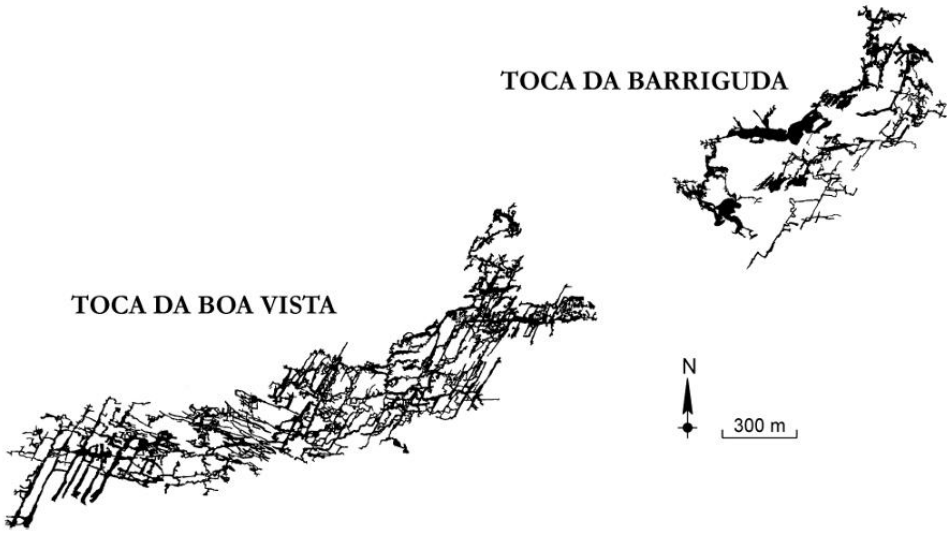

Figure 1: Plan view of TBV and TBR cave. Survey by Grupo Bambui de Pesquisas Espeleologicas (Auler & Smart, 2003).

The hypogenic process of TBR's formation has been debated between shallow cave and deep-seated hypogenic speleogenesis. Shallow cave hypogenic speleogenesis does not need to occur at depth; while deep-seated hypogenic caves form through the upwelling of acidic groundwater from below the cave surface (Klimchuk et al., 2000). Deep-seated hypogenic caves have three-dimensional architecture and are often related to tectonic activity (Auler and Smart, 2003). Given the

lack of tectonic activity and the apparent absence of three-dimensional cave features and ascending passages, Auler and Smart (2003) determined that TBR was formed through shallow-cave hypogenic processes, where cave development occurred as oxic surface water interacted with sulfide-bearing pyrite and was incorporated into a laterally flowing aquifer. Cave development in this situation would be horizontally limited by the distribution of sulfide beds and vertically limited by the extent of oxic water. TBR's passage network appeared to conform to this distribution system, supporting the theory that the cave developed through shallow hypogenic cave formation.

Continued research of TBR led to evidence against the cave having shallow cave hypogenic speleogenesis and in favor of the cave having a deep-seated hypogenic origin. Originally, this process seemed unlikely to be the origin of TBR due to the region's long-term tectonic inactivity. The last two tectonic periods the region experienced were during the Cambrian tectonothermal event and the breakup of Pangea (Klimchouk et al., 2016). As these events occurred 520 and 200 Ma (million years ago) respectively, TBR and TBV could be the oldest caves in the world if the caves did in fact form through deep-seated hypogenic speleogenesis. Further investigation of TBR revealed the presence of numerous vertical passageways that serve as conduits for fluid migration known as feeders. These feeders act as a diagnostic features of deep-seated hypogenic cave formation (Klimchouk et al., 2016). The feeders had been overlooked in preliminary studies, as they are infilled with sediment and not easily visible. TBR and TBV were also found to have a three-dimensional architecture, with three stratigraphic stories recognized in TBV and two in

TBR. The discovery of this three-dimensional architecture and vertical feeder conduits signifies that, deep-seated hypogenic speleogenesis is the most likely mechanism for TBR's cave development.

When selecting a cave for paleoclimatic research, the climate potential of samples should be considered. Rapid climate events and hydrological change are more clearly captured in shallow cave systems and are therefore ideal for studying millennial-scale events such as Heinrich Events (Fairchild & Treble, 2009; Cruz et al., 2005; Tan et al., 2006). TBR is a shallow cave system reaching a max depth of 60m. TBR-14 lies at a depth of only 30m, so it is particularly sensitive to climatic change. This characteristic makes TBR-14 an ideal candidate for studying rapid climate events and hydrological change.

Modern day climate/vegetation:

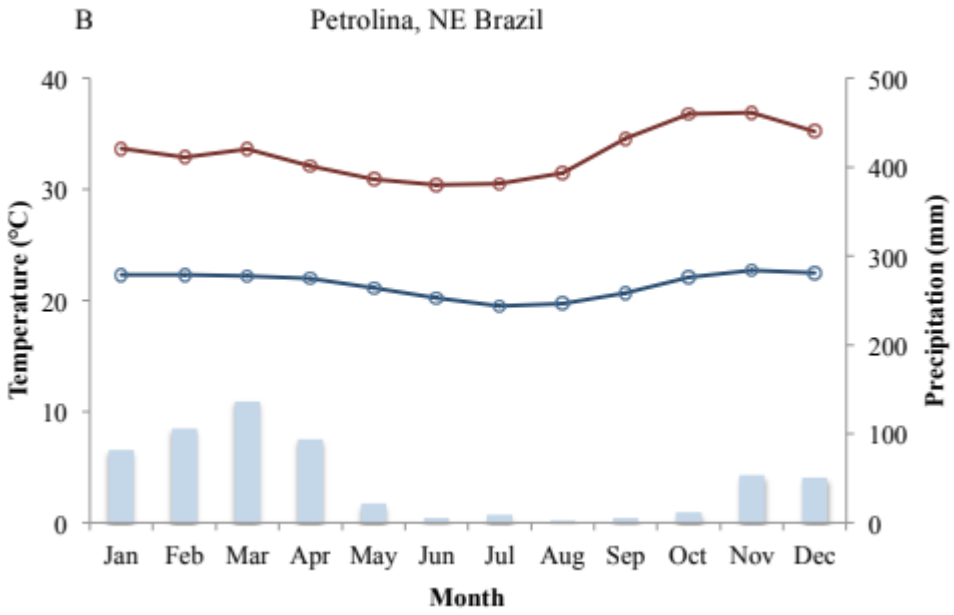

Figure 2: Monthly average temperature and precipitation values for Petrolina, NE Brazil. Monthly average temperature highs (red) and lows (blue) are shown with monthly precipitation (bars) for Petrolina, NE Brazil. Petrolina is 120 km North of the cave site. Data was collected from 1961-1990 by the Instituto Nacional de Meteorologia (INMET) of Brazil (http://www.inmet.gov.br/portal/). Figure taken from (Wendt, 2015 thesis)

The interior of NE Brazil, located ~500 Km from the coast, has an annual temperature of 28℃ and receives around 490 mm of rainfall annually (Auler et al., 1999). The region is semiarid with low rainfall and high evapotranspiration rates (~1400 mm/year). Climate models predict that droughts will become longer, more frequent, and more intense (Marengo et al., 2017). Rainfall in NE Brazil is seasonally limited, with a long dry season and a narrow wet season (figure 2, Wendt, 2015). From May to October, the dry season produces virtually no rainfall (<50 mm). The wet season lasts

from November to April, with most rainfall occurring between January and April. March is typically the rainiest month.

Interannual rainfall in NE Brazil is highly variable, with as much as a 40% difference observed between wet and dry years (Cadier, 1996). The high rainfall variability of the region is related to changes in the mean position of the ITCZ (Hastenrath & Heller, 1977; RouCou et al., 1996). Cross-equatorial sea surface temperature (SST) and the strength of the northeasterly winds change the mean position of the ITCZ. The ITCZ does not currently reach the cave site, but precipitation is enhanced when the ITCZ is closest to the site. Wet years occur when the northeast trade winds strengthen and a positive SST anomaly exists south of the equator, resulting in a southward displaced ITCZ (Hastenrath, 1990). Conversely, dry years are the result of weaker northeast trade winds and warmer SST north of the equator. The high interannual variability and aridity of NE Brazil contributes to its distinct vegetation.

The modern vegetation of NE Brazil is dominated by Caatinga, a biome characterized by an abundance of xerophytic, deciduous, thorny scrub-brush, and dry forests (Leal et al., 2005). Caatinga occupies a region of 735,000 km^2 and separates the Amazon rainforest to the North from the Atlantic rainforest to the South (figure 3). To the Southwest of the Caatinga region lies the Cerrado Savannah. In the past, an ecological bridge of wetter vegetation may have existed in the Caatinga or Cerrado ecosystems to connect the Atlantic and Amazon forests. The Caatinga biome is well adapted to dry conditions but is becoming increasingly fragmented and diminished due to habitat loss (Leal et al., 2005) and climate change (De Oliveira et al., 2012).

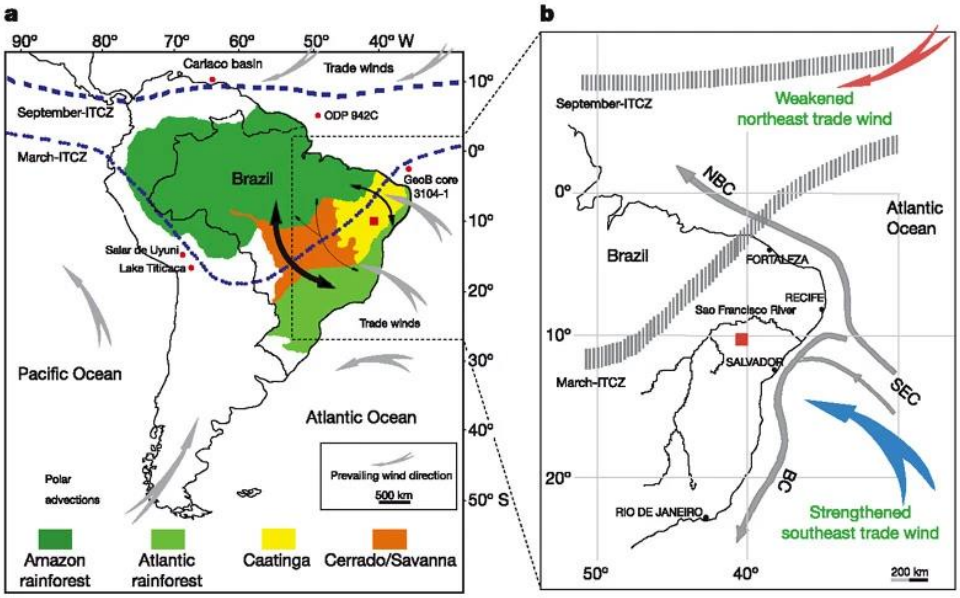

Figure 3: A) Biomes of Northeast Brazil and the surrounding area. Caatinga (yellow), Cerrado (orange) Atlantic rainforest (light green), and Amazon rainforest (dark Green). B)TBR (red square) (Wang et al., 2004).

Background:

Heinrich Events:

Heinrich events are millennial-scale climatic events characterized by the mass export of icebergs into the North Atlantic, resulting in global changes in atmospheric circulation and climate. Hartmut Heinrich first proposed cyclical mass iceberg discharge based on his findings from the Dreizack Seamounts, underwater hills located in the Northeast Atlantic. Heinrich chose this area for study as the hills are not influenced by dissolution or turbidite sediment; additionally, at a latitude of 47°23' N, the location is sensitive to both warm and cold excursions with only the strongest pulses of ice rafting capable of being recorded (Heinrich, 1988).

The most apparent evidence of previous sea ice cover is ice-rafted debris (IRD). The term IRD describes sediment that was transported at the bottom of icebergs and later deposited when the icebergs melted. These deposits consist of sediment larger than 150 μm. IRD is easily distinguishable, as sediment in distal source deep ocean deposits are typically fine-grained and much smaller. Colder surface waters would likely coincide with increased ice rafting, signifying an expected increase in the representation of Neogloboquadrina pachyderma (*N. pachyderma*) foraminifera, which are a proxy for polar water temperature. The Dreizack sediment cores revealed six quasi-cyclical peaks of lithic IRD deposits concurrently with peaks of *N. pachyderma* (Heinrich, 1988). Each peak represents a Heinrich event, with the most recent being Heinrich event 1 (H1). These peaks, relatively dated with oxygen isotope stratigraphy, represented times of maximum ice rafting and had an apparent influence by orbital precession as the periodicity of the peaks was ~11,000 years, half the length of a processional cycle (Heinrich, 1988).

Investigation of other North Atlantic Ocean sediment cores, particularly DSDP Site 609, provided additional insights into Heinrich events source and features. In addition to the matching peaks of IRD and N. pachyderma, similar to the Dreizack cores, the other North Atlantic cores revealed that the lithic fragment layers are rich in high-density detrital carbonates and low in total foraminifera count, with a westward increase in IRD in the cores (figure 4, Bond et al., 1992). The westward increase in detrital carbonate indicates Eastern Canada as the sediment source since the region is filled with dolostone and limestone and lies in the trajectory indicated by the sediment

pattern (Bond et al., 1992). Hematite-stained grains and Icelandic glass found coincident with detrital carbonate indicate multiple sources may have been contributing to Heinrich IRD layers, such as East Greenland and Iceland (Bond & Lotti, 1995). Magnetic susceptibility of the detrital carbonate grains and several radiometric-based provenance studies suggest Hudson Straight, Baffin Bay, and areas along the Labrador Sea as the primary sources for IRD (Hemming, 2004).

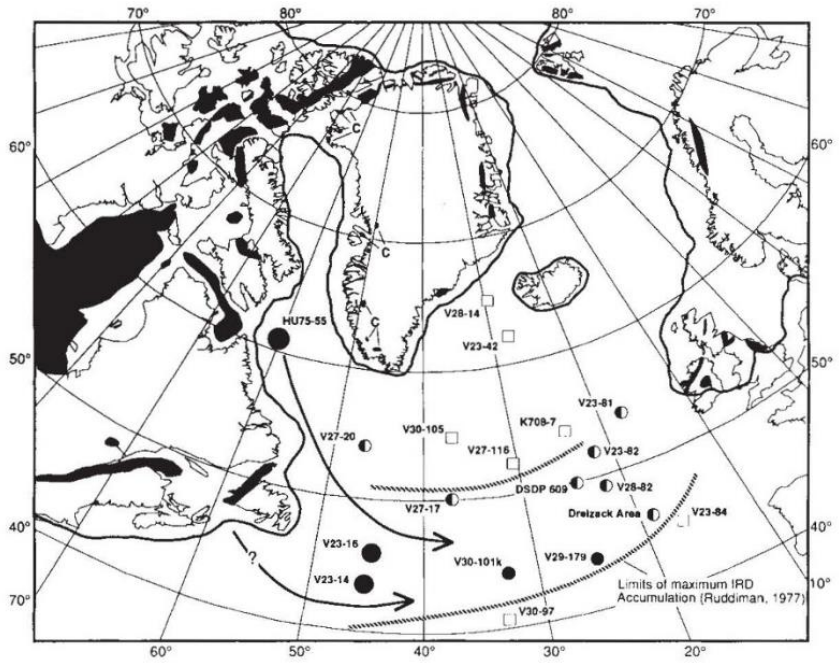

Figure 4: Heinrich layers are present in all cores depicted. Circles signify that the IRD in the core was rich in carbonate IRD. A full circle indicates that every Heinrich layer had carbonate rich IRD while a half-filled circle means that some layers were absent of IRD (Bond et al., 1992).

The low foraminifera count of DSDP site 609 could suggest an alternative narrative of Heinrich events, where instead of times of high IRD, they represent periods of low foraminifera flux (Broecker et al., 1992). This narrative does not counter the idea of Heinrich events, as the mass export of icebergs would result in a less saline and colder surface ocean leading to fewer foraminifera (Broecker et al., 1992). N.

pachyderma found buffering the Heinrich layers suggest the water was cold even before the Heinrich event. Since the North Atlantic is a crucial area for AMOC, a less saline North Atlantic would prevent North Atlantic Deep Water (NADW) formation and could slow down or shut down AMOC, a possible component indicating how Heinrich events led to global climate change.

Continued investigation of Heinrich layers led to evidence that the original periodicity of the events was incorrect. Each Heinrich layer was radiocarbon dated at DSDP 609, revealing inconsistent intervals of ~5-10,000 years between each event (Bond et al., 1992). As these intervals are much smaller than Milankovitch orbital periodicity, it is unlikely that the events are strongly influenced by the cycle (Bond et al., 1992). The IRD and foraminifera records for the North Atlantic cores coincide with particularly cold temperatures reflected in the Greenland Ice core Project (GRIP) $\delta^{18}O$ ice core record. The intervals between events and correspondence between the IRD record and Greenland ice core temperatures instead suggest Heinrich events are related to Dansgaard-Oeschger cycles (D-O). D-O cycles are notable climate proxies due to the abrupt warming recorded in Greenland ice. The cycles have a periodicity of ~1,600 years and are sawtooth in shape, representing rapid warming and gradual cooling (Bond et al., 1993). This warming happened on a scale of years to decades and could result in over 10 degrees Celsius of warming (Schulz, 2002). Interstadial refers to the period of a D-O event with abrupt warming, and stadial refers to the period of a D-O with gradual cooling. Heinrich events do not occur during every D-O cycle. Bond et al. (1993) noted an intracycle trend between D-O events where the interstadial and stadial

became colder with each progressive cycle. At the coldest stadial of the intra-D-O cycle, a Heinrich event occurs followed by a warmer D-O cycle. H1 did not occur at the end of a bundled DO cycle (Bond et al., 1992). The Bond cycle, the intra-DO cycle, demonstrates that Heinrich events take place during times of extreme atmospheric cooling (Bond et al., 1993).

Heinrich event 3 (H3) and Heinrich event 6 (H6) are markedly different from the other events. H3 and H6 have higher than background IRD concentrations, but unlike the other events, they are not rich in detrital carbonate and contain fewer lithic fragments (Bond et al., 1992). H3 and H6 have lower fluxes of IRD and H3 has lower magnetic susceptibility compared to the other events (Hemming, 2004). These discrepancies could either result from the events having a different iceberg source or suggest that H3 and H6 were not actual iceberg expulsion events, but instead were periods of reduced foraminifera production (Hemming, 2004).

Changes in ocean circulation are an essential component of Heinrich events, but initially their relationship to Heinrich events was unclear. The prevailing thought was that iceberg rafting would freshen surface salinity, disrupting thermohaline circulation and shutting down the AMOC system. Using $\delta^{13}C$ and $\delta^{18}O$ from benthic and planktonic foraminifera in two North Atlantic cores, Vidal (1997) characterized changes in deep-water convection and surface temperature before, during, and after Heinrich event 4 (H4). Vidal found a precursor slowdown of AMOC beforehand and that deep convection in the North Atlantic stopped during the event, where a greater proportion of benthic foraminifera were represented by a southern deep-water signal.

The precursor slowdown of AMOC found in Vidal's work brought into question the role of ice rafting in AMOC changes. Mcmanus et al. (1999) examined climate variability and sea surface changes across the last 500 Ka and five glacial cycles through $\delta^{18}O$ and IRD deposits in the North Atlantic. This work showed that there is greater climate variability during glacial cycles, but AMOC variability still exists during interglacial cycles. Interglacial AMOC strength changes indicate that ice rafting cannot be the initial driver of variability but could serve as a positive feedback loop that amplifies climate variability. Modeling of ocean currents illustrated that a weakened AMOC signal leads to reduced convection of North Atlantic waters resulting in intermediate waters warming (Shaffer et al., 2004). Mg/Ca ratios, a proxy for ocean temperatures, of benthic foraminifera representative of intermediate waters in the Northwest Atlantic provide evidence of subsurface warming prior to the Heinrich event (Marcott et al., 2011). Subsurface warming could trigger ice shelf collapse, signifying that AMOC strength changes lead to ice rafting as opposed to ice rafting resulting in changes in AMOC intensity.

Mechanisms:

MacAyeal (1993) proposed the first significant mechanism for Heinrich events. This mechanism postulated that Heinrich events were caused by internal ice sheet dynamics of the Laurentide ice sheet (LIS), not climatic change. The Binge-Purge mechanism refers to the change in the mass of the Laurentide throughout a cycle. During the binge phase, the Hudson Bay sediment bed is frozen, preventing the LIS

from moving or notable amounts of icebergs from forming. The Laurentide slowly accumulates mass according to the snow accumulation rate during this phase. The purge phase is the Heinrich event, where the Laurentide rapidly diminishes in size due to the calving of icebergs into the Hudson Strait. The purge phase triggers when the ice sheet reaches a thickness that allows for the basal temperature of the ice sheet to be at melting point (MacAyeal, 1993). At the melting point, an ice stream develops as the basal sediments thaw and act as a lubricant, causing a Heinrich event to occur. The mass calving of icebergs leads to a greatly reduced thickness of the Laurentide, which reduces the ice sheet's insulating capacity, freezes the sediment bed, and restarts the cycle.

A vital concept of the Binge-Purge model is that it functions independently of climatic change. In this model, warm interstadials only follow a Heinrich Event due to the size of the Laurentide passing a threshold where it can no longer impact atmospheric circulation. The size of the Laurentide only forces climate; it is not impacted by climatic forcing. The apparent connection of Heinrich events to D-O events through Bond cycles refutes the notion of a mechanism independent of climate forcing. Precursor changes to the strength of AMOC further refute the notion of a climate-independent mechanism. AMOC strength changes likely play a role in the thawing of basal sediments of the Laurentide as ocean temperatures react to diminished ocean current circulation of the North Atlantic. If Heinrich events were independent of climate, IRD deposits should only be a function of Hudson Bay discharge. However, Basaltic glass and hematite-stained grains precede the Hudson Bay-sourced carbonate grain

deposits. Bond and Lotti (1995) pinpointed Iceland as the source of the basaltic glass and found the Gulf of St. Lawrence to be the major source of hematite-stained grains. Additionally, Bard et al. (2000) found that H1 had two main pulses of IRD at 16.0 and 17.5 ka BP. If the Binge-Purge model was correct, there should only be a single pulse of IRD when the Laurentide collapses. Therefore, it is unlikely that Heinrich events are independent of climate.

The 7,000-year periodicity of a LIS binge-purge cycle found in MacAyeal's 1993 model serves as the foundational evidence for the Binge Purge Model, roughly equivalent to the periodicity of Heinrich Events. This foundational evidence is weakened when H3 and H6 are considered. If H3 and H6 were not iceberg rafting events but instead periods of diminished foraminifera, the importance of the periodicity of the model weakens. If H3 and H6 were iceberg rafting events formed from other sources, the periodicity of the model is not significant. For these reasons, the Binge-Purge model is unlikely to be an accurate mechanism behind Heinrich events.

Delivery of IRD through an ice shelf in the Labrador Sea was the next prominent Heinrich event mechanism proposed. During a Heinrich stadial, an ice shelf builds in the Labrador Sea. As the ice shelf builds, it accumulates carbonate debris from Hudson Strait ice, while the process of underplating adds a protective layer to the debris (Hulbe, 1997). Underplating occurs as relatively warm, buoyant water melts the bottom of the ice shelf and rises along the side of the ice shelf. As the water travels alongside the bottom of the iceberg, it cools and freezes onto the ice shelf. This process results in some debris depositing at the ice shelf origin but also leads to debris-free ice

accumulating over the ice that contains debris. When the ice shelf breaks off and becomes an iceberg, the debris entrapped in the iceberg will be deposited further from its source as the underplated ice melts before the debris-laden layer (Hulbe, 1997). The strengths of this mechanism are that it relies on external climate forcing and provides an explanation for increased IRD survivability to create Heinrich layers. Flaws with this model lie in the lack of carbonate deposits within the Labrador Sea in addition to the fact that it would require 1000 years of continuous IRD delivery to create the Heinrich layers (Hulbe, 1997).

After the breakup of the Antarctic Larson A and B ice sheets in 2002, Hulbe et al. (2004) revisited the ice shelf mechanism and evoked catastrophic ice shelf collapse as being the IRD mechanism rather than a long steady supply of IRD. The revised mechanism does not use underplating to describe increased IRD survival but instead proposes that capsized icebergs created during an ice shelf breakup would have a similar effect. Catastrophic ice shelf collapse occurs in a climate context where mean temperatures are below freezing but summer air temperatures are around freezing point. In this climate context, meltwater builds on the ice sheet's surface during the summer and infills crevasses. As the water fills crevasses, it expands and propagates the crevasses. When the crevasses reach the bottom of the ice sheet, the ice breaks. Broken ice segments flip onto their sides due to changes in their center of gravity. The entrapped sediment originally on the bottom of the ice sheet occupies all levels of the iceberg resulting in increased survivability of the sediment at the top of the iceberg and continuous deposition of ice throughout the iceberg's path. A challenge with Hulbe’s

revised mechanism is that it requires surface melting from atmospheric warming during a period of pronounced atmospheric cooling.

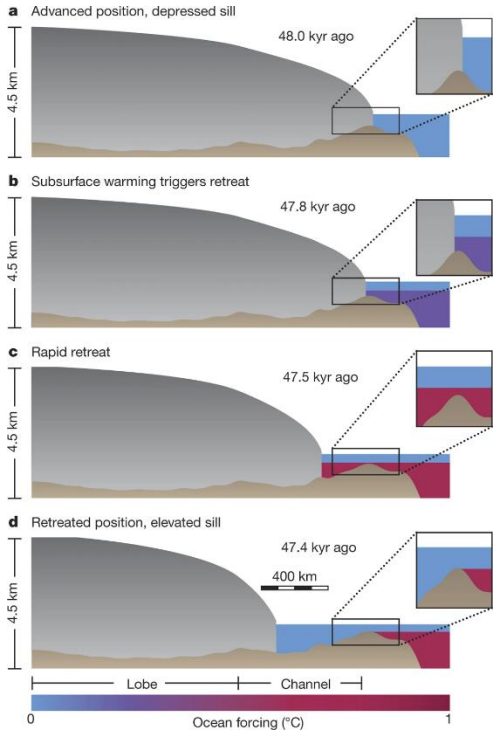

Figure 5: Marine ice cliff instability model (Bassis et al., 2017)

The most robust Heinrich mechanism was proposed by Bassis et al. (2017) following the breakup of Greenland ice shelves. The marine ice cliff instability model (figure 5) improves other proposed mechanisms, as it does not require atmospheric warming and is tied to external climate forcings. The mechanism is based on the interplay between subsurface ocean warming, water depth, and isostatic rebound. During the cold stadial, the ice sheet is at its furthest extent and positioned at a glacial sill that minimizes water depth. Before the Heinrich event, a weakened or halted AMOC causes subsurface warming of intermediate waters (Shaffer et al., 2004). Warmer subsurface ocean temperatures melt the ice sheet's base at the sill, resulting in glacial

retreat. As the ice sheet retreats away from the sill, it is exposed to deeper water which further increases the rate of retreat. With the ice sheet gone, the glacial sill is released from the gravitational weight of the ice, and its elevation rises from isostatic rebound. Through time, the sill rebounds high enough that it isolates the ice sheet from the warmer waters, halting ice shelf retreat and stopping ice rafting.

Impacts of H1:

Heinrich events, the ice rafting episodes, and their associated stadials, the cold period that contains the Heinrich event, are excellent analogues to modern-day climate change in that they are periods with both rapid and global climate change. The rapid and global climate change during HS1 was perpetuated through a large-scale reorganization of atmospheric circulation. Impacts from shifting atmospheric circulation caused by Heinrich Stadial cold anomalies in the North Atlantic are seen worldwide (figure 6). Tropical Hydroclimatic Events (THEs) are common manifestations of these impacts and describe dramatic changes in rainfall in the tropics and subtropics (Bradley & Diaz, 2021). During Heinrich stadial 1 (HS1), the Chinese monsoon became weaker, precipitation increased over the Flores Sea, Borneo became drier, the American southwest became wetter, and northern South America became drier while Northeast Brazil became wetter (Wang et al., 2001; Muller et al., 2012; Partin et al., 2007; Broecker et al., 2009; Wang et al., 2004). High-resolution records across the globe display a two-phased structure of HS1 with a transition around ~16.1 ka (Broecker & Putnam, 2012). Observations of shared timing of peak climatic change in globally distributed records highlight the interconnected teleconnections on Earth. They can

provide insight into some of the inner workings of atmospheric circulation patterns that govern climate.

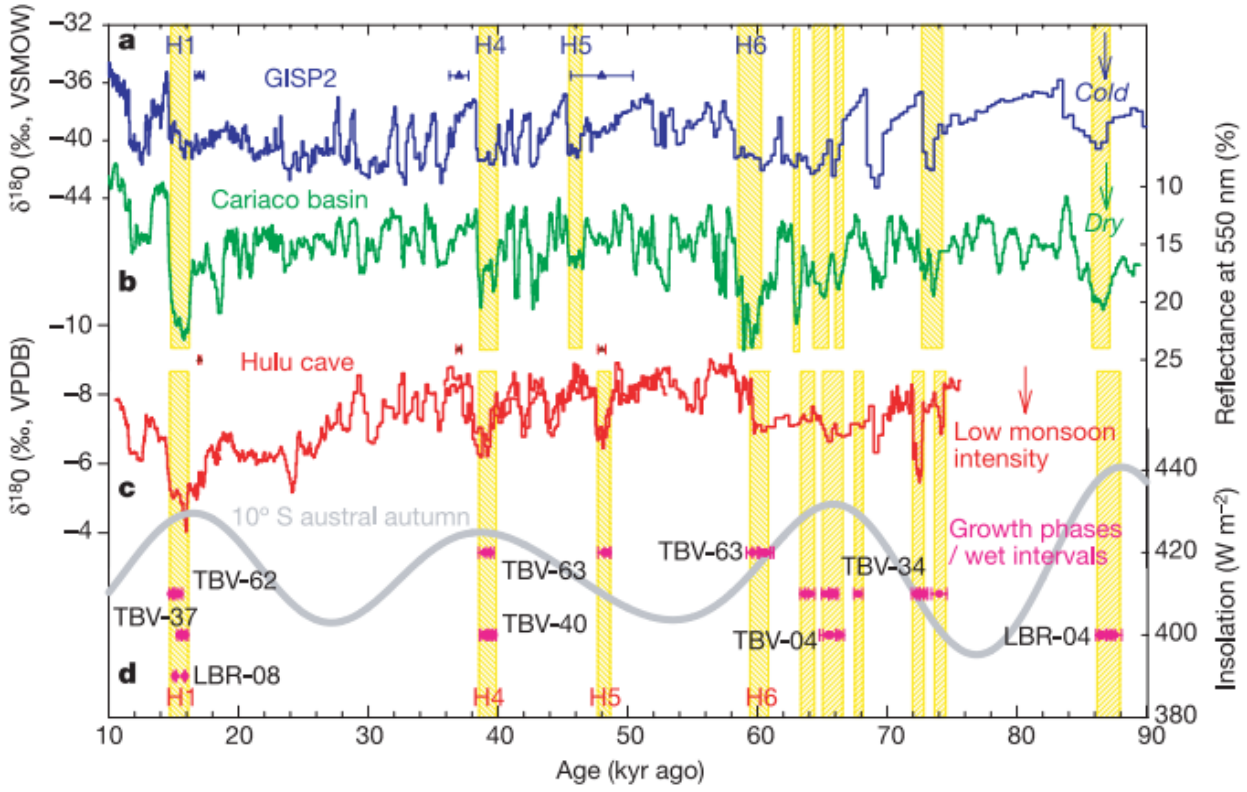

Figure 6: North Atlantic cold anomalies during Heinrich stadials (a) coincide with a drier Cariaco basin (b), weaker monsoon (c), and speleothem growth periods in NE Brazil (d) (Wang et al., 2004).

During HS1, Eastern China experienced rapid climate change, indicated by speleothem records across China. These records document a shift from lighter to heavier $\delta^{18}O$ values (Liang et al., 2020) reflecting changes in monsoon intensity with heavier values relating to a weaker East Asian Summer Monsoon (EASM) system and a more arid climate (Cheng et al., 2016). Hulu cave is the most notable record and is exceptionally dated. Wang et al. (2001) originally dated the record and documented a 2 ‰ increase in $\delta^{18}O$ at 16.07 ± 0.06 ka, representing the largest shift in the Hulu cave

record. This shift was exceptionally fast and could have occurred in as little as two years (Treble et al., 2007).

In the Indo-Pacific, a region affected by the ITCZ, climate change during HS1 occurred in two distinct ways with the north becoming drier and the south becoming wetter (Huang et al., 2019). The northern section of the Sunda Shelf saw decreased precipitation. $\delta^{18}O$ records from Borneo stalagmites document heavier (drier) values during HS1 and driest conditions at 16.3 ± .3 ka BP, coincident with the dry shift in China (Partin et al., 2007). These conditions are further documented in the gravity core, CG2, in the South China Sea. The gravity core, positioned at the mouth of a paleo-river that existed when the Sunda Shelf was exposed, shows higher terrigenous input prior to the shift recorded in China compared to after (Huang et al., 2019). The southern Indo-Pacific experienced opposite climate conditions compared to the northern section during HS1; this observation is recorded in sediment core VM33-80 in the Flores Sea (Muller et al., 2012). The Flores Sea had a higher input of detrital material during the second half of HS1 compared to the first, indicating precipitation and thus river discharge was higher in the latter half of HS1.

In South America, an antiphased relationship is observed between sites north and south of the Inter-Tropical Convergence Zone (ITCZ) during Heinrich stadials. The ITCZ, the ascending branch of Hadley cell circulation, is characterized by intense convective activity and high rainfall. In the modern day, the location of the ITCZ varies seasonally as a function of insolation maxima. The ITCZ reaches its northernmost position in June and its southernmost position in January. Areas currently in the

northern branch of the ITCZ have been shown to become drier during Heinrich stadials like HS1. The most notable example of this is the Cariaco Basin off the coast of Venezuela, which records changes in sediment color and in the amount of Ti and Fe deposition (Peterson et al., 2000; Deplazes et al., 2013). Sediment color analysis using sediment total reflectance (L*) of the basin reveals periodic shifts between terrigenous organic carbon and biogenic carbonate as the dominant component of sediment input (figure 6, Deplazes et al., 2013). When the region receives more rainfall, there is an increase in the input of terrigenous organic carbon, which is dark in color. When the region receives less rainfall, there is an increase in the percent composition of biogenic carbonate that is lighter in color. These shifts are further observed in Fe/Ca and Ti/Ca ratios. Ti and Fe are indicative of terrestrial sediment whereas Ca is derived from biogenic carbonate. When the region receives more rainfall, there are higher ratios of Ti/Ca and Fe/Ca than when the region is drier. During Heinrich stadials, particularly HS1, L* is high while Fe/Ca and Ti/Ca is low, indicating higher concentrations of biogenic carbonate and drier conditions in Venezuela.

Geochemical analysis of GeoB16224-1, a sediment core influenced by the Amazon River, further displays the trend of northern South America becoming drier while south of the ITCZ becomes wetter. The GeoB16224-1 record displays a two-phase decrease in sea surface salinity and sediment load coupled with increases in organic matter reflective of shifts in the spatial location of precipitation towards the central Amazon and away from the northern Amazon and tropical Andes (Crivellari et al., 2018). Increases in goethite relative to iron oxides in marine records further indicate

a spatial shift in the main precipitation locus to the Amazon lowlands and away from the Andes (Harris & Mix, 1999).

To the south of the ITCZ, an opposite trend in precipitation is seen compared to the north. In Northeast Brazil, a location currently outside of the ITCZ and with a semiarid climate, the region experiences a wetter climate during HS1 showcased through speleothem growth in caves, travertines, fossils, and vegetation shifts (Auler et al., 2004). Wang et al. (2004) dated speleothems and travertines, secondary cave features that form through calcite precipitation from water, in Northeast Brazil. Travertines, a feature that forms from holding water, are evidence for a wetter Northeast Brazil, as these features only form when there is an excess of water present in these caves. Dating of speleothems and travertines in the region from Toca da Boa Vista (TBV) and Toca da Barriguda (TBR) caves reveal precipitation is strongly tied to Heinrich stadials as the region is too dry for speleothem growth outside of these periods (Wang et al., 2004). A palynological and sedimentological record off the coast of NE Brazil, GeoB3912, provides further evidence of a wet period in the region during HS1 (Dupont et al., 2010). Pollen and spores change from being dominantly caatinga, a dry scrub brush-like vegetation, to a more diverse array of vegetation characteristic of denser wooded environments that require more rainfall. Ti/Ca and Fe/Ca ratios, proxies for terrestrial run-off, rise in the first phase of HS1 and decrease in the second phase of HS1 (Jennerjahn et al., 2004; Jaeschke et al., 2007). Terrestrial run-off is controlled by erosion rates modulated by precipitation and vegetation. The initially high run-off in HS1 is most likely a function of increased precipitation, whereas the decrease in the second

phase of HS1 when considered alongside the pollen record, is modulated by an increase in vegetation cover. Environmental change is shown in two steps, with the first being a shift to more wooded environments in the form of gallery forests, with undeveloped soils resulting in high erosion rates, and the second being where erosion is reduced from the development of soils and the expansion of wooded areas. Vegetational biome shifts during HSs in NE Brazil may have served as an essential ecological bridge for species exchange between the eastern Amazonian and the Atlantic forests (Costa et al., 2003).

ITCZ During Heinrich Stadials:

A mechanism for explaining the observed anti-phased relationship of precipitation records in South America during HS1 would be through a shift in the trajectory of the ITCZ. A displacement of the ITCZ towards the south would result in the Cariaco Basin and Tropical Andes becoming drier while NE Brazil and the Southern Amazon would become wetter. Peterson et al. (2000) proposed this mechanism as a potential way to explain the drying of the Cariaco Basin. Wang et al. (2004) evoked this mechanism to explain why dry periods in the Cariaco Basin coincided with wet periods in NE Brazil. This mechanism may also explain the precipitation changes seen in the Indo-Pacific which saw similar variations in climate between locations north and south of the equator (Muller et al, 2012; Huang et al., 2019).

Climate modeling furthered support for the ITCZ displacement mechanism shown in the climate records. Using a general atmospheric circulation model that resembles climate conditions during Heinrich stadials, Chiang et al. (2003) discovered that when increased ice cover is added to a hemisphere, there was a direct displacement of the ITCZ systematically away from that hemisphere by impacting Hadley circulation and increasing the north-south interhemispheric temperature gradient. When the northern hemisphere had higher ice cover, there was stronger tropical subsidence in the northern Hemisphere coupled with higher uplift in the southern hemisphere. Further investigation of this phenomenon using the CCM3-slab ocean model found the polar-equator teleconnection to be governed by a coupled wind, evaporation, and SST feedback (WES) (Chiang & Bitz, 2005). After an AMOC slowdown, colder North Atlantic sea surface temperatures and increased sea ice in the northern hemisphere caused lower sensible and latent heat fluxes to the air cooling the atmosphere. The colder air spreads across the high and mid-latitudes creating colder ocean surface temperatures in those regions. A strong pressure gradient develops, which increases the strength of the Northeasterly trade winds. Higher wind speeds of cool air cause evaporative cooling of surface oceans and propagate colder temperatures toward the tropics. As sea surface temperatures of the northern tropics cool, the inter-hemispheric pressure gradient increases, and high-pressure anomalies develop, the ITCZ shifts to the south, where higher SST and uplift persist. This process may also explain the fast-paced transition from HS1a to HS1b implied in paleoclimate records since modeling shows that significant displacement of the ITCZ can occur within a decade of perturbation (Chiang et al., 2008).

δ18O:

Oxygen has several stable isotopes, the most abundant being ^{16}O, and ^{18}O as the second most common. ^{16}O comprises 99.7% of oxygen atoms, while ^{18}O comprises ~0.18%. Stable isotopes are nuclides with the same number of protons but a different number of neutrons. They are stable in that they do not decay through time, so the abundance ratio between two isotopes is constant on Earth as a whole. The abundance ratio can change in an individual reservoir as a result of fractionation, a process that discriminates against one nuclide in favor of another. Generally, this is due to the difference in mass between the nuclides. To quantify fractionation, delta notation is used (Equation 1), where the isotopic composition of the sample is compared to the isotopic composition of a defined standard. Variations in $\delta^{18}O$ through time have been recorded in several paleoclimate records such as ice cores, foraminifera, and speleothems (Lisiecki & Raymo, 2005; Masson-Delmotte et al., 2005; Li et al., 1989). These $\delta^{18}O$ records have been used to understand how temperature, ice volume, ocean circulation, precipitation, and many other Earth dynamics have changed through time.

$$\delta\, 18O = \left(\frac{\left(\frac{18O}{16O}\right)_{reference}}{\left(\frac{18O}{16O}\right)_{standard}} - 1 \right) * 1000$$

Equation 1:Definition of $\delta^{18}O$

Oxygen isotopes fractionate due to kinetic and equilibrium fractionation. Equilibrium fractionation is slow and bidirectional, where each end member can become enriched or depleted in an isotope. The amount of fractionation is dependent on bond

strength, which is determined by temperature and mass (Kendall & McDonnell, 1998). Kinetic fractionation is unidirectional and based on reaction rate differences caused by mass and velocity, which is modulated by temperature. At colder temperatures, there is more fractionation compared to warmer temperatures.

$\delta^{18}O$ values in precipitation vary due to several factors, including latitude, elevation, continentality, evaporation, and generally are strongly modulated by temperature (Dansgaard, 1964). In a simplified system, oxygen isotopes fractionate throughout the water cycle during evaporation and condensation. Evaporation tends to be a kinetic fractionation process, while condensation is an equilibrium process. During the initial evaporation of seawater, heavy oxygen is discriminated against, and seawater becomes enriched in ^{18}O while the water vapor becomes depleted in ^{18}O. Further fractionation occurs as the air mass moves poleward through Rayleigh distillation (Dansgaard, 1964). In cloud processes, ^{18}O prefers the condensate phase, while ^{16}O is preferentially partitioned into air vapor. With each condensation event, the air mass becomes progressively more depleted in ^{18}O.

Around the ITCZ, temperature plays a minimal role in determining $\delta^{18}O$ values. Fractionation occurs due to deep vertical convection that characterizes atmospheric activity in the region. Here, the amount effect can be observed in $\delta^{18}O$ values, where rainfall amount is anticorrelated to $\delta^{18}O$ (Dansgaard, 1964). This is reflected annually in oxygen isotopes, with the rainiest months having the lowest $\delta^{18}O$ values. Dansgaard (1964) explained the amount effect as a function of progressive condensation within a storm, smaller isotopic exchange of water droplets during heavy rainfall, and the

reduced influence of evaporation on $\delta^{18}O$ in a high-humidity environment. Modeling of cloud dynamics suggests the amount effect is caused by the evaporation of rainfall in combination with the recycling of water vapor in the cloud system (Risi et al., 2008). Regardless of the cause, $\delta^{18}O$ precipitation values can be used to define the centrality of the ITCZ for a site.

The geographic distribution of $\delta^{18}O$ precipitation values in South America displays a clear pattern where monitoring stations inside the trajectory of the ITCZ have more negative values (~-5‰) compared to values outside the ITCZ (-2‰) (Wendt et al., 2019) (figure 7). As the ITCZ is characterized by high rainfall, lower $\delta^{18}O$ values can be used to infer that a site has a wet climate. Oxygen isotope paleoclimate records south of the modern-day ITCZ have interpreted a reduction in $\delta^{18}O$ as evidence of southwards displacement of the system (Wendt et al., 2019; Wang et al., 2004; Strikis et al., 2015). However, caution should be used in this interpretation as the amount effect is not the sole cause of $\delta^{18}O$ variation (Cruz et al., 2007).

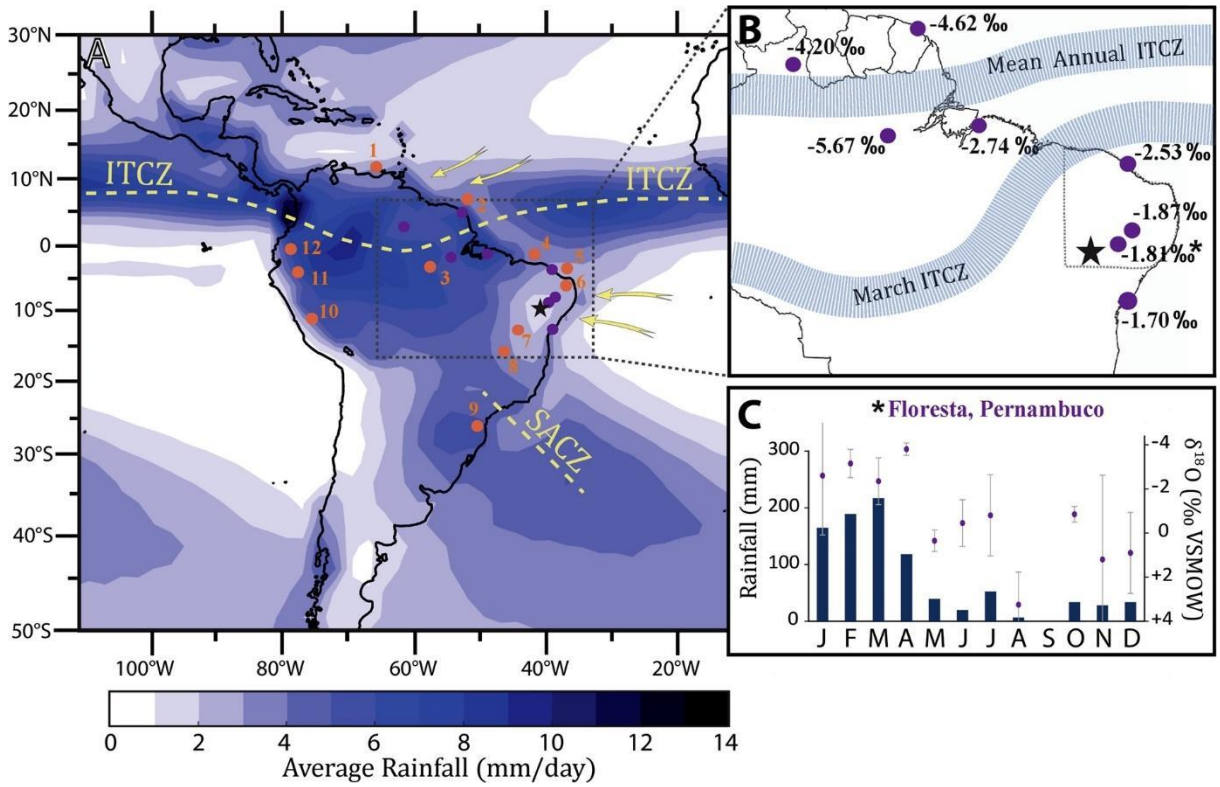

Figure 7: A) Average daily rainfall in modern South America. TBR is marked as a star. B) $\delta^{18}O$ as a function of proximity to the ITCZ. C) Monthly rainfall and $\delta^{18}O$ in Floresta, a town North of TBR. Figure taken from Wendt et al. (2019)

Trace Elements:

Trace metals refer to elements that are incorporated into speleothems in minor but detectable amounts. In the 1980s and 1990s, the trace element research in speleothems focused on Mg, partly, as it occurs at higher concentrations, but now includes a wide array of elements such as other alkaline earth metals (e.g., Ba and Sr), alkali metals (e.g., Li, Na, K), transition metals (e.g., Ti, Fe, Cu, Zn, Sr), metals (e.g., Al and Pb), semimetals (e.g., B and Si), nonmetals (e.g., P and S), and actinides (e.g., U). As the field now includes multiple elements that are not metals, the term trace elements is more accurate. Trace element to Ca ratios (TM/Ca) can vary through time as a

function of the strength of different processes such as aridity, rainfall, seasonality, fires, water residence time, growth rate, hiatuses, and more (Fairchild & Treble, 2009; Campbell et al., 2023). As each element can be affected by non-climatic processes such as water mixing, multiple elemental reservoirs, and co-occurring processes that have contradictory impacts on an element, it is crucial to understand how elemental ratios are altered to be able to discern climatically relevant ratio variability. When understood and carefully analyzed, changes in the concentrations and correlations of each element can help provide insight into various climatic parameters as a powerful proxy tool.

Initially, it was thought that the distribution of Mg/Ca in speleothems was temperature dependent and could be used as a paleothermometer of seasonal or long-term temperature change (Gascoyne, 1982). However, the variability of Mg/Ca ratios in speleothems is significantly larger than what could be expected if temperature was the governing factor (Roberts et al., 1998). Roberts (1998) instead postulated that variation of water residence time in the host rock above a cave was the cause of different Mg/Ca ratios.

Mg concentrations in drip waters are primarily impacted by water-rock interaction (WRI), water mixing, and carbonate precipitation along the flow path; the extent of these impacts is strongly dictated by aridity through changes in water residence time and Prior Calcite Precipitation (PCP) (Fairchild et al., 2000). Water mixing can result in higher Mg/Ca ratios if the introduced water source has higher concentrations of Mg than the typical source. Longer water residence time leads to an increased contribution of

incongruent dolomite dissolution compared to calcite dissolution, as the former process is slower. The incongruent dissolution of magnesium results in higher Mg/Ca ratios as residence time increases. PCP occurs when supersaturated water encounters a void space with lower pCO_2 (figure 8). In this scenario, CO_2 will degas from the drip water and calcite will precipitate out of solution. As Ca preferentially precipitates over Mg, Mg/Ca becomes enriched in the drip water. Thus, Mg/Ca ratios can be used as a proxy for aridity since cave ventilation (PCP) and mean water residence times increase during these times (Fairchild & Treble, 2009).

The usefulness of Mg/Ca as a proxy for aridity is increased when the Mg/Ca ratio corresponds to similar TM/Ca ratio variability of Sr and Ba. PCP impacts alkaline earth metals. When increases in all three ratios are simultaneous, the likelihood of aridity impacting the ratios is improved. Non-covariation can occur under various scenarios, including if Ba and Sr are derived from non-host rock sources or if the host rock has a high Mg concentration. Ba and Sr can originate from suspended detrital material in water, and Sr can be wind deposited as well (Orland et al., 2014). When the three elements do not covary, it does not mean that PCP is not occurring, but rather that other factors exhibit greater influence on the signals.

Soil above the cave represents the other major reservoir of trace elements incorporated into speleothems. For the scope of this project, Phosphorous (P) is the only primarily soil-derived trace element investigated. P can be a difficult proxy to interpret as it occurs in multiple forms and its concentration depends on reservoir size and transport efficiency. P in speleothems can be sourced from free phosphate ions

from soil minerals, attached to organic matter colloids sourced from plant decay, or through in-situ microbial activity on the speleothem (Frisia et al., 2012; Huang et al., 2001; Treble et al., 2003).

Inorganic P and organic P are the dominant forms of P in speleothems. Using total organic carbon (TOC) analysis on a speleothem in Grotta di Ernesto, Huang et al. (2001) found that most P is inorganic and incorporated through phosphate ions. P cannot solely be sourced from inorganic ions, as P colloids are the main contributor of the humic and fulvic acids that characterize fluorescent organic matter (FOM) (Orland et al., 2014). In the same 2001 study, Huang found that during infiltration events, P concentrations increase and coincide with higher fluorescent organic material, indicating that organic phosphorus influences P concentrations (Huang et al., 2001). The two forms can also be separated since organic P has a specific response to seasonal forcing.

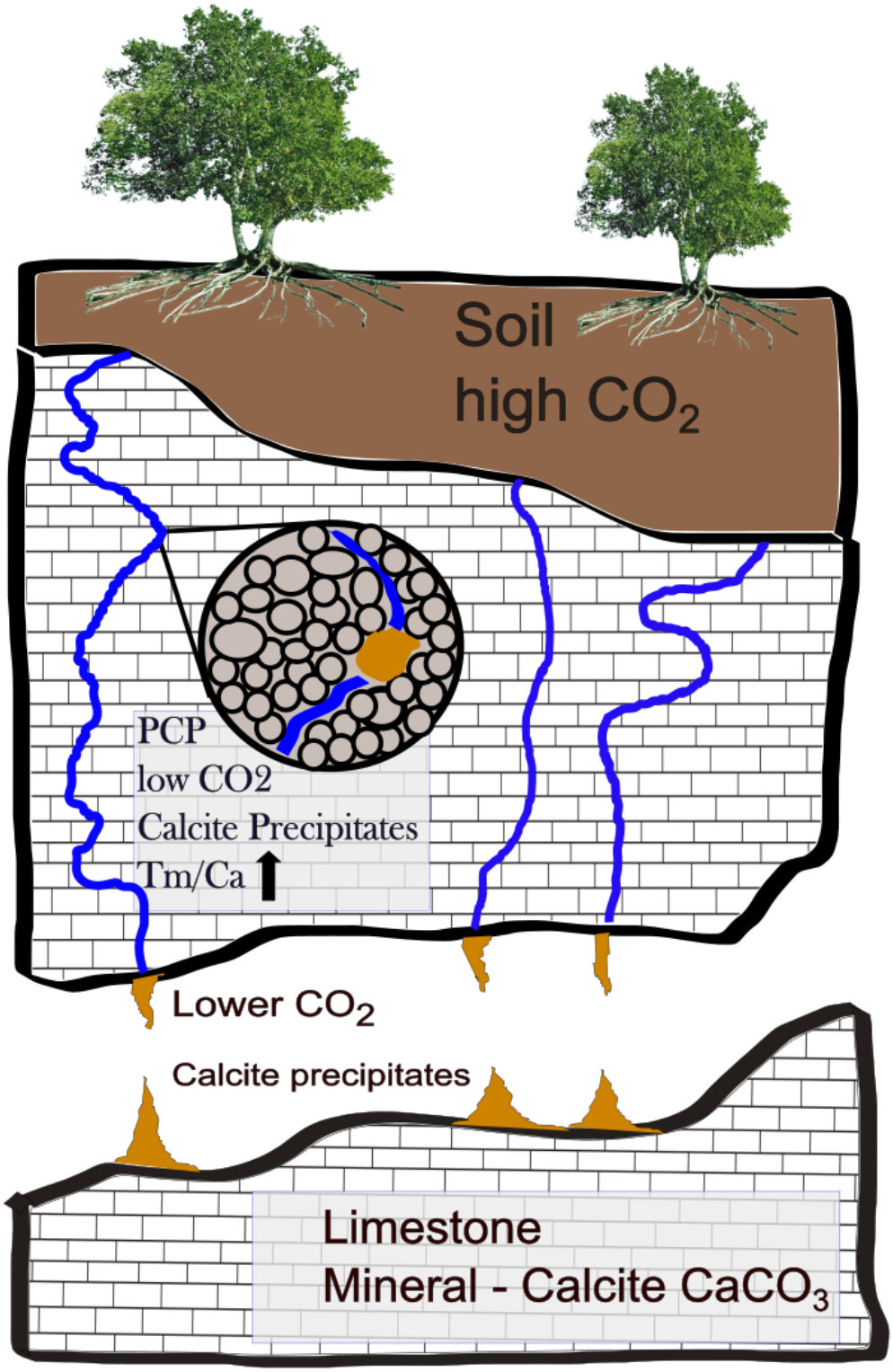

Figure 8: Conceptual diagram of how Tm/Ca varies as a function of PCP.

Inorganic P is incorporated throughout the year, while organic P has short-lived periods of significantly higher concentrations due to the flushing of organic matter after plant decay accumulates during a prolonged dry season (Borsato et al., 2007). This temporal distribution pattern of organic P can make it an excellent proxy for understanding past pluvial periods. The potential of this proxy was originally shown through P accurately mimicking rainfall distribution in a monitoring study of Moondyne cave in SW Australia (Treble et al., 2003).

Interpretations of P are commonly interpreted as changes in rainfall and seasonality. Climatic interpretation of P can be difficult as it is site specific. A cave site with seasonally segregated rainfall, like Moondyne Cave, will have a different climatic signal than a tropical environment with rainfall equally distributed throughout the year (Frisia et al., 2012). P can change due to several factors because reservoir size and transport efficiency of P can vary based on soil, soil minerals, vegetation, rainfall distribution, and rainfall amount. Commonly, P concentration will be lower during periods of reduced rainfall and higher during infiltration events (Treble et al., 2003; Orland et al., 2014). However, shortened dry periods can result in a reduced colloidal pool and a weaker P signal by decreasing the overall reservoir size and expanding the temporal distribution of P throughout the year (Hartland et al., 2012). Vegetation changes are also known to affect the P signal in speleothems. Modern analysis of speleothems found that deforestation resulted in an increased concentration of P in speleothems (Borsato et al., 2007). This is due to enhanced transport efficiency of infiltration events and possibly due to elevated microbial activity increasing degradation

of organic material. Transient peaks in the P signal can also indicate growth hiatuses in the speleothem.

Confocal Banding:

Confocal Laser Fluorescent microscopy (CLFM) has been utilized in a number of speleothem paleoclimatic studies for understanding climate change and lending support to U-Th derived chronologies. CLFM reveals the fluorescent banded structure apparent within some speleothems when exposed to a blue light laser under a confocal microscope. A band consists of a light and dark couplet. The light (bright) section appears brighter under a confocal microscope as it contains a higher amount of fluorescent organic matter (FOM) in comparison to the dark couplet. Calcite precipitated during a bright band segment is interpreted as precipitating during a wetter interval, when the input of FOM through fulvic or humic acids is the highest. In contrast, calcite precipitated during periods of reduced surface influence will have reduced concentrations of FOM. In many cases, the periodic change between light and dark banding is seasonal and can reflect annual changes in rainfall (Baker et al., 1999).

Partial annual confocal banding has been found at many cave sites. Annual banding allows for precise measurement of growth rate, high resolution analysis of climate change, and can bolster U-Th chronologies. For example, Domínguez-Villar et al. (2012) utilized a 1:1 ratio between annual confocal banding and U-Th-based ages to infer where hiatuses in the speleothem chronology occurred. However, annual banding should not be assumed in seemingly well-banded speleothems. Analysis of well-

constrained, modern speleothems show that banded records can under record time (Orland et al., 2014). In many cases, annual banding is present but not throughout the entire record. Supra-annual banding can be present in samples from the influence of quasi-periodic climate cycles such as El Nino Southern Oscillation (ENSO), and sub-annual banding can form from groundwater mixing (Martin-Chivelet et al., 2017). Annual banding can be verified by comparing the number of bands to U-Th dates in a well-constrained age layer, verifying stark seasonal changes in the amount and composition of drip water, and monitoring studies of modern growth layers (Tan et al., 2006).

Caves in climates with distinct dry and wet seasons tend to exhibit confocal banding most strongly (Baker et al., 2021). As fluorescent intensity is inversely connected to depth, shallow caves will also have stronger fluorescent banding (Cruz et al., 2005). Speleothems that are more susceptible to strong banding are especially well-suited for analysis as they are more sensitive to climate change. Variations in confocal banding width, brightness, and structure can indicate significant changes in climate. Proctor et al. (2000) connected changes in laminae width to the strength of the North Atlantic Oscillation (NAO). In a study of NE Brazil during HS4, Wendt et al. (2019) found a transition between distinct seasonal banding couplets to double bright couplets where instead of a light band followed by a dark band, the banding was characterized as a bright band to another bright band (figure 9). In this case, the banding served as foundational evidence for the region having two rainy seasons in a year, which could have been possible with a far enough displaced ITCZ. Orland et al. (2014) found that changes in the clarity of confocal banding coincided with a regime shift in the climate

where a transition to an arid climate was met with muted fluorescence. Climatic interpretation of fluorescence is strengthened by the proxy's connection with other records. High-resolution ion probe measurements of $\delta^{18}O$ reveal that annual banding closely correlates with seasonal changes recorded in oxygen isotope measurements (Orland et al., 2009). Comparison of banding with trace elements shows that the annual fluorescence profile coincides with peaks in phosphorous and troughs in host rock derived elements, supporting the argument that the proxy is tied to rainfall (Sliwinski & Stoll, 2021). The close correspondence of phosphorous and copper to FOM shown in Principal component analysis (PCA), led to the elements being determined as the dominant components of FOM (Orland et al., 2014). Therefore, understanding the processes behind P and Cu concentrations can expand interpretations of fluorescent banding.

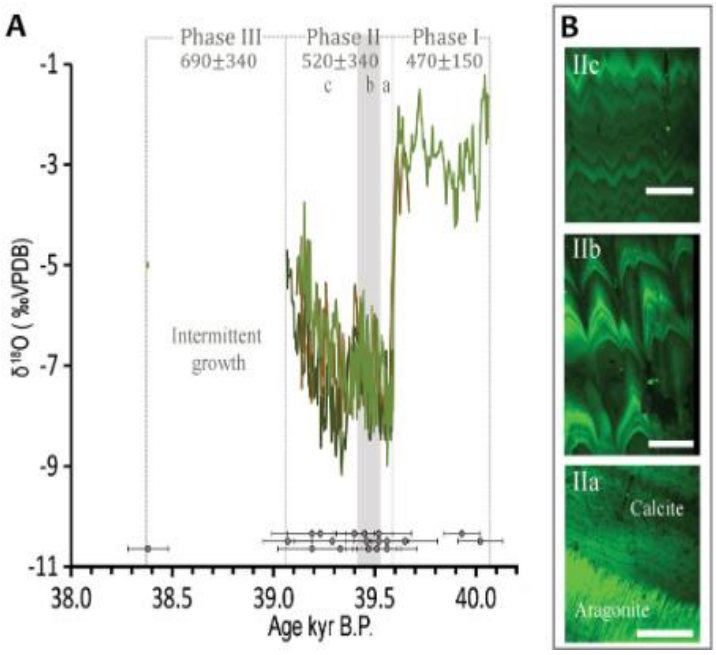

Figure 9: H4 had 3 distinct phases. During phase 2, the fluorescent banding changed in response to higher precipitation and shorter dry seasons Wendt et al. (2019).

Uranium – Thorium Dating:

Uranium-thorium dating (U-Th dating) is a radiometric dating technique that is widely used in paleoclimatology to construct precise, high-resolution chronologies of speleothem and coral growth layers. The temporal resolution of U-Th dated speleothems is unparalleled in paleoclimatology, allowing for a detailed reconstruction of rapid climate change that is not possible in other paleoclimate records. Currently, U-Th dates can be obtained from any sample with U concentrations of ppb or greater that formed between a few years – 650,000 years ago (Wendt et al., 2021). Uncertainty can be higher in samples with lower concentrations of U and Th.

$$relative\ error = \frac{2}{\sqrt{number\ of\ counts}}$$

Equation 2:Counting statistics error equation.

Historically, U-Th dating has been limited by analytical capabilities and counting statistics. Counting statistics characterizes the relative error of measurement and is shown in equation (2), where precision is related to the number of counts. Counts are determined by the number of atoms of a sample, the ionization efficiency of the instrument, and how many ionized particles are counted on the instrument. Originally, U and Th were measured using alpha counting, which measures the number of alpha particles emitted over time from alpha decay to calculate the concentrations of each nuclide. Alpha counting requires large sample sizes, 10s of grams, and is time-consuming. Temporal resolution is inherently low in alpha counting due to the method

requiring a large sample size, resulting in multiple growth layers being analyzed together. Analytical capabilities of U-Th measurements improved significantly using Thermal Ionization Mass Spectrometry (TIMS). The more precise measurements provided through TIMS allowed for sample sizes over an order of magnitude smaller while reducing age uncertainty and temporal resolution. Mass spectrometry measurements of ^{234}U and ^{230}Th are only possible due to the work of Chen et al. (1986) and Edwards et al. (1987). Li et al. (1989) were the first to collect U-Th measurements on speleothems using a mass spectrometer. Analytical capabilities were improved further through multi-collector inductively coupled plasma mass spectrometry (MC-ICP-MS). Advancements in analytical techniques are still possible since measurement capabilities are still limited by low ionization efficiency (~1.3%) (Wendt et al., 2021).

The dating system is based on the ^{238}U decay chain and three radionuclides: ^{238}U, ^{234}U, and ^{230}Th. Each nuclide is radioactive, while ^{234}U and ^{230}U are radiogenic. U-Th dating is a disequilibrium dating system where the age of a sample is determined by the amount of time that has passed since a fractionation event. Disequilibrium dating requires the daughter nuclides to be able to fractionate from each other and for their half-lives to be small in comparison to the original parent. In U-Th dating, ^{238}U has a significantly longer half-life than its intermediate daughters. The half-lives of ^{238}U, ^{234}U, and ^{230}Th are $4.4683 \pm 0.0048 \times 10^9$ years (Jaffery et al., 1971), 245,620 ± 290 years, and 75,590 ± 110, respectively (Cheng et al., 2013). When applied to the Quaternary period, ^{238}U can be treated as a stable isotope. Fractionation can occur due to the intrinsic differences in chemical properties between uranium (U^{6+}) in uranyl (UO_2^{2+}) and

thorium (Th^{4+}) ions at the surface. When interacting with water, the ions separate since uranium is soluble while thorium is insoluble as a result of differences in their valence states. Before a fractionation event, a system is at secular equilibrium where the activity ratios, the product of the decay constant, and the number of atoms of a nuclide of the component are equal. During a fractionation event, unity is disrupted as the activity ratios of the three radionuclides become unequal. In a closed system where the initial parent/daughter ratio is known, the time since the fractionation event occurred can be calculated until the system has reached secular equilibrium (figure 10).

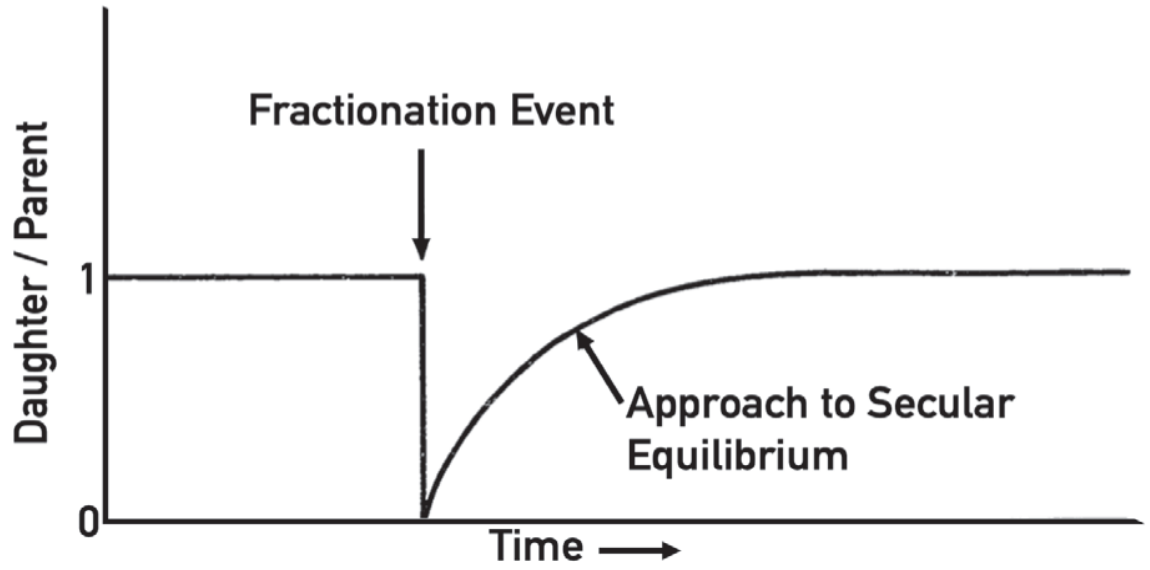

Figure 10: Conceptual graph of disequilibrium dating detailing the parent/daughter activity ratios through time before, during, and after a fractionation event (Wendt et al., 2021).

In the context of speleothems, the fractionation event occurs in the soil or bedrock where rainwater acquires uranium but not thorium due to the intrinsic solubility differences between the two elements. The water travels through the epikarst before

reaching the cave and precipitating on a speleothem. Precipitate formed during the same time will create a growth layer. As precipitation continues, the layer becomes isolated from drip water and becomes a closed system. At this time, (t=0), it is assumed that no ^{230}Th is present. With the initial ratio between Th and U known and the closed nature of the system, the conditions for U-Th disequilibrium dating are met. Under these conditions, ^{230}Th forms radiogenically through ^{234}U and the activity ratio of the three radionuclides can be used to find the age of the growth layer. The age calculation can be done using Equation (3) where A is the activity ratio, lambda is the decay constant, and δ^{234}U represents the fractionation ratio between ^{234}U and ^{238}U.

$$\left[\frac{230Th}{238U}\right]_A = 1 - e^{\lambda_{230}t} + \frac{\delta^{234}U}{1000}\left(\frac{\lambda_{230}}{\lambda_{230} - \lambda_{234}}\right)\left(1 - e^{-(\lambda_{234} - \lambda_{230})t}\right)$$

Equation 3: U/Th Age calculation equation

Methods:

U-Th Dating:

Preliminary U-Th measurements of TBR-14 by Wang et al., (2004) and Wendt et al., (2019) provided eight U-Th dates. These dates served as a framework for determining where additional dates were needed to improve the age – depth model and provided activity ratios necessary for estimating sample size. Nine additional samples and three replicate samples were drilled for U-Th dating measurements. Samples were hand drilled along calcite growth laminae. Sample weight should have been determined using Eq (4) and the U^{238} concentrations and 230/238 activity ratios calculated within the original U-Th measurements. I used an outdated sample size calculation sheet that did not correctly use this equation, which resulted in too small of a sample size and

higher age uncertainty. Desired counts refer to the number of counts required to achieve counting statistics of 1‰ (4 million ions), ionization efficiency (ion efficiency) is set at 1.3, lambda refers to the decay constants, and the activity ratios and ^{238}U concentrations were taken from the work done by Wendt (2015) and Wang (2004).

Equation 4: Sample size equation for U-Th dating

$$Sample\ size(g) = \left(\frac{desired\ counts}{Ion\ effeciency} * \frac{1}{6.022 * 10^{23}}\right) * \left(\frac{\lambda_{230}}{\lambda_{238}} * \frac{1}{\left(\frac{230}{238}\right) Act}\right) * \left(\frac{238_{g/mol}}{238_{U\ conc}}\right)$$

U-Th data acquisition follows the procedure described in Edwards (1987) and Wendt (2021). After samples are weighed and dissolved in 14 N HNO_3, a diluted isotopic spike containing ^{236}Th, ^{233}U, and ^{238}U is added to the sample so chemistry yield can be found. The spike weight was determined using the preliminary U-Th measurements and the spike calculation spreadsheet that calculates the amount of spike required to establish the ratio of $^{235}U/^{233}U$ to ~13.

Chemistry yield is a measurement that expresses how much sample was lost during the U-Th dating procedure. By comparing the concentrations of these isotopes after the procedure to their known initial concentration, it is possible to determine yield. This measurement is made easier in that these isotopes of uranium and thorium are not natural in the sample, so changes in their concentrations are solely interpreted as sample loss during the chemistry procedure. A chemistry blank is processed alongside samples to check for contamination during the chemistry procedure.

After the spike was added, samples were dried down. There are three dry-down cycles in the chemistry procedure. The first cycle occurs after spiking, the second at the

end of the iron coprecipitation process, and the third after column chemistry. Each cycle consists of five steps with the fifth step changing every cycle. The fifth step involves dissolving the sample in 2 N HCl, 7 N HNO_3, and ICP solution respectively. Each step other than the fifth is followed by drying down the sample on a hotplate. The first four steps consist of drying the sample down, then redissolving it in two drops of $HClO_4$, and afterward dissolving the sample in 14 N HNO_3 twice.

The iron coprecipitation step binds uranium and thorium cations to iron flakes while removing anions. $FeCl_2$ and NH_4OH are added to the dissolved solution. $FeCl_2$ precipitates iron flakes. NH_4OH is added to the solution to raise the PH so that iron precipitation is possible. Once iron flakes have precipitated, the solution is centrifuged for seven minutes at 2500 rpm. Centrifuging compacts the iron flakes and allows the anions in the supernatant to be removed. This process is performed three times before the second dry down cycle begins.

During the second dry down, columns are prepared. The solution is poured into the columns containing a cation exchange resin and flushed with 7 N HNO_3 to remove iron from solution. Thorium is separated from uranium with 6 N HCl. Finally, uranium is removed from the columns with super clean H_2O. The thorium and uranium solutions undergo a final dry down and are dissolved in ICP solution containing super clean water, 1% nitric acid, and hydrofluoric acid.

Each sample's uranium and thorium fractions are measured on a Thermo-Finnigan Neptune inductively coupled plasma mass spectrometer (ICP-MS). ^{229}Th, ^{230}th, ^{232}Th, ^{233}U, ^{234}U, and ^{235}U are measured. ^{238}U is not measured as it is too abundant to

measure on the ICP-MS, but it can be calculated with the constant $^{235}U/^{238}U$ ratio. Machine blanks are run between sample measurements to account for instrumental noise. To reduce measurement uncertainty in uranium, samples are run until 4 million counts have been recorded to overcome counting statistics and achieve 2‰ error. Due to the sample being relatively young and initial uranium concentrations being low, thorium was very limited in the sample so counting statistics usually could not be achieved in thorium measurements resulting in greater age uncertainty. The age of each sample was then calculated.

Age Depth Model:

The age-depth model for TBR-14 was created using OxCal software and 17 out of the total 22 U-Th dated ages. Due to the relatively short temporal duration of growth and the fast growth rate of the stalagmite, the influence of small uncertainty in the U-Th dates was larger than a typical sample. A curated list of U-Th dates was used instead of all U-Th data to reduce the impact of the age uncertainty on the age depth model. A threshold of 40 percent was used to eliminate four dates, and a single date was discarded on the basis that it had no yield information and was 500 years out of stratigraphic order.

Oxygen and Carbon Isotopes:

Calcite was micro-drilled at 0.5 mm resolution (~5 years) for the whole record and a high-resolution trench was milled between (49 – 42 mm) (~16.21 – 16.15 ka B.P) at 0.1 mm resolution (~1 year) by Katee Wendt. In total, 276 samples were analyzed for their oxygen and carbon stable isotopic composition using a Finnigan Delta V Advantage mass spectrometer equipped with an automated carbonate preparation

system (Gas Bench II). Measurements were performed by Anamaria Häuselmann at the Institute of Geological Sciences, University of Bern, Switzerland. Results are reported relative to the Vienna Peedee Belemnite (VPDB) standard. To check for isotopic equilibrium, a Hendy test was performed where five subsamples along a single growth layer were drilled and analyzed (Hendy, 1971).

Confocal Image Acquisition:

Confocal laser fluorescent microscopy (CLFM) imagery was created to document the entirety of H1 confocal banding present within the 110 mm growth event. The imaging was used to create a full-tilled image of the banding, measure 958 individual growth bands, create a confocal band brightness profile, and determine an estimate and absolute minimum growth period duration in years.

Images were produced using the Nikon A1R-MP microscope at the University of Minnesota Imaging Center with a Plan Apo lambda 20x objective. The laser operated using a 488-excitation nm wavelength line and captured fluorescent emissions at 525 nm wavelengths. The A1R-MP is equipped with a moving sample stage that is capable of 70 mm of x direction movement which allows for large samples to be scanned. Since the H1 growth of the sample is 110 mm long, image acquisition was done in two separate intervals, and two finalized composite images were the maximum that could be achieved. The first 60 mms of the sample was scanned for two consecutive days with the instrument staying powered on to ensure the sample would not be displaced on the moving stage and that each ~ 10 mm composite section would share an absolute orientation. The last 50 mm of growth was scanned in a single continuous session.

Before imaging the sample, the sample was aligned to the x and y coordinate of the stage so that x-axis movement did not result in y-axis drift of the sample. Each image is a composite of hundreds of separate captures produced using the “scan large image” function on the Nikon software. When using the “scan large image” function, the user defines the x-y bounds they desire for the top, bottom, left, and right of the large composite image. At each bound, a z point is given where the features of interest are most visible; for speleothems, this is the fluorescent banding. If the z depth of the selected area changes non uniformly, additional z calibrations within the selected area are required. Z depth calibration was completed using the resonant scanner at a lower resolution for time efficiency. The final acquisition of each image was performed using the galvonomic scanner with a 2.4 second dwell time and an averaging selection of 2.

The stage bounds for each initial composite image were 10,250 microns long and 3,000 microns wide, not including the reference ruler. ~10 mm is the optimal length for each initial composite to maximize the amount of sample that is scanned at once without sacrificing confocal band clarity or wasting machine time due to a complicated surface focusing process. 10,250 microns allows for a 125-micron overlap with the composite sections before and after each composite. The 125-micron overlap is used in the final tiling procedure to create the finished composite images of the sample.

The 11 (~10 mm) initial composite images produced on the A1R-MP were combined to create a final composite image from 0-60 mm and another from 60-110 mm using the Nikon NIS Elements Viewer software. Each image was cropped to be of uniform dimensions (10.8 mm x 3.3 mm, 17256 x 5322 pixels) before the final tiling

procedure. The 125-micron stage coordinate overlap that was used to create each section resulted in each initial composite being 10,800 microns, as the coordinates determined where the laser was centered, resulting in areas outside the bounds being imaged. Each composite was then combined using an eight percent overlap to create the two continuous confocal images.

Pixel intensity was measured through a transect in both the 0-60 and 60-110 mm composite images. Transects were chosen based on the criteria that the transect had to be as close as possible to the ruler and had to minimize the amount of coverage of erroneously bright spots. Proximity to the ruler is ideal since it would increase the likelihood that the depth scale of the brightness was aligned with the oxygen isotopes or other proxies. Erroneously bright spots are characterized as areas that have a brightness value over 3,000, are globular in shape, and do not display the features associated with a confocal band. These spots are associated with blemishes on the surface of the stalagmite slab and are the result of poor polishing or scratching of the sample. The transect from 0-60 was distanced 2.68 mm away from the edge of the ruler to avoid the high-resolution stable isotope trench present at (42-49 mm) which appears as dark in confocal imagery and has an intensity value of 0. The transect from 60-110 mm was distanced 0.93 mm away from the ruler to avoid a large erroneously bright spot. To minimize the influence of erroneously bright spots on the intensity transects and obtain representative mean intensity values throughout the sample, the intensity values were calculated using a nearest neighbor function of 128 pixels and 512 pixels

(81.92 and 327.68 microns respectively). This function calculates the average intensity values of pixels along the y-axis at each x-axis' coordinate.

Growth rates were measured individually for each 10 mm section. The mean growth rate, the distance between two bands, the standard deviation of growth rate, minimum growth rate, maximum growth rate, and the total number of growth bands were collected for each section. The total number of growth bands per section was compared to the counted number of manual and WICOUNT bands for every 10 mm (WICOUNT discussed in the following section). The growth rate was measured by using a distance tool on the Elements Viewer Software that finds the horizontal x-axis distance between two points. The advantage of this tool compared to other distance tools on the software is that it allows the user to select two points at different y coordinates and find the x distance, which is very useful for growth bands where the visibility of each band is at a variable y coordinate. In cases with clear and distinct banding, bands were measured from the apex of one band to the apex of another (peak to peak). If a growth band was faint, the band would be measured from the most distinct portion of the band to the same portion of the next growth band. The data was then exported to Excel.

The measured bands had a total count difference of 2 percent compared to the manually counted bands and 5 percent compared to the WICOUNT number of bands. In most sections, there was less than a 10 percent disagreement between the counting methods except section 70-80 mm, where only 78 bands could be measured compared to 95 and 108 bands counted manually and with WICOUNT respectively.

Confocal Band Counting:

Confocal band counting was accomplished through two different methods: manual and automatic counting using WICOUNT. Both band counting methods were done in 10 mm sections starting from 10 mm, as the 0-10 mm scan did not have consistent and easily visible banding. Images were cropped to be exactly 10 mm so no band would be counted twice and so that the ruler would not be visible, since this would impact the automated software count. Annual banding was checked for by comparing the count of each 10 mm section against the total time passed implied by U-Th dates.

Manual band counting was performed three times for each section. Each bright band was counted as a single layer. If a band disappeared in the transect that was being counted, the mouse cursor would move along the growth layer until a clearer band was present. As an additional check, another person would periodically count a 10 mm section.

Automatic band counting was done through the software WICOUNT developed by Fabio Oriani from the University of Lausanne, Switzerland (2022). Traditional automated band counting involves using line transects through a record and using a peak counting technique to find the number of bands present. Transect based techniques introduce error into band counts as they are unable to accurately count peaks when the transect crosses erroneously bright areas or regions with faded banding. WICOUNT uses an entire image for band counting, reducing the influence of these situations on the total band count. An example of a 10 mm WICOUNT image is available in supplemental figure 2.

WICOUNT takes an image, filters small scale noise with a five pixel moving average, and then utilizes dynamic time warping (DTW) to align non-linear features of interest (Oriani et al., 2022). DTW compares two subsequential rows of pixels, identifies matching sequences of pixels, and combines them into an identical set. After each DTW pass, the number of rows is halved. This process continues until all features have been aligned and only a single row of pixels exists. Afterwards, a time series is constructed from the pixel values where each lamina is represented as a certain magnitude and length. Using a wavelet transform and manually selecting the wavelet corresponding to confocal bands, laminae detection occurs (Oriani et al., 2022).

Trace Metals:

The TBR-14 slab used for confocal imagery was too large to be used for laser ablation trace metal analysis. To prepare for trace metal analysis, the slab was cut into eight sections (figure 11) using a Las-Tec laser technology wire saw (model 2008 – 0 – 0) with a 0.25 mm saw kerf. Six cuts were made, resulting in two thick sections along the H1 growth axis that could be used for laser ablation. A diagonal cut was made along the growth axis to ensure that no growth layer was fully lost in the sawing process. Section 7 is the result of the sample breaking during shipping prior to the cutting process. Section 2 is 11 mm thick, 25 mm wide, and 48 to 55 mm long. Section 5 is 9 to 10 mm thick, 24 mm wide, and 71 to 79 mm long. Section 2 covers from the top to 52 mm at the growth axis and section 5 covers from 52 mm to 130 mm at the growth axis, meaning it covers past the H1 – H4 boundary.

Laser ablation work was performed at UC Davis using an Agilent 7700 ICP-MS coupled to a laser. The H1-H4 hiatus boundary, oxygen isotope transition at 37-49 mm depth, and a possible hiatus at 71 – 72 mm depth were selected regions for preliminary analysis as they were high priority regions of interest. These sections were ablated to get an estimate for the general trace element concentrations in the sample. Th and Y were excluded from further analysis as they had minimal differences between the signal and limit of detection (LOD). Al and Cl were eliminated from final analysis as the signal was indistinguishable from the instrumental baseline. S was taken out due to low confidence in its signal.

Li, B, Na, Mg, Si, P, K, Ca 42, Ca 44, Ti, Fe, Cu, Zn, Sr, Zr, Ba, ^{206}PB, and U were included for acquisition for the whole sample traverses and experiments. Three trenches were ablated to ensure reproducibility of data. The trenches were ablated using a 40-micron laser spot size and a 10 micron/second ablation rate. The data was then converted from time of laser acquisition session to depth by multiplying the time a measurement was taken to the ablation rate. The endpoints of the trenches were imaged using confocal reflectance spectroscopy on the A1R-MP confocal microscope to precisely align the trace element depth data to the depth scale. The aligned data was then input into the age depth Oxcal model where the data was converted to time series.

Data analysis consisted of outlier removal, elemental pairwise correlation analysis, and principal component analysis (PCA). Outliers were removed using a rolling mean with a window size of 100 data points (1mm). Elemental pairwise correlation and PCA was performed at 5 time segments; the whole record (17.03 –

15.45 ka B.P.), the main growth period (16.97 – 15.85 ka B.P.), before the oxygen isotope shift (16.97 – 16.27 ka B.P.), encompassing the oxygen isotope shift (16.27-16.16 ka B.P.), and after the oxygen isotope shift (16.16 - 15.86 Ka B.P) were analyzed. PCA and pairwise correlations were utilized given that they can illuminate how different trace elements are related. The main growth period was analyzed, as the beginning of the whole record contains a period of anomalously high concentrations of every element in the record and therefore skewed the pairwise correlations of every element to being significantly correlated, whereas in the record this is not the case. This period of data is most likely attributed to the cave system being inactive for ~22,000 years. The three segments corresponding to the different phases of the oxygen isotope record were selected to see how correlations between elements varied across the different pluvial regimes indicated by the oxygen isotope record.

Figure 11: TBR-14 sample divided into 8 sections. Sections 1,2,3,4,5,6, and 8 were made using the wire saw. Section 2 and 5 were analyzed for trace metals.

Analytical Scientist (initials)	Sample Depth (mm)	^{238}U (ppb)	^{232}Th (ppt)	$^{230}Th/^{232}Th$ (atomic x 10^{-6})	$d^{234}U^{*}$ (measured)	$^{230}Th/^{238}U$ (activity)	^{230}Th Age (yr) (uncorrected)	^{230}Th Age (yr) (corrected)	$d^{234}U_{initial}^{**}$ (corrected)	Age B.P.
XF	3	27 ±0	1 ±4	105683.3 ±274072.1	1568.9 ±11.4	0.3475 ±0.0054	15648 ±270	15648 ±270	1640 ±12	15579 ±270
XF	6	30 ±0	3 ±2	61810.6 ±55478.0	1554.5 ±5.9	0.3453 ±0.0035	15632 ±171	15632 ±171	1625 ±6	15563 ±171
WH	10	44.5 ±0.1	618 ±12	373 ±8	1238.9 ±3.6	0.3138 ±0.0012	16247 ±70	16070 ±143	1296 ±4	16001 ±143
WH	15	40.3 ±0.0	3 ±0	71830 ±7409	1427.9 ±2.4	0.3359 ±0.0008	16009 ±44	16008 ±44	1494 ±2	15939 ±44
WH	20	30.7 ±0.0	32 ±1	5375 ±150	1465.2 ±2.5	0.3434 ±0.0017	16126 ±87	16114 ±87	1533 ±3	16045 ±87
KW	41	57 ±0	1 ±1	2546310.8 ±1031700.6	1718.1 ±4.3	0.3798 ±0.0013	16164 ±64	16164 ±64	1798 ±4	16095 ±64
WH	45	34.3 ±0.0	29 ±1	7584 ±263	1770.0 ±2.8	0.3900 ±0.0017	16290 ±78	16282 ±79	1853 ±3	16213 ±79
WH	49	40.7 ±0.0	12 ±1	20962 ±1458	1691.0 ±2.2	0.3804 ±0.0017	16365 ±80	16362 ±80	1771 ±2	16293 ±80
KW	50	68 ±0	2 ±0	208751.7 ±45455.0	1780.6 ±2.6	0.3882 ±0.0010	16144 ±47	16144 ±47	1864 ±3	16075 ±47
WH	60	78.7 ±0.1	58 ±2	8610 ±369	1682.0 ±3.2	0.3844 ±0.0023	16608 ±107	16601 ±107	1763 ±3	16532 ±107
XF	67	108 ±0	2 ±3	342226.6 ±465436.2	1846.0 ±5.2	0.4062 ±0.0024	16547 ±111	16547 ±111	1934 ±5	16478 ±111
KW	81	82.5 ±0.1	3 ±1	235029 ±48847	2121.5 ±3.1	0.4499 ±0.0011	16684 ±45	16683 ±45	2224 ±3	16614 ±45
WH	90	95.1 ±0.1	57 ±15	12650 ±3238	2179.0 ±3.4	0.4623 ±0.0018	16842 ±71	16836 ±71	2285 ±4	16767 ±71
WH	90	96.1 ±0.1	58 ±2	12763 ±389	2182.3 ±3.2	0.4646 ±0.0016	16914 ±65	16909 ±65	2289 ±3	16840 ±65
WH	104	103.6 ±0.5	7 ±1	122630 ±11559	2277.7 ±6.1	0.4837 ±0.0080	17104 ±119	17103 ±119	2390 ±6	17034 ±119
KW	106	171.1 ±0.2	9 ±1	149725 ±12201	2175.8 ±3.0	0.4691 ±0.0011	17123 ±47	17123 ±47	2283 ±3	17054 ±47
XF	106	207 ±0	16 ±3	103450.9 ±18937.0	2201.2 ±5.4	0.4725 ±0.0021	17133 ±87	17133 ±87	2310 ±6	17064 ±87

Table 1: Uranium-Thorium dating results of TBR-14 from Toca Da Barriguda cave in NE Brazil.

Results:

U-Th Dating:

Seventeen U-Th dates were collected from TBR-14 and incorporated into the OXCAL age-depth model (figure 12). Four replicates were run to ensure reproducibility. The results of U-Th dating are displayed in Table 1. Age uncertainty is between 0.27 – 1.74 %. ^{238}U ranges between 27 – 1711 ppb. ^{232}Th is anonymously low, indicating that detrital thorium is a minor factor in age calculation. During HS1, TBR-14 grew from 17.03 - 15.4 ka BP in two different growth periods. The first growth period occurred from 17.03 - 15.85 ka BP. A growth hiatus occurs from 15.85 – 15.61 ka BP. The second growth period was from 15.61 – 15.4 ka BP.

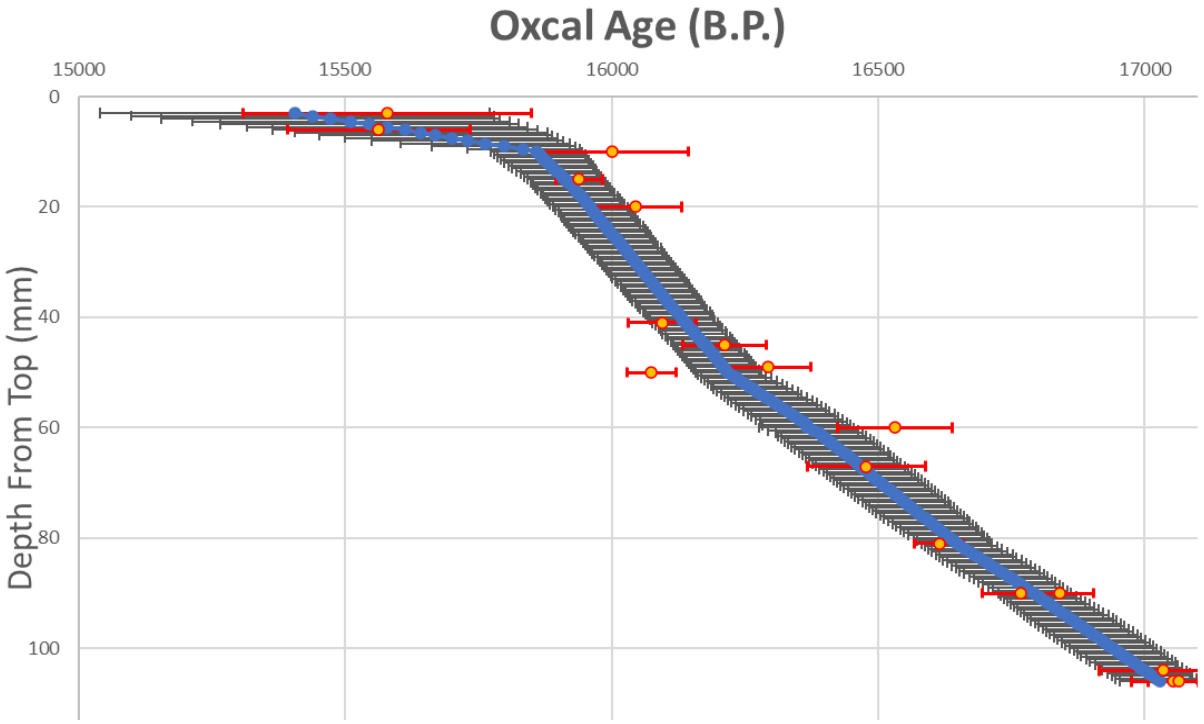

Figure 12: Oxcal Age – Depth Model. The blue line represents the average age while the grey outline marks the age uncertainty at each point. The yellow dots are the U/Th date measurements while the red line represents the age uncertainty.

Oxygen Isotopes:

The HS1 oxygen isotopic record is remarkably similar in structure to the nearby record of TBV-40 during HS4 (Wendt et al., 2019). The record (figure 13) consists of 3 separate, distinct phases defined by their relationship to the isotopic shift present within the record. These phases correspond to before (16.97 - 16.27 ka B.P.), during (16.27 - 16.16 ka B.P.), and after the oxygen isotopic shift (16.16 - 15.86 ka B.P.) and will be referred to as Section 1, Section 2, and Section 3 henceforth. Analysis of Section 1 begins at 16,970 B.P. and not 17,030 B.P., as the first 60 years of the dataset have anomalously high trace element concentrations, and CLFM is likely associated with hiatuses or the reactivation of the cave system. Data analysis is constrained to only the continuous growth period found with U-Th dating; therefore, Section 3 ends at the start of the 15.85 ka BP hiatus.

The highest $\delta^{18}O$ values and variability characterize the first phase, Section 1. The highest value found in this segment is -3.61‰ (VPBD), while the lowest value is -3.61‰ (VPBD). Section 1 has mean $\delta^{18}O$ values of -5.24‰ (VPBD) and a standard deviation of 0.63‰ (VPBD). Section 2 contains the most dramatic shifts in oxygen isotopic values. Section 2 starts at -5‰ and ends at -7.58‰ (VPBD). The end of Section 2 (16.16 ka B.P.) marks the sharpest transition in $\delta^{18}O$ values with a ~1.4‰ (VPBD) drop in ~2 years, as indicated by the growth bands. The drop is followed by a ~15-year trough in $\delta^{18}O$ values -7.58‰ (VPBD). Section 3 is characterized by low $\delta^{18}O$ values

that trend upwards through time, ending at -6.28‰ (VPBD). Mean values during Section 3 are -7.05‰ (VPBD) with a standard deviation of 0.4‰ (VPBD).

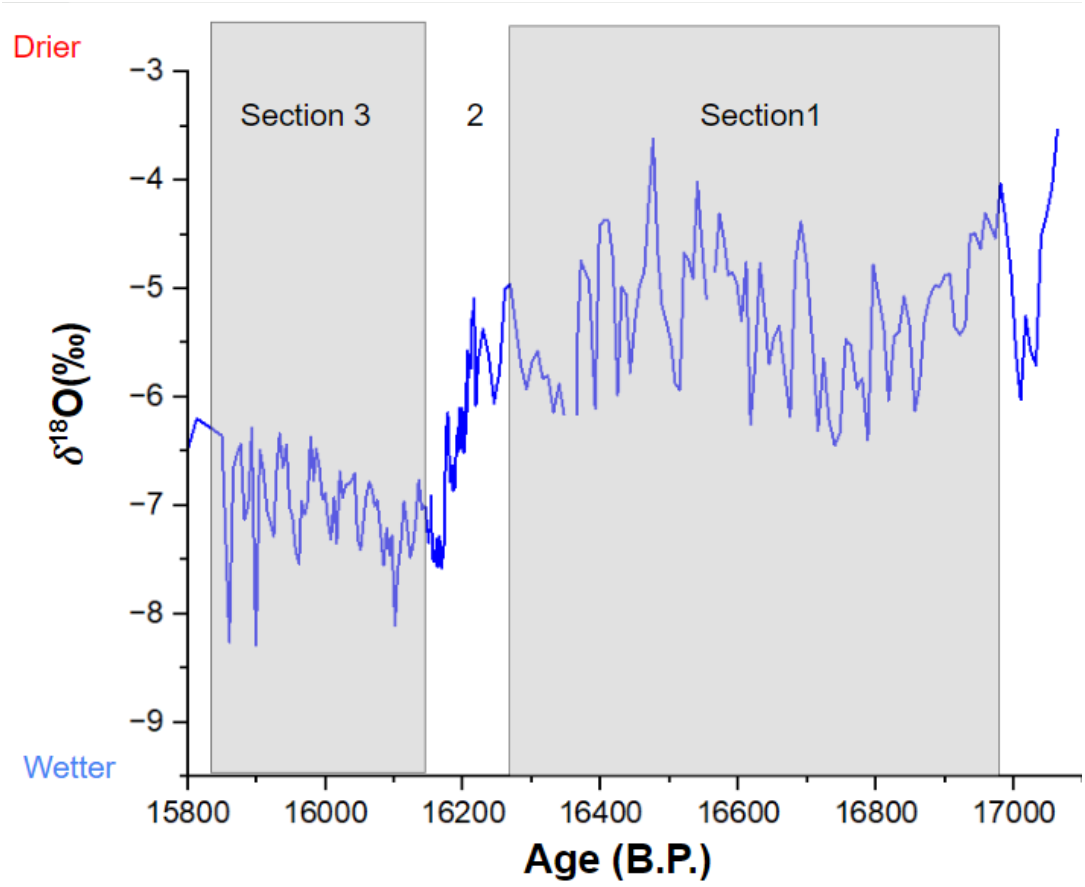

Figure 13: $\delta^{18}O$ values of TBR-14 throughout the HS1 main growth phase. The record shows a shift from higher values to lower values from Section 1 to Section 3.

Trace Elements:

Time series for Mg, Sr, Ba, U, and P for the whole record are shown in supplemental figure 3. To showcase the finer scale variability of each element, only the individual oxygen isotope sections are analyzed in this study. The time series for Mg, Sr, and Ba for the oxygen isotope sections are shown in Figure 14.

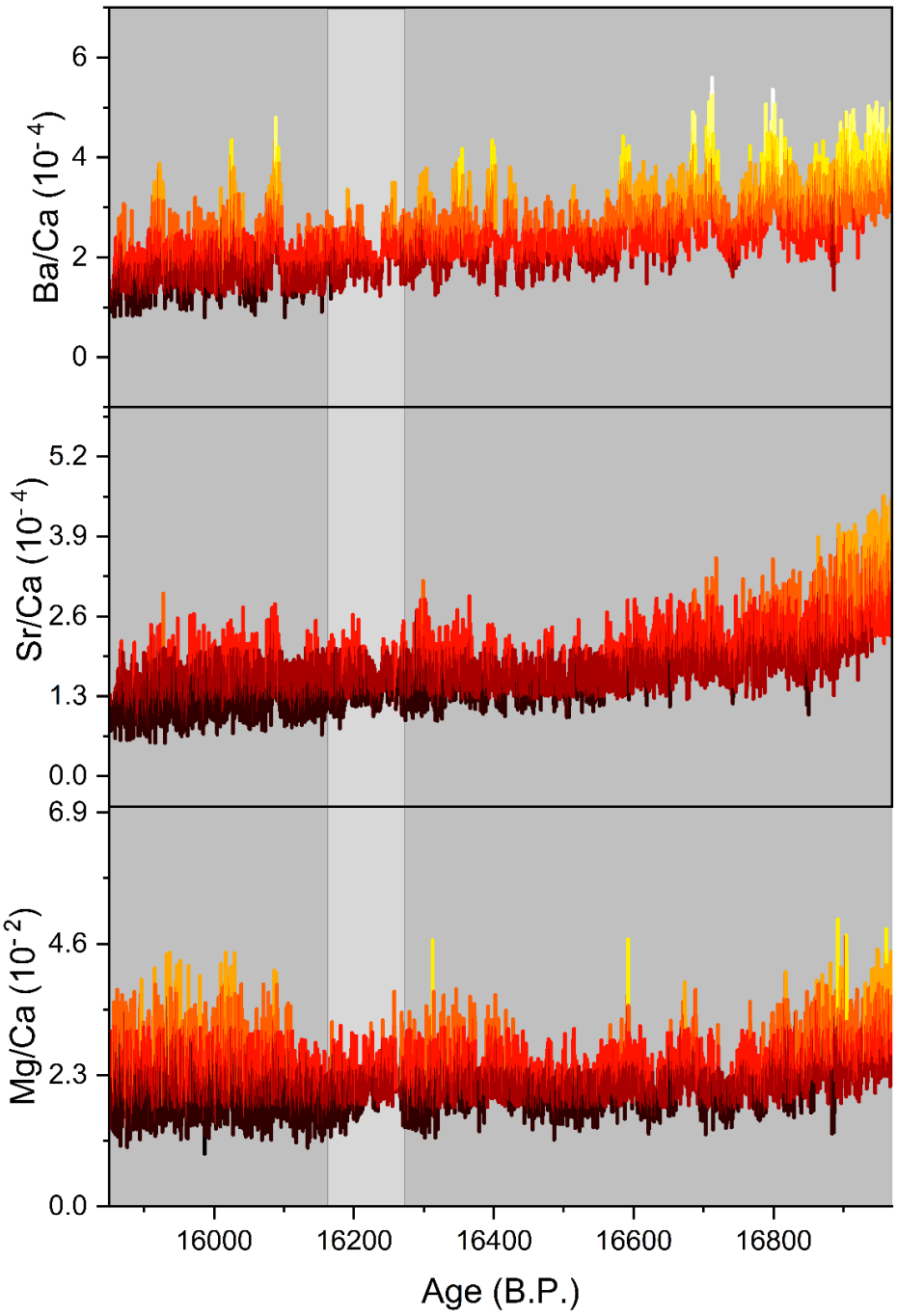

Figure 14: Ba/Ca, Sr/Ca, and Mg/Ca values throughout the main growth period. Values are the highest during Section 1 (right). Section 2 (light shade) has a stepped decrease in TM/Ca values and is consistently low. Mg/Ca in Section 3 (left) is highly variable and decouples from Sr/Ca and Ba/Ca. Sr/Ca and Ba/Ca are higher in Section 3 then 2 and have periodic pulses of high values.

Overall, the host rock elemental ratios experience a decline throughout the whole growth period. Statistics for elemental ratios for each section can be found in Table 2. Section 1 has the highest mean and max values for each element and the highest variability for Sr/Ca and Ba/Ca. Section 1 begins with high values of each host rock elemental ratio and generally declines throughout the section. Notable peaks in elemental ratios are seen at 16.59, 16.71, and 16.8 ka B.P.. These peaks are most distinguishable in Ba/Ca, while in Sr/Ca, they are the least apparent. In Section 2, there is a decrease in the elemental ratios of each element and low variability. Section 3 consists of a ~60-year period of low ratios and stability followed by a ~230-year period of high variability and oscillating values. At ~16.09 ka B.P., TM/Ca ratios increase for each element significantly, most notably for Ba/Ca. Peaks in Ba/Ca occur at 16.09, 16.03, 15.92, and 15.87 ka B.P.. Mg/Ca ratio variability is the highest in Section 3. The oscillating period within Section 3 is similar to Section 1 but has smaller elemental ratios.

Table 2: Brightness, P, Ba/Ca, Sr/Ca, and Mg/Ca ratios for each oxygen isotope section.

Brightness (pixel intensity)	Age	Mean	Min	Max	Std Deviation
Section 3	16.16 - 15.85	633.7424	294	1970	171.2873534
Section 2	16.27 - 16.16	802.9614	323	1797	202.0874659
Section 1	16.27 - 16.97	990.1475	322	2773	357.1095656
P (ppm)	Age	Mean	MiN	Max	Std Deviation
Section 3	16.16 - 15.85	67.52957	8.444116	204.2585	31.86655955
Section 2	16.27 - 16.16	101.6093	22.7483	213.4802	34.22134355
Section 1	16.27 - 16.97	106.8556	17.55424	247.5963	37.67860011
Ba/Ca	Age	Mean	Min	Max	Std Deviation
Section 3	16.16 - 15.85	0.000195	7.9348E-05	0.00048	5.30706E-05
Section 2	16.27 - 16.16	0.000209	0.000116487	0.00035	3.78031E-05
Section 1	16.27 - 16.97	0.000274	0.000124276	0.00056	6.81017E-05
Sr/Ca	Age	Mean	Min	Max	Std Deviation
Section 3	16.16 - 15.85	0.000139	5.42453E-05	0.000298	3.32636E-05
Section 2	16.27 - 16.16	0.000156	7.73476E-05	0.000263	2.71367E-05
Section 1	16.27 - 16.97	0.000197	9.00208E-05	0.000456	5.52481E-05
Mg/Ca	Age	Mean	Min	Max	Std Deviation
Section 3	16.16 - 15.85	0.022416	0.009188987	0.0445	0.005262331
Section 2	16.27 - 16.16	0.021316	0.012238363	0.037671	0.0035768
Section 1	16.27 - 16.97	0.023281	0.01167031	0.050313	0.004956635

The correlation between trace elements changes throughout each section, with higher host rock covariation seen at the beginning of the growth period than at the end. Section 1 has the highest covariation values among host rock elements (Sr-Ba= 0.78, Mg-Ba = 0.61, Mg-Sr =0.62) and the smallest anticorrelation of host rock elements with P (Mg-P= -0.16, Sr-P = -0.09, Ba-P = -0.26) in the record. Mg decouples from Sr and Ba in Section 2, while the covariation of Sr and Ba weakens (Sr-Ba= 0.64, Mg-Ba = 0.33, Mg-Sr =0.38). P is the most anticorrelated to host rock elements in Section 2 (Mg-P= -

0.34, Sr-P = -0.32, Ba-P = -0.37). Host rock cross-correlation remains lower in Section 3 (Sr-Ba= 0.62, Mg-Ba = 0.42, Mg-Sr =0.38). Host rock-P anticorrelation lessens in Section 3 (Mg-P= -0.17 , Sr-P = -0.09, Ba-P = -0.30). Correlation relationships between the elements can be seen in the PCA output. An example of the PCA output is seen in Supplemental figure 8.

Fluorescence and Phosphorus:

Supporting the findings of Orland et al. (2014), CLFM band intensity (brightness) and phosphorous were found to correlate (R^2=0.5037). The correlation value could be limited due to the inconsistent sampling rate of P resulting in the two variables not being on the exact same depth scale. A comparison of brightness values and P during each oxygen isotope section is seen in figure 16.

Like the alkaline Earth metal record, the first 60 years of speleothem growth during HS1 consists of extremely high values that are not seen in the rest of the record and thus will not be analyzed, as it mutes the variability seen in the rest of the record. The entire growth record is presented in supplemental figure 4. The two composite scan images of the whole confocal band record are available in supplemental figure 7.

Section 1 has two broad oscillating peaks in data and ends with a low plateau in band intensity values. Section 1 has high P concentrations and band intensity. Brightness values are the highest and most variable during Section 1, with a mean of 990 (pixel value) and a standard deviation of 357 (pixel values). The highest concentration of P is reached (247 ppm) and the mean value is high (106.85 ppm).

Hiatuses and the loss of the annual signal partly explain the high brightness and P values in Section 1. Section 1 contains several hiatuses denoted by transient peaks in the P record coinciding with an isolated bright singular confocal band (supplemental figure 5). Brightness values are also affected by the loss of the annual signal in confocal bands (supplemental figure 6). Annual signal loss results in bands blurring together and creating a brighter signal than if the bands were distinct and measured apart.

Section 2 has a rising trend in P and brightness and ends with comparatively high values (80-121 ppm; 490-790). Section 3 begins with relatively high P and brightness values (~200 ppm P and ~1250) which drop significantly at 16.1 ka B.P.. After the drop, P and brightness have reduced variability and values. The mean of both datasets is the lowest in Section 3. Brightness has a mean of 633 and a standard deviation of 171. P has a mean of 67 ppm and a standard deviation of 32 ppm.

Confocal imaging of Sections 2 and 3 reveals a bright confocal banding growth package (figure 15) between 16.19-16.1 ka B.P. (46.5 and 36 mm). As this section consistently contains distinct bright banding, the growth package likely reflects real growth, not hiatuses. Brightness and P values increase at the start of the package and remain at a regional high throughout the package. Alkaline Earth metals drop in concentration at the start of the package and reach their lowest concentrations throughout the continuous growth period. Additionally, $\delta^{18}O$ changes happen in phase with structural changes in banding characteristics. A comparison of confocal bands, $\delta^{18}O$, Ba/Ca, and P/Ca, during the bright growth package can be seen in figure 17.

The bright growth package has three stages based on banding characteristics: Stage 1(16.19 – 16.17 ka B.P.), Stage 2 (16.17-16.15 ka B.P.), and Stage 3 (16.15-16.1 ka B.P.). Stage 1 starts with an abrupt increase in brightness values reaching 1716 from the previous 682. Brightness values of the package are the highest in Stage 1. Stage 1 has eight bright confocal bands with the package's highest growth rates (~250 um). Stage 2 brightness values are stable around 950, and the growth rate is high (~180 um). Stage 2 contains ten distinct bands and double banding. Stage 3 has a declining trend in brightness and the lowest values of the package. Brightness starts at 1130 and declines to 716. Stage 3 ends with a single bright band at 985 (pixel value). The growth rate is the smallest in the package (~150 um) and banding is less distinct. A single, double band is positioned at the beginning of Stage 3.

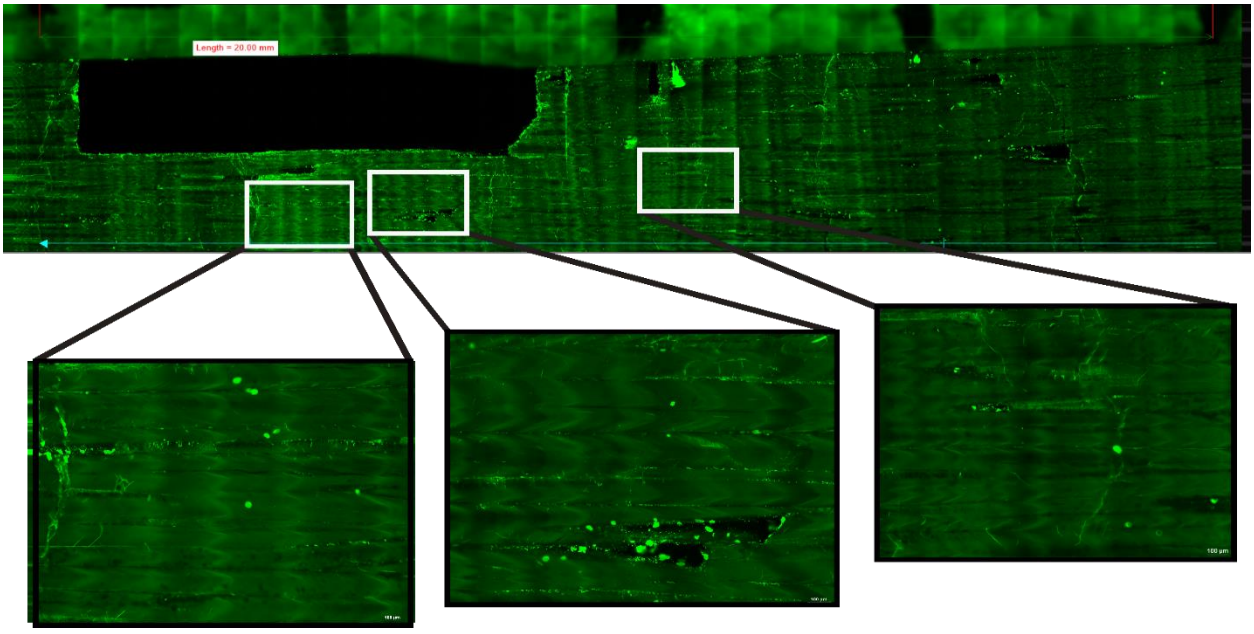

Figure 15: Confocal image from 50 mm to 30 mm depth (16.22 – 16.04 kyr B.P.). The right is stratigraphically up. Confocal brightness package from 46.5 and 36 mm (16.19-16.1 kyr B.P) is displayed. Dark rectangle is the high-resolution oxygen isotope trench. Stage 1 bands are wide and bright (Bottom left). Stage 2 bands are slightly smaller but have double banding (bottom center). Stage 3 bands have lower growth rates but are still distinct and bright in comparison to the rest of the record (bottom right).

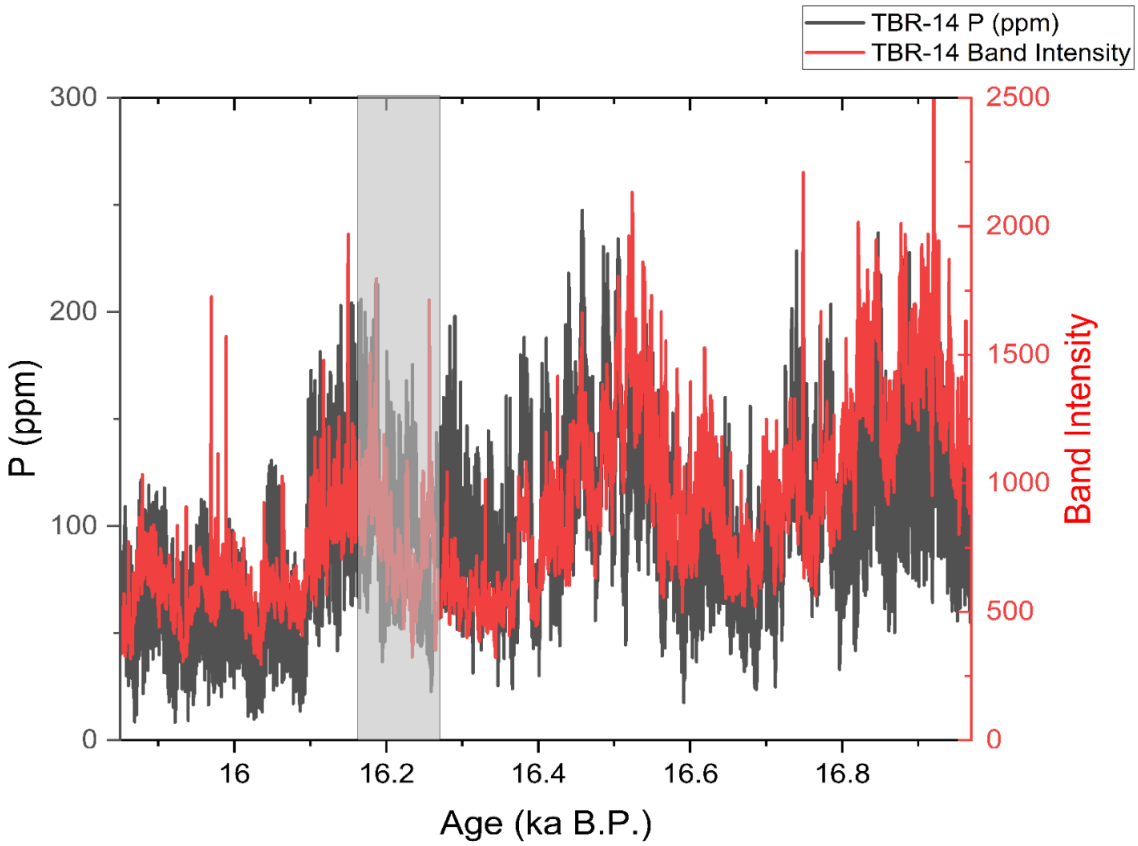

Figure 16: Fluorescent band intensity (red) and phosphorous concentrations (black) throughout the analyzed sections. The grey rectangle represents data from Section 2.

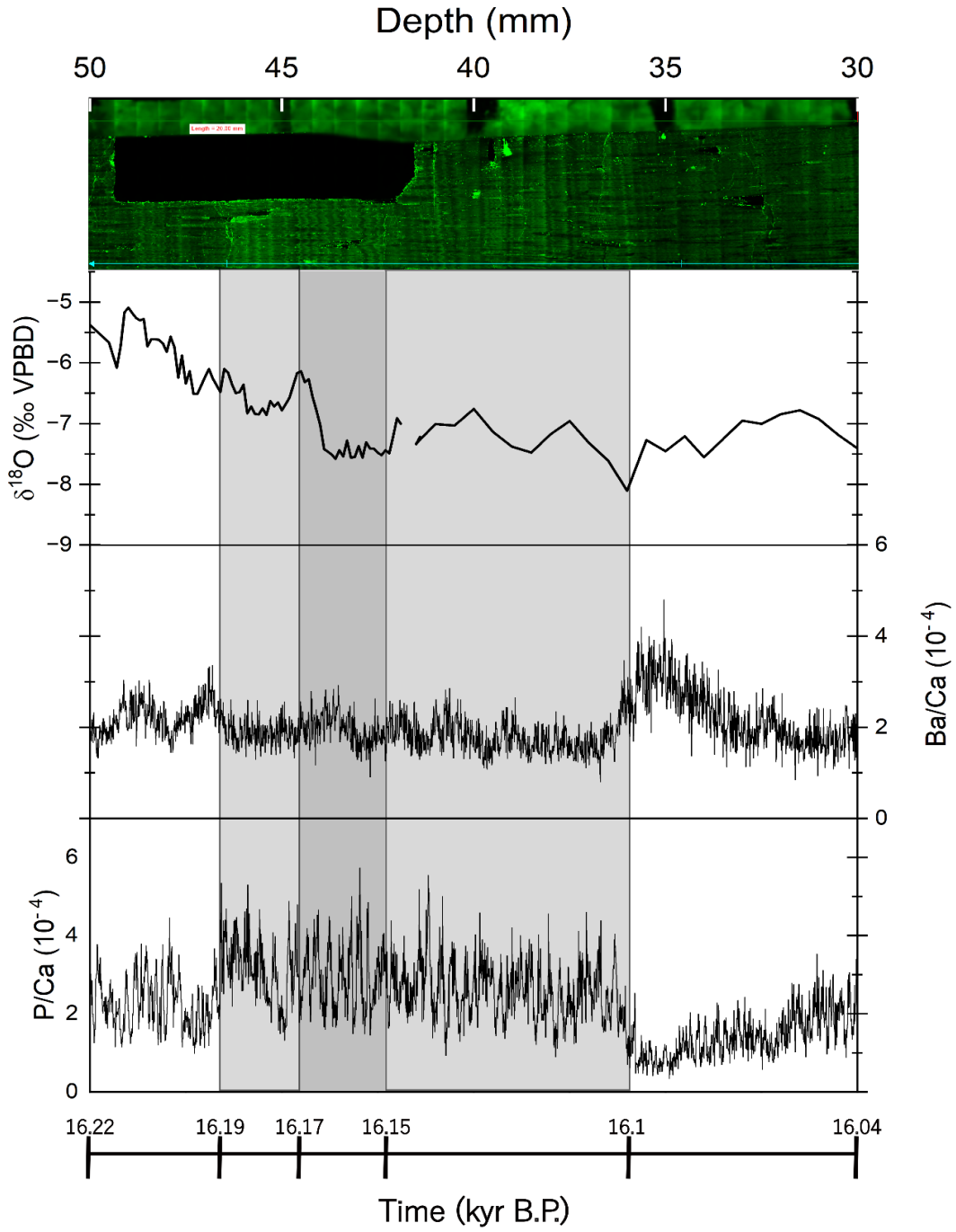

Figure 17: $\delta^{18}O$, Ba, and P timeseries during the bright growth package (shaded). During the bright growth package, Ba/Ca is low while P/Ca is high. Stage 1 has 8 bright confocal bands with the highest growth rates (~250 um) and a trough in $\delta^{18}O$. Stage 2 consists of 10 distinct bands with double banding and high growth rates (~180 um) and a ~1.4‰ drop in $\delta^{18}O$ followed by a consistent trough of low values (~7.5‰). Stage 3 has less bright and more variable banding with lower growth rates (~150 um). δ^{18} O values fluctuate around -7.3‰ and reach a minimum of -8.1‰ at 16.1 kyr B.P. After 16.1 kyr B.P., P/Ca drops while Ba/Ca rises sharply.

Band Counting:

WICOUNT and manual band counting methods returned similar band counts (Table 3) throughout the record, with the total difference being only 3-6%. The close agreement between the two methods suggests Oriani's (2022) WICOUNT software is a robust band-counting method and should be used in the future. However, both methods found that the number of bands was smaller than the time that passed during the continuous growth phase. WICOUNT was 85 – 88 % of the U-Th derived time range, while the manually counted bands accounted for 83 % of the U-Th time range. This discrepancy implies that the confocal bands are not continuously annual. Likely, short hiatuses are present in the record that are small enough that they are not seen in U-Th dating. This conclusion is supported by transient peaks in the P record that coincide with isolated bright single confocal bands. Minor hiatuses create the largest discrepancies during Section 1, where the band count sum is consistently lower than the time passed. Annual banding is the most prevalent during Section 3, where the counted band sum is the closest to the U-Th derived time range for a given 10mm segment.

Table 3: The number of bands counted manually and with WICOUNT compared to U/Th based age model.

Age B.P.	Section	Bands WICOUNT	Bands Manually Counted	U/Th years
15.86-15.96	10-20 mm	102	111	102
15.96-16.04	20-30 mm	84	87	84
16.04-16.13	30-40 mm	78	68	85
16.13-16.22	40-50 mm	76-111	58	89
16.22-16.37	50-60 mm	100	99	147
16.37-16.51	60-70 mm	127	110	140
16.51-16.64	70-80 mm	108	95	130
16.64-16.79	80-90 mm	67	67	158
16.79-16.94	90-100 mn	97	91	148
16.94-17.02	100-110 m	158	183	87
	Total	997-1032	969	1170

Discussion:

Movement of the ITCZ Inferred From $\delta^{18}O$ (Comparison with other records)

The foundational study of speleothems in NE Brazil discovered that speleothem growth periods corresponded to Heinrich stadials and related the growth to a southward shift in the ITCZ (Wang et al., 2004). At the time, research studies had suggested the ITCZ would shift south during Heinrich stadials, but no direct or well dated proxy evidence existed. Wang et al. (2004) provided an essential contribution to the theory by presenting proof that the ITCZ did indeed shift south during Heinrich stadials. Studies of TBV and TBR focused on HS4, HS6, and HS11 furthered this claim by adding $\delta^{18}O$ records tied to the speleothem growth (Wendt et al., 2018; Berry, 2018). Currently on the precipice of the annual ITCZ trajectory, the absolutely dated TBR-14 record is ideally situated to constrain the southwards movement of the ITCZ spatially and temporally during HS1 through the $\delta^{18}O$ record. If speleothem growth is connected to movement of the ITCZ, an anticorrelated climate signal should be observable between TBR and climate records north of the ITCZ. Additionally, other records south of the ITCZ should have a similar signal to TBR. Localized climate proxies should illustrate increased wet conditions as well to ensure that the $\delta^{18}O$ values are not only reflective of upstream regional effects. The paleoclimate proxies of the TBR-14 record support the

hypothesis that a southward shift in the ITCZ occurred and caused NE Brazil to become wetter.

A common question in paleoclimatology asks whether $\delta^{18}O$ accurately reflects regional hydroclimate changes, especially in the tropics. When considered alone, local climate interpretation of $\delta^{18}O$ can be limited, as $\delta^{18}O$ can vary from more than just local changes in precipitation amount (Cruz et al., 2007). However, precipitation and ecological biome shifts in NE Brazil are well documented in paleo-records (Arz et al., 1998; Jennerjahn et al., 2004; Jaeschke et al., 2007; Dupont et al., 2010). These shifts are particularly valuable to understand since Caatinga replacement by wetter vegetation may have served as an ecological bridge between the eastern Amazonian and the Atlantic forests, thus permitting the exchange of species and increasing biodiversity (Costa et al., 2003, De Oliveira et al., 1999). The palynological and terrestrial runoff evidence of GeoB3912 and GeoB3910-2 displays a two-phased vegetational change akin to the precipitation shift seen in the TBR-14 $\delta^{18}O$ record (figure 18). The vegetational shift is seen with a decrease in Caatinga pollen representation across HS1, increased precipitation suggested by a larger makeup of non-arid plant species and organic carbon in runoff, and soil development through a decrease in erosional rates (Dupont et al., 2010). The marine core records were radiocarbon dated. The exact timing of the recorded ecological and precipitation change in the marine core is uncertain due to reservoir age effects and lower temporal resolution (Dupont et al., 2010). The timing of the shift recorded in the $\delta^{18}O$ record is well constrained due to U-

Th dating and may serve as a better framework for understanding the timing of ecological change within GeoB3912 and GeoB3910-2.

The TBR-14 speleothem record of PCP trace element indices, fluorescent banding, and P/Ca provides a detailed point-source account of how aridity and precipitation changed through HS1 with a precise timeline on a local scale (figure 20). These proxies show that aridity was prevalent during the first phase of vegetational growth, the soil was less developed, and prolonged dry periods were standard. The second phase of vegetation succession started at ~16.19 ka B.P.. From 16.19-16.1 ka B.P., the region received the most rainfall and exhibited the shortest dry season. Double banding within this period suggests vegetational development may have resulted from the region receiving two rainy seasons in one year. After 16.1 ka B.P., aridity increased but was markedly lower than in phase 1. Combining the high precision dating potential of speleothems with the palynological record from neighboring marine sediment cores can produce a more complete picture of the hydroclimate and paleoecology variability across NE Brazil during Heinrich Stadial 1. Changes in the TBR-14 $\delta^{18}O$ record coincide with local climate change as observed in terrestrial runoff, pollen, PCP, P/Ca, and fluorescent banding.

TBR-14 tracks the $\delta^{18}O$ Paixão record closely. In both records, $\delta^{18}O$ can be used to infer changes in rainfall, with decreases indicating wetter conditions in the region through time. TBR-14 and PX7 have similar structures with higher (drier) values in Section 1 and lower (wetter) values in Section 2, with a return to higher values during Section 3. PX7 contains a 2‰ drop that is synchronous with the 1.4‰ drop found within

TBR. Taken together, Northeast Brazil is experiencing wetter conditions regionally throughout HS1, and at ~16.16 ka, the climate abruptly changes to even wetter conditions.

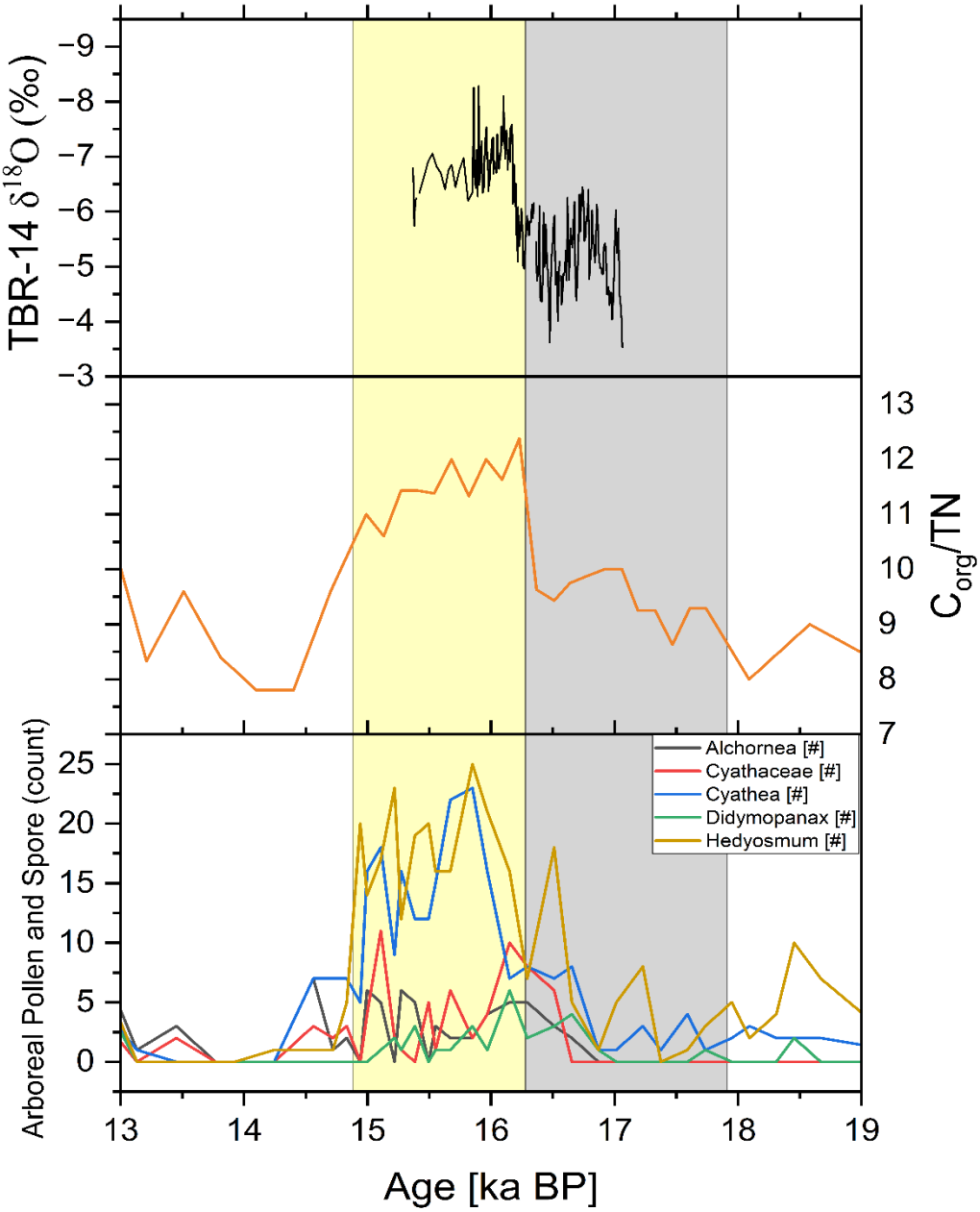

Figure 18: The two phased vegetation and organic matter runoff shift documented in GeoB 3910-2 is present in the TBR-14 $\delta^{18}O$ record. The transition to lighter $\delta^{18}O$ is accompanied by a shift to more humid plants. Modified from Wendt thesis (2015)

The Cariaco basin sediment core, representative of the northern branch of the ITCZ, is anticorrelated to Northeast Brazil. High reflectance values within the record are caused by a larger contribution of carbonate precipitation and smaller terrigenous carbon input in the basin. This occurs when there is decreased terrestrial runoff and is interpreted as a decrease in rainfall and increased aridity. Throughout the TBR-14 growth period, the reflectance values of the sediment core are higher than usual. Near the $\delta^{18}O$ drop recorded in TBR-14, reflectance values reach 100%, the highest values of the ~100,000-year record. While Northeast Brazil became wetter during HS1, the Cariaco Basin was very dry. The antiphase relationship between Northeast Brazil and the Cariaco Basin could occur if the mean latitudinal range of the ITCZ shifted south. Southwards displacement of the ITCZ would gradually reduce the amount of rainfall the Cariaco Basin received while increasing the amount of rainfall of Northeast Brazil to the south of the ITCZ. If the ITCZ shifted far enough south, the Cariaco Basin would fall outside of the ITCZ entirely, while Northeast Brazil would be at its wettest.

Similar to the Cariaco basin, Chinese Monsoon records mirror $\delta^{18}O$ in NE Brazil. The Chinese monsoon records like YT from Hulu Cave (Wang et al., 2001) and SM7 from Shima cave (Liang et al., 2020) have a two-phased $\delta^{18}O$ structure with a rapid shift in $\delta^{18}O$ between phases. This structure is opposite to that of NE Brazil; in these records, values shift to heavier $\delta^{18}O$ values. As these records are constructed from U-Th dated speleothems, the timing of the two phases and the isotopic shift are well constrained. The timing of the shift to a drier China and weaker monsoon is coeval with the shift to a wetter NE Brazil.

On all spatial scales, the TBR-14 record has a climatically significant signal (figure 19). Locally, the changes in $\delta^{18}O$ are concurrent with changes in environmental and climatic signals documented in the record as well as with nearby palynological and sediment cores. Regionally, the $\delta^{18}O$ pattern is replicated to nearby records and opposite records north of the ITCZ. This observation signifies that δ18O is reflective of broad-scale changes in atmospheric circulation. Globally, the $\delta^{18}O$ pattern appears significant due to its coeval anticorrelation to the Chinese monsoon records. The TBR-14 record fulfills the requirements discussed for interpreting change within the record as a function of shifts in the latitudinal range of the ITCZ.

With the requirements fulfilled, the movement of the ITCZ during HS1 can be investigated. At 17.03 ka B.P., the ITCZ was displaced far enough south for speleothem growth to begin. Between 17.03 – 16.27 ka B.P., ITCZ coverage of the region was variable. From 16.27– 16.16 ka B.P., The ITCZ shifted southwards dramatically, culminating in the ~1.4‰ (VPBD) drop. After 16.16 ka B.P., the range of the ITCZ began to return northwards which terminated speleothem growth.

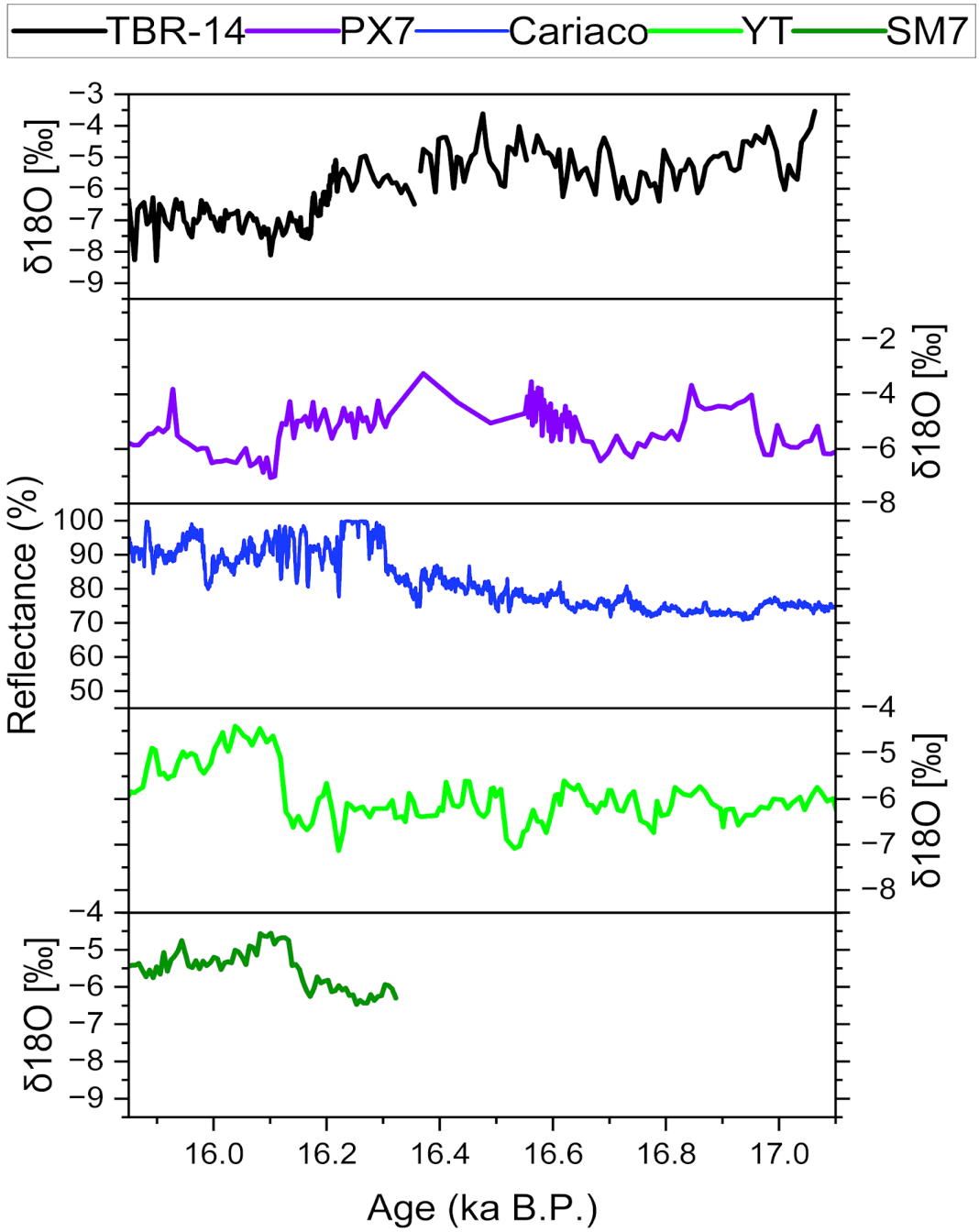

Figure 19: $\delta^{18}O$ and reflectance changes in paleoclimate records from across the globe. TBR-14, PX7, and the Cariaco Basin are from South America. YT and SM7 are from China. Each record shows two distinct phases. Records to the south of the ITCZ are similar to TBR-14 while records to the north have an opposite structure.

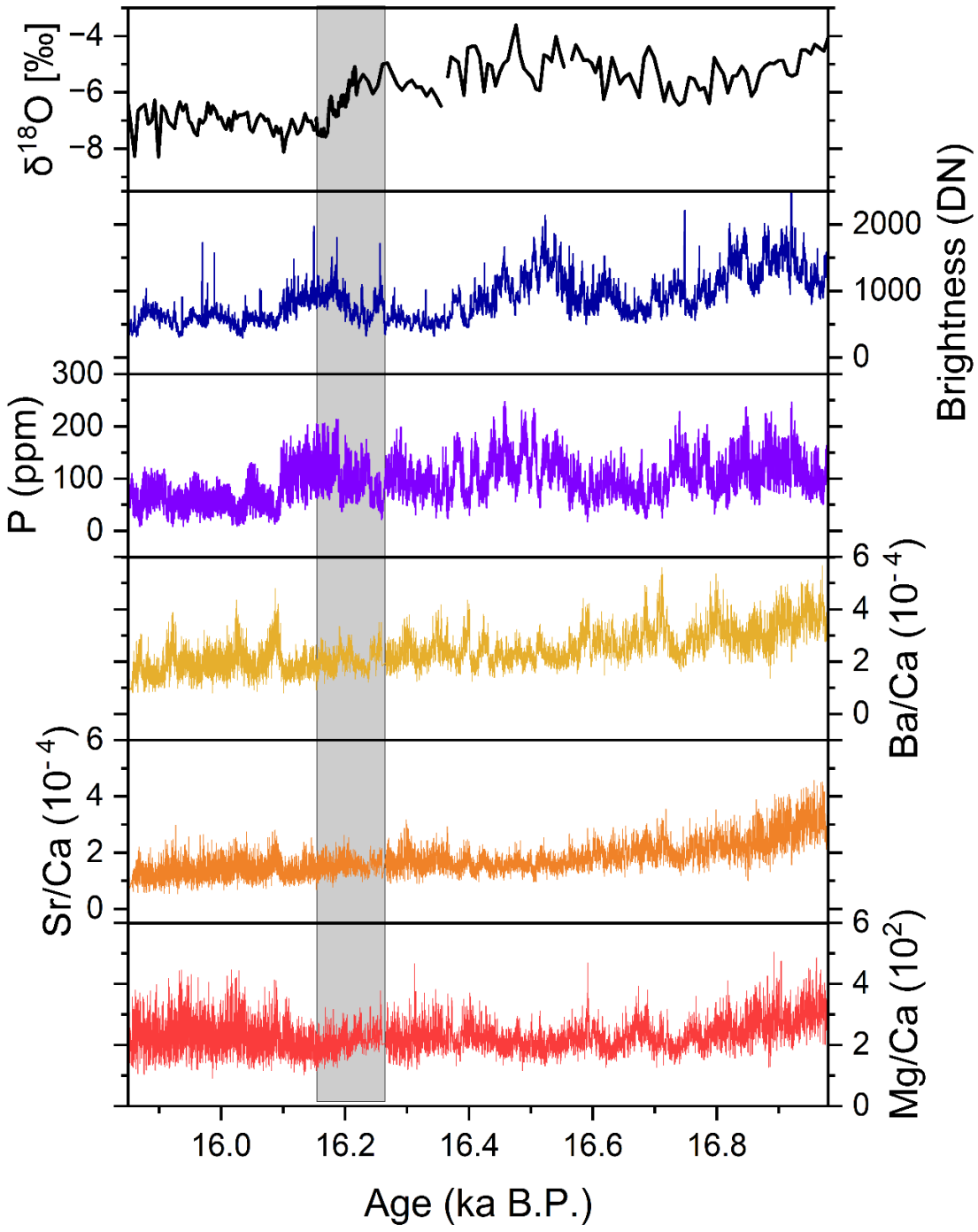

Figure 20: Comparison of each TBR-14 dataset throughout HS1. Section 1 is to the left of the shaded box. Section 2 is the shaded box, Section 3 is to the right of the shaded box.

Pluvial Phase 1 (Section 1):

Section 1 was markedly wetter than background climate conditions but drier than other growth sections. The 21,000-year absence of speleothem growth prior to Section 1 suggests the region had a water deficit that prohibited speleothem growth. The initiation of speleothem growth (17.03 ka B.P.) at the start of Section 1 is strong evidence that climate became wetter. However, the prevalence of PCP, vegetational makeup of Northeast Brazil, high $\delta^{18}O$ values, and the confocal and P/Ca records suggest that Section 1 was the driest period during the growth period.

During Section 1, NE Brazil was on the fringes of the ITCZ and not the core as indicated by the higher oxygen isotope values. Rainfall in this situation will be greater than previous background levels, i.e. when the speleothem was not growing, but have limited distribution throughout the year. Rainfall distribution was likely confined to the austral summer followed by an 8-month dry season (Jennerjahn et al., 2004). Vegetation type during Section 1 is characteristic of these climate conditions.

Proxies from Northeast Brazil's continental margin and Lagoa do Caçó suggest that the first phase of the Heinrich associated pluvial period was transitional, as evidenced by the background caatinga environments slowly diminishing and pioneer species taking hold. The long dry season hindered rainforest development, but the increase in rainfall during the summer promoted soil erosion and an increase of pioneer species (Jennerjahn et al., 2004). Lagoa do Caçó records a low percentage of arboreal

pollen and GeoB3910 documents an increase in fern spores (Ledru et al., 2002; Dupont et al., 2010). During this period, gallery rainforests began to develop. Based on the high Fe/Ca and Ti/Ca ratios and low organic carbon levels found in marine cores, it can be inferred that erosional rates were elevated (Jennerjahn et al., 2004; Jaeschke et al., 2007). The high erosional rates are likely due to higher than background precipitation falling on a sparsely vegetated, primarily caatinga landscape with poor soil.

A key indicator of the high aridity present during Section 1 is the prevalence of PCP. High concentrations of Mg/Ca, Ba/Ca, and Sr/Ca along with covariation of the alkaline earth metals indicate that PCP was the highest during Section 1. As PCP occurs more frequently during arid conditions, it is likely that the region was drier and had a long dry season. The overall trend to lower concentrations of Mg/Ca, Ba/Ca, and Sr/Ca throughout Section 1 insinuates a general decrease in aridity through time. A low frequency climatic signal may be affecting PCP ratios, causing the sinusoidal peaks to appear approximately every 90-110 years.

The confocal banding of Section 1 reveals that the climate was inconsistent interannually and relatively dry. Band counting was the furthest removed from U-Th time in Section 1 signifying non-annual growth. The loss of annual banding occurs when the climate is inconsistently wet with some years not receiving enough rainfall for speleothem growth. Growth hiatuses are also common in this period shown through transient bright confocal bands alongside high P/Ca values. Growth hiatuses occur when several or more years consistently do not receive enough rainfall for speleothem growth. Like modern day conditions, locations on the outermost edge of the annual

ITCZ trajectory are not always covered by the ITCZ. Failure of the ITCZ to reach TBR would result in the cessation of growth and hiatuses in the record seen in the confocal band record.

P/Ca ratios are hard to interpret during Section 1 but likely are not primarily influenced by total rainfall amount. Higher erosion during the time period (Jennerjahn et al., 2004) signifies that the transport of soil colloids into the cave was more easily facilitated. In this situation, the P/Ca signal in stalagmites could be high with modest increases in rainfall because the flushing of soil colloids was more efficient. The precipitation regime may have also contributed to the high P/Ca signal. The long dry season would prohibit the transport of phosphorous colloids for most of the year. Then, during the high intensity summer rainfall, the colloids would be flushed resulting in a high concentration of P/Ca centered on a single event. This climate regime would cause higher P/Ca values than an environment where the distribution of rainfall is more consistent throughout the year (Frisia et al., 2012). The high variability of P/Ca during Section 1 could reflect high interannual rainfall variability with low values occurring during drought years. The higher P/Ca signal in Section 1 likely was a function of poor soil quality and sparse vegetation.

The Pluvial Transition (Bright Confocal Growth Package):

The bright confocal growth package (figure 17) between 16.19-16.1 ka B.P. is likely the wettest period of the entire record. Throughout the package, the growth rate is consistently high, brightness corresponds to oxygen isotope changes, PCP is minimal, and soil flushing is high. PCP is inferred to be minimal, as the elemental ratios are at a

record minimum and have low correlation values. During this period, Mg/Ca decouples from Ba/Ca and Sr/Ca. Ba/Ca and Sr/Ca become less correlated as well. As PCP increases with aridity, a minimum in PCP suggests the period was wet and that water residence time in the epikarst was low. The package also contains a local high in P/Ca and brightness values. P/Ca and brightness can be difficult to interpret as they are not solely a function of rainfall (soil flushing), but also of vegetation type, vegetation density, and soil quality. By comparing the P/Ca signal to other proxies, it is possible to distinguish what factor is most influential in P/Ca ratios. The interpretation of P/Ca as a rainfall indicator is more reliable if other proxies suggest wetter conditions. The shift in P/Ca corresponds to increased growth rate, decreases in $\delta^{18}O$, and an exact anticorrelated relationship with Ba/Ca. Therefore, P/Ca can be viewed as a function of increased rainfall during the growth package. Sub-package climatic change can be investigated by looking at how band brightness, confocal banding structure, and $\delta^{18}O$ change within the growth package.

Stage 1 begins with an abrupt shift to a wetter climate. The near instantaneous transition to bright and wide confocal banding alongside a drop in PCP indices and increase in P/Ca at the initiation of Stage 1 all suggest the local climate became wetter. Stage 1 occurs during a sustained trough in $\delta^{18}O$. The wetter conditions inferred by the proxies during Stage 1 coinciding with lower $\delta^{18}O$ values are concurrent with the idea of a sustained southwards displacement of the ITCZ. Stage 1 is interpreted to be the second wettest stage in the growth package even though the confocal banding is the brightest. The banding structure of Stage 1 is characterized by singular bands and not

double bands like the banding present in Stage 2. This structure could exist under a climate system where the ITCZ is far enough displaced to greatly increase the level of rainfall amount at the site but does not reach the displacement required to cause two distinct rainfall seasons. Under this climatic regime, FOM would be more concentrated and brighter than a system with two rainy seasons. Annually it would receive less rainfall than a climate regime with two rainfall maxima.

Stage 2 contains the sharpest $\delta^{18}O$ shift present in the record. Confocal imagery and the high resolution of the oxygen isotope trench in the TBR-14 record makes it possible to investigate the oxygen isotope shift at an annual resolution level. A close-up of the oxygen isotope drop is shown in figure 21. The speed of climate change is estimated from the confocal banding. Due to the clear, distinct banding, it is likely that the banding is annual and that no hiatuses are present. The oxygen isotope drop found within Stage 2 occurs in just two years as evident by the confocal overlay.

The dramatic transition in confocal banding structure to double bright bands in Stage 2 accompanies the oxygen isotopes drop and the subsequent $\delta^{18}O$ trough. Sustained low oxygen isotope values with low variability indicate that the ITCZ was reliably displaced south enough to cover NE Brazil for prolonged periods of time. Banding structure correlating with oxygen isotope changes is clear evidence that $\delta^{18}O$ is connected to local climate and not just upstream effects. The minimum in PCP with higher soil flushing during this period supports this claim as well. Double bright banding is almost exclusive to Stage 2 and signifies the region received two rainy seasons in one year. This could be possible if the ITCZ is displaced far enough south that

Northeast Brazil becomes centralized in the ITCZ, resulting in two separate rainy seasons. The first wet season would occur as the main locus of precipitation shifts between the southern and northern most extents of the ITCZ. The second wet season would occur as the ITCZ shifts from the northern to southern most extent of the ITCZ.

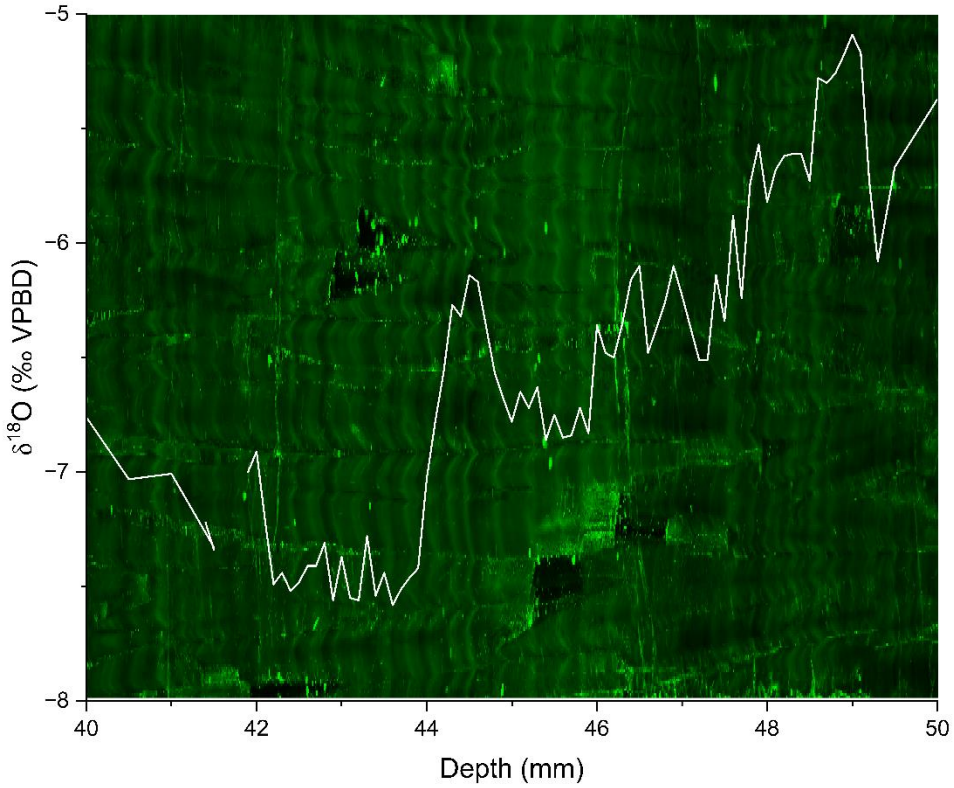

Figure 21: Oxygen isotopes with confocal overlay. The drop occurs ~44.25 mm. Time is moving to the left. 50 mm equates to 16.22 ka B.P. and 40 mm equates to 16.13 ka B.P. . Age uncertainty is =/- 60 years. The drop occurs at 16.16 ka BP which is within error of the Hulu Cave oxygen isotope shift. The whole drop occurs over 3 bands while the majority of the drop occurs over 2 bands. The oxygen isotope drop and subsequent trough is characterized by double bands adding confidence to the climatic impact of the isotope change at the cave site.

Stage 3 contains a singular double band but is overall characterized by a return to single bright bands, less distinct banding, and lower growth rates. The return to single bright bands signifies the loss of two annual wet seasons. Lower growth rates and less distinct banding indicate a reduction in rainfall. The $\delta^{18}O$ variability and inconsistent banding brightness seen in Stage 3 may reflect a less consistent latitudinal range of the ITCZ resulting in higher interannual rainfall variability. These characteristics imply that Northeast Brazil was returning to drier conditions and had passed the peak of precipitation reached in Stage 2. Throughout Stage 3, the latitudinal range of the ITCZ progressively moved northwards.

Pluvial Phase 2 (Section 3):

Section 3 is characterized by a general drying trend punctuated by several short-term aridity events. The section was drier than during the bright confocal package but was notably less arid than Section 1 as indicated by lower $\delta^{18}O$ and PCP values as well as a diverse pollen assemblage. Starting with Stage 3 and continuing until the end of the speleothem growth period, Section 3 saw the gradual return of the ITCZ latitudinal range to background levels and away from NE Brazil. The movement is reflected in the trending upwards values of $\delta^{18}O$ throughout Section 3, indicating a continuous shift northward. The eventual removal of the ITCZ from the study site is inferred from the cessation of speleothem growth.

The strongest evidence for Section 3 being wetter than Section 1 exists in the pollen record. During Section 3, the amount and percentage of pollen and spore from Alchornea, Cyathaceae, Cyathea, Didymopanax, and Heydyosmum in GeoB3910-2 is

significantly higher than in Section 1 (Dupont et al., 2010). These arboreal species require high moisture and are not tolerant of long dry seasons. Their presence suggests that the length of the dry season was shorter than 4 months (Jennerjahn et al., 2004).

An increase in Mg/Ca, Ba/Ca, and Sr/Ca after Stage 3 reveals that PCP becomes more prevalent than during the bright confocal growth package. However, the continued decoupling of Mg/Ca with Ba/Ca and Sr/Ca in addition to the lower values of Ba/Ca and Sr/Ca implies that the process is not occurring to the extent observed in Section 1. These two observations are in line with the inferred positioning of the ITCZ. As the ITCZ is rebounding from the maximum displacement observed during the bright confocal growth package, the climate will be drier, causing the epikarst to have more frequent PCP. If the displacement in the period is greater than Section 1, the region will be less arid and have less extensive PCP, resulting in lower Ba/Ca, Mg/Ca, and Sr/Ca ratios.

Spikes in Ba/Ca during Section 3 suggest that periods of high PCP and aridity may have occurred throughout the Section. The Sr/Ca and Mg/Ca signals show a clear rise in values only in the first peak ~16.09 ka B.P.. Other peaks observed in the Ba/Ca ratio are present but not prominent. This could signify that PCP is becoming a less influential process impacting Sr/Ca and Mg/Ca ratios, as both signals have a lot of noise, making them harder to interpret as climate signals. The validity of these signals as an indicator of PCP and by extension aridity during Section 3 is reinforced when compared to the brightness and P/Ca signals. At each peak in Ba/Ca there is a coinciding trough in P/Ca and confocal band brightness.

Confocal banding and P/Ca are difficult to interpret in Section 3 but are most likely related to vegetation change modulated by rainfall. The close correspondence between confocal band counts and U-Th years implies that growth was consistent and annual throughout the section. The disappearance of confocal banding near the end of the speleothem growth period is a strong indicator that the landscape became drier at the end of the record. During Section 3, the P/Ca and band brightness signals are muted and lower than the rest of the record. The anticorrelated relationship of band brightness and P/Ca to PCP ratios indicates that the signal is still responding to aridity and rainfall, but the subdued nature of the signal indicates that the FOM and colloidal systems were significantly altered from previous periods. The two main factors that could change in the system are reservoir size and transport efficiency of FOM, both of which may be changed by vegetation and vegetation density. Arboreal pollen assemblages document changes in both the plant species and amounts of plants present at this time (Jennerjahn et al., 2004; De Olivieira et al., 1999; Behling et al. 2000; Dupont et al., 2010). Borsato et al. (2007) found that the P/Ca signal was higher after deforestation. Perhaps, the opposite trend would be observed after vegetation density above the cave increased. Higher vegetation density would reduce erosion and lead to greater retention of FOM and P colloids, causing a reduced flux of P and FOM into the cave during infiltration events. Under this scenario, the P/Ca and band brightness signal would respond to infiltration events, but the magnitude of the response would be reduced. Future studies aimed at the interplay between vegetation, soil, and

speleothem P and band brightness could be a vital component of future paleoclimate speleothem research.

16.1 ka BP event:

The significance of the oxygen isotope drop in Stage 2 is reinforced when comparing the record to Chinese Monsoon records like YT from Hulu cave and SM7 from Shima Cave (Wang et al., 2001; Liang et al., 2020). Throughout China, there is a unified shift of ~2‰ to higher $\delta^{18}O$ values around ~16.1 ka B.P. (Wang et al., 2001; Li et al., 2019; Zhang et al., 2018). The YT record placed this change at 16.06 ka B.P.. SIMS analysis of the YT record showed that the isotopic shift occurred in six years, with most of the shift occurring in just two years (Treble et al., 2007). Although the shift occurs simultaneously throughout the Chinese monsoon records, the rate of the change has not been replicated. The duration of the isotopic shift in TBR-14 was found to be identical to YT. The two-year isotopic shift found within both records is an exceptionally rare example of abrupt climate change within paleoclimatology. The occurrence of the shift found in records throughout the world is unambiguous evidence that the event is globally significant.

The antiphase relationship between China and Northeast Brazil is a clear manifestation of a teleconnection as both region's climate change at the same time. In China, the change corresponds to a weaker monsoon and drier climate (Wang et al., 2001; Zhou et al., 2016). This change could indicate that the strength of the EASM is in part a function of the latitudinal position of the ITCZ. Paleorecords from the South China

Sea and the Flores Sea support this argument as they record a southward shift of the ITCZ in the Indo-Pacific synchronous with the shift documented in TBR-14 and the Chinese Monsoon (Huang et al., 2019). An alternative explanation for this teleconnection is that the movement of the ITCZ is responding to the same forcing mechanism as the atmospheric circulation changes behind the weakening of the EASM. Although the cause is unknown, the established teleconnection allows climate change in both regions to be better understood through studying the other. The mirrored $\delta^{18}O$ pattern found in China supports the argument that the climate change seen in Northeast Brazil $\delta^{18}O$ record is occurring on a broad scale and is significant. The fast growth rate alongside the high-resolution proxies of TBR-14 allow for an in-depth analysis of the $\delta^{18}O$ shift not feasible in most Chinese cave records due to their lower growth rates preventing sub-decadal events to be resolved.

The abrupt global shift observed between 16.1-16.2 ka B.P. may originate from the Heinrich event and the mass export of icebergs. This forcing mechanism would match the rate of climate change observed in the records as ice cover in the North Atlantic would rapidly change during a Heinrich event. Higher ice cover would amplify the climate forcings already occurring during the Heinrich stadial by further cooling the atmosphere, strengthening atmospheric pressure gradients, and intensifying the Northeast trade winds (Chiang et al., 2008). The existence of spontaneous widespread iceberg cover in the North Atlantic is supported by the synchronous deposition of IRD in the North Atlantic core U1308, but the timing of IRD deposition in the North Atlantic is

not agreed upon (Hodell et al., 2017). It should be noted that the iceberg discharge shown in the IRD record is not sea ice, but icebergs calved from ice sheets.

For ice rafting to be the cause of the 16.1 ka event, peak IRD deposition needs to align with the event. In core U1308, two IRD peaks are documented during HS1 at 16.2 ka and 15.1 ka; the larger IRD peak is within error of the 16.1 ka event (Hodell et al., 2017). An IRD stack of 15 marine core records also algins with the 16.1 ka event (Lisiecki and Stern, 2013). However, disagreement is found between cores in the timing of IRD delivery in the North Atlantic. Two IRD peaks were also found in the Iberian Margin core, SU81-18, but were dated at 17.5 ka and 16 ka, with the 17.5 ka peak being the larger of the two (Bard et al., 2000). The ^{14}C ages of SU81-18 have a two-sigma age uncertainty of 600 years (Bard et al., 1989) making it possible that the second peak corresponds to the 16.1 ka event. The lack of detrital carbonate found in the second IRD peak of SU81-18 weakens this interpretation by indicating the IRD was not sourced from Canada. Hodell et al. (2017) argue that Bard's dates are not correct since Bard used a constant reservoir age of 400 years for radiocarbon ages. If the reservoir age was older than 400 years, the calculated calendar age of the IRD peaks would be younger. Analysis of core MD99-2334K on the Iberian Margin found reservoir ages changed dramatically during HS1 as a function of changing ocean ventilation and could have been as high as 1,800 years (Skinner et al., 2014). Comparison of radiocarbon ages of aligned marine core features such as $\delta^{18}O$, IRD deposition, and geomagnetic paleointensity, provided a more conservative estimate of reservoir ages in the North Atlantic during early HS1 as between 1,000-1,300 years (Lisiecki and Stern,

2013). Without using a 400-year constant reservoir age and accounting for the 600-year age uncertainty of SU81-18, the larger IRD peak found by Bard could have occurred at ~16.1 ka and be in agreement with the timing of IRD deposition found within U1308 and the precipitation shift seen in the TBR-14 record.

Another possibility for the 16.1 ka event is the rapid expansion of North Atlantic winter sea ice (Denton et al., 2010). Like IRD, sea ice extent can change dramatically over short time scales that match the rate of climate change observed at 16.1 ka. Sea ice would function similarly to the IRD forcing mechanism by increasing atmospheric pressure gradients and strengthening Northeast trade winds (Chiang et al., 2008). Winter sea ice may also be responsible for the lack of a cooling signal in Greenland oxygen isotopes during HS1 as it would trigger a decrease in precipitation that would overprint the colder temperature signal of Greenland ice cores (He et al., 2021).

Connection to Global Climate:

The TBR-14 speleothem record has been shown to precisely capture the timing of shifts in the latitudinal range of the ITCZ. The timeline of ITCZ shifts provided by TBR-14 is not only important for understanding other paleoclimate sites in the tropics and subtropics but also global climate change. During Heinrich Stadial 1, the ITCZ mediated high latitude, northern hemisphere climate forcings to all latitudes in the southern hemisphere (Denton et al., 2010; Huang et al., 2019). The resulting changes in atmospheric circulation in the southern hemisphere led to a 50-ppb increase in methane

and the ventilation of the Southern Ocean with a concomitant 12-ppm rise in CO_2 (Anderson et al; Marcott et al., 2014).

The physical impact of climatic change during HS1 in the midlatitudes of the southern hemisphere is observed through receding glaciers in New Zealand and the Chilean Lake District (Putnam et al., 2013; Denton et al., 2010). These changes coincide with an increase in opal fluxes, a proxy for upwelling, in the Southern Ocean (Anderson et al., 2009). Biogenic opal is created by marine diatoms, single-celled primary producers. The flux of biogenic opal is a function of diatom amount and diatom preservation. Anderson et al. (2009) concluded that the peaks in opal fluxes during HS1 found in three Southern Ocean sediment cores were caused by higher production and not from preservation. The greater production in the region was caused by a higher delivery of Si which was only possible from the upwelling of deep water (Anderson et al., 2009). This process is vital to understand as the enhanced upwelling of carbon-rich deepwater is thought to have caused a rise in atmospheric CO_2 (Menviel et al., 2018) which led to global warming and deglaciation (Denton et al., 2010).

Several atmospheric mechanisms have been evoked to explain the increase in upwelling in the Southern Ocean: southward displacement of the southern hemisphere westerlies (Toggweiler et al., 2006), intensified southern hemisphere westerlies (Menviel et al., 2018), and a weaker South Pacific Split Jet (Chiang et al., 2014).These mechanisms suggest that higher wind speeds would lead to a greater mixing of surface water, increased Eckman transport, and stronger eddy transport resulting in enhanced upwelling (Denton et al., 2010). Importantly, each mechanism links the change in

southern mid-latitude atmospheric circulation to a shift of the ITCZ southward and a subsequent altering of southern hemisphere Hadley circulation (Huang et al., 2019). Therefore, the precise timeline of ITCZ displacement depicted in the TBR-14 record may be useful for future studies of mid-latitude atmospheric change and upwelling during HS1.

Conclusion:

This study presents a multiproxy-based precipitation record of NE Brazil that constrains the timing and duration of the pluvial period that occurred during HS1. The pluvial period is connected to the southward displacement of the ITCZ evident by the shared structure of $\delta^{18}O$ signals of records to the south of the ITCZ coinciding with a mirrored precipitation signal north of the ITCZ. The $\delta^{18}O$ values throughout the record further support this argument. Utilizing trace element analysis and confocal banding in addition to $\delta^{18}O$, the pluvial period can be understood on both a regional and local scale. The multiproxy approach provides direct evidence for fine-scale movements of the ITCZ by revealing multiple lines of evidence for a direct relationship between changes in $\delta^{18}O$ and local climate.

The two-phased precipitation structure shown in the record's $\delta^{18}O$ was sorted into 3 sections. The first section (16.97 - 16.27 ka B.P.) was the most arid and had high interannual variability; PCP occurred extensively in the epikarst, while high interannual variability resulted in non-annual confocal banding and growth hiatuses. The ITCZ was the least displaced in Section 1 and did not always reach the cave site. Section 2 and

the bright confocal growth package (16.27 - 16.16, 16.19-16.1 ka B.P.) was the wettest time period with sustained lows in $\delta^{18}O$, a record low in PCP amount, and a regional high in P/Ca and brightness of growth bands. Double banding in growth layers is diagnostic of the southernmost extent of the ITCZ where the region received two wet seasons annually. After the confocal brightness package, Section 3 (16.1 - 15.86 ka B.P.) marks a gradual return to more arid conditions as PCP became more extensive and $\delta^{18}O$ rose.

The $\delta^{18}O$ precipitation structure is aligned closely to the ecological changes seen in NE Brazil palynological records. The correspondence between the speleothem and palynological records strengthens the interpretation of NE Brazil becoming wetter during HS1. Additionally, the TBR-14 record serves to bridge a fundamental gap in the understanding of the palynological records. These records depict forest expansion in NE Brazil during HS1, which provides essential support for the ecological bridge hypothesis but lack high-resolution dating. The U-Th dated TBR-14 record helps constrain the timing and duration of the ecological changes shown in the palynological records.

HS1 is a crucial paleoclimatic analogue for understanding modern climate change because of the event's global impact and abrupt nature. The global impact of HS1 is expressed as a shift from wet to wetter conditions in NE Brazil as China transitions from dry to drier conditions. These changes are a function of movement of the ITCZ occurring simultaneously with the weakening of the EASM in China. The abruptness of climate change during HS1 and anti-correspondence between these

distant locations is clearest during the Heinrich event at ~16.1 ka B.P., where each record contains an abrupt change in climate in just 2 years. The 2-year climatic shift is expressed as a 1.4 ‰ $\delta^{18}O$ decrease and double banding in NE Brazil simultaneously with a ~2 ‰ increase in $\delta^{18}O$ in China. The timing of the synchronous changes in both records suggests a global shift in the ITCZ and tropical precipitation in response to a massive climatic perturbation in the North Atlantic. This allows us to better understand how future high latitude perturbations might affect rainfall distribution in the tropics.

References:

Anderson, R. F., Ali, S., Bradtmiller, L. I., Nielsen, S. H. H., Fleisher, M. Q., Anderson, B. E., & Burckle, L. H. (2009). Wind-driven upwelling in the southern ocean and the deglacial rise in atmospheric CO2. *Science*, *323*(5920). https://doi.org/10.1126/science.1167441

Arz, H. W., Pätzold, J., & Wefer, G. (1998). *Correlated Millennial-Scale Changes in Surface Hydrography and Terrigenous Sediment Yield Inferred from Last-Glacial Marine Deposits off Northeastern Brazil*.

Auler, A. S., Wang, X. F., Edwards, R. L., Cheng, H., Cristalli, P. S., Smart, P. L., Richards, D. A., Auler, A. S., Wang, X., Edwards, R. L., Cheng, H., Cristalli, P. S., Smart, P. L., & Richards, D. A. (2004). Quaternary ecological and geomorphic changes associated with rainfall events in presently semi-arid northeastern Brazil. *Journal of Quaternary Science.*, *19*(7), 693–701. https://doi.org/10.1002/jqs.876

Auler, A. S., & Smart, P. L. (2003). The influence of bedrock-derived acidity in the development of surface and underground karst: Evidence from the Precambrian carbonates of semi-arid northeastern Brazil. *Earth Surface Processes and Landforms*, *28*(2). https://doi.org/10.1002/esp.443

Auler, A. (1999). *Karst evolution and palaeoclimate of Eastern Brazil*.

Baker, A., Mariethoz, G., Comas-Bru, L., Hartmann, A., Frisia, S., Borsato, A., Treble, P. C., & Asrat, A. (2021). The Properties of Annually Laminated Stalagmites-A Global Synthesis. In *Reviews of Geophysics* (Vol. 59, Issue 2). https://doi.org/10.1029/2020RG000722

Baker, A., Mockler, N. J., & Barnes, W. L. (1999). Fluorescence intensity variations of speleothem-forming groundwaters: Implications for paleoclimate reconstruction. *Water Resources Research*, *35*(2). https://doi.org/10.1029/1998WR900057

Bard, E., Rostek, F., Turon, J. L., & Gendreau, S. (2000). Hydrological impact of Heinrich events in the subtropical Northeast Atlantic. *Science*, *289*(5483). https://doi.org/10.1126/science.289.5483.1321

Bard,*'?, E., Famnanks, R., Arnold, M., Maurice, P., Duprat, J., Moyes, J., & Duplessy, J.-C. (1989). Sea-Level Estimates during the Last Deglaciation Based on 6180 and Accelerator Mass Spectrometry 14C Ages Measured in Globigerina bulloides. In *QUATERNARY RESEARCH* (Vol. 31).

Bassis, J. N., Petersen, S. v, & Cathles, L. mac. (2017). Heinrich events triggered by ocean forcing and modulated by isostatic adjustment. *Nature*, *542*(7641). https://doi.org/10.1038/nature21069

Berry, A. E. (2018). *Evidence of Late Pleistocene Heinrich Stadials in Northeastern Brazil A THESIS SUBMITTED TO THE FACULTY OF UNIVERSITY OF MINNESOTA BY*.

Behling, H., W. Arz, H., Pätzold, J., & Wefer, G. (2000). Late Quaternary vegetational and climate dynamics in northeastern Brazil, inferences from marine core GeoB 3104-1. *Quaternary Science Reviews*, *19*(10). https://doi.org/10.1016/S0277-3791(99)00046-3

Bond, G. C., & Lotti, R. (1995). Iceberg discharges into the North Atlantic on millennial time scales during the last glaciation. *Science*, *267*(5200). https://doi.org/10.1126/science.267.5200.1005

Bond, G., Heinrich, H., Broecker, W., Labeyrie, L., McManus, J., Andrews, J., Huon, S., Jantschik, R., Clasen, S., Simet, C., Tedesco, K., Klas, M., Bonani, G., & Ivy, S. (1992). Evidence for massive discharges of icebergs into the North Atlantic ocean during the last glacial period. *Nature*, *360*(6401). https://doi.org/10.1038/360245a0

Bond, G., Broecker, W., Johnsen, S., McManus, J., Labeyrie, L., Jouzel, J., & Bonani, G. (1993). Correlations between climate records from North Atlantic sediments and Greenland ice. *Nature*, *365*(6442). https://doi.org/10.1038/365143a0

Borsato, A., Frisia, S., Fairchild, I. J., Somogyi, A., & Susini, J. (2007). Trace element distribution in annual stalagmite laminae mapped by micrometer-resolution X-ray fluorescence: Implications for incorporation of environmentally significant species. *Geochimica et Cosmochimica Acta*, *71*(6). https://doi.org/10.1016/j.gca.2006.12.016

Bradley, R. S., & Diaz, H. F. (2021). Late Quaternary Abrupt Climate Change in the Tropics and Sub-Tropics: The Continental Signal of Tropical Hydroclimatic Events (THEs). In *Reviews of Geophysics* (Vol. 59, Issue 4). John Wiley and Sons Inc. https://doi.org/10.1029/2020RG000732

Broecker, W., & Putnam, A. E. (2012). How did the hydrologic cycle respond to the two-phase mystery interval? *Quaternary Science Reviews*, *57*. https://doi.org/10.1016/j.quascirev.2012.09.024

Broecker, W., Bond, G., Klas, M., Clark, E., & McManus, J. (1992). Origin of the northern Atlantic's Heinrich events. *Climate Dynamics*, *6*(3–4). https://doi.org/10.1007/BF00193540

Broecker, W., & Putnam, A. E. (2012). How did the hydrologic cycle respond to the two-phase mystery interval? *Quaternary Science Reviews*, *57*, 17–25. https://doi.org/10.1016/j.quascirev.2012.09.024

Broecker, W. S., McGee, D., Adams, K. D., Cheng, H., Edwards, R. L., Oviatt, C. G., & Quade, J. (2009). A Great Basin-wide dry episode during the first half of the Mystery Interval? *Quaternary Science Reviews*, *28*(25–26). https://doi.org/10.1016/j.quascirev.2009.07.007

Cadier, E. (1996). Small watershed hydrology in semi-arid north-eastern Brazil: basin typology and transposition of annual runoff data. *Journal of Hydrology*.

Campbell, M., McDonough, L., Treble, P., Baker, A., Kosarac, N., Coleborn, K., Wynn, P., & Schmitt, A. (2023). A Review of Speleothems as Archives for Paleofire Proxies, With Australian Case Studies. *Review of Geophysics*.

Cheng, H., Lawrence Edwards, R., Shen, C. C., Polyak, V. J., Asmerom, Y., Woodhead, J., Hellstrom, J., Wang, Y., Kong, X., Spötl, C., Wang, X., & Calvin Alexander, E. (2013).

Improvements in 230Th dating, 230Th and 234U half-life values, and U-Th isotopic measurements by multi-collector inductively coupled plasma mass spectrometry. *Earth and Planetary Science Letters*, *371–372*. https://doi.org/10.1016/j.epsl.2013.04.006

Cheng, H., Edwards, R. L., Sinha, A., Spötl, C., Yi, L., Chen, S., Kelly, M., Kathayat, G., Wang, X., Li, X., Kong, X., Wang, Y., Ning, Y., & Zhang, H. (2016). The Asian monsoon over the past 640,000 years and ice age terminations. *Nature*, *534*(7609). https://doi.org/10.1038/nature18591

Chiang, J. C. H., Fung, I. Y., Wu, C. H., Cai, Y., Edman, J. P., Liu, Y., Day, J. A., Bhattacharya, T., Mondal, Y., & Labrousse, C. A. (2015). Role of seasonal transitions and westerly jets in East Asian paleoclimate. *Quaternary Science Reviews*, *108*, 111–129. https://doi.org/10.1016/J.QUASCIREV.2014.11.009

Chiang, J. C. H., & Bitz, C. M. (2005). Influence of high latitude ice cover on the marine Intertropical Convergence Zone. *Climate Dynamics*, *25*(5). https://doi.org/10.1007/s00382-005-0040-5

Chiang, J. C. H., Biasutti, M., & Battisti, D. S. (2003). Sensitivity of the Atlantic Intertropical Convergence Zone to Last Glacial Maximum boundary conditions. *Paleoceanography*, *18*(4). https://doi.org/10.1029/2003PA000916

Chiang, J. C. H., Cheng, W., & Bitz, C. M. (2008). Fast teleconnections to the tropical Atlantic sector from Atlantic thermohaline adjustment. *Geophysical Research Letters*, *35*(7). https://doi.org/10.1029/2008GL033292

Chiang, J. C. H., Lee, S. Y., Putnam, A. E., & Wang, X. (2014). South Pacific Split Jet, ITCZ shifts, and atmospheric North-South linkages during abrupt climate changes of the last glacial period. *Earth and Planetary Science Letters*, *406*. https://doi.org/10.1016/j.epsl.2014.09.012

Costa, L. P. (2003). The historical bridge between the Amazon and the Atlantic Forest of Brazil: A study of molecular phylogeography with small mammals. *Journal of Biogeography*, *30*(1). https://doi.org/10.1046/j.1365-2699.2003.00792.x

Crivellari, S., Chiessi, C. M., Kuhnert, H., Häggi, C., da Costa Portilho-Ramos, R., Zeng, J. Y., Zhang, Y., Schefuß, E., Mollenhauer, G., Hefter, J., Alexandre, F., Sampaio, G., & Mulitza, S. (2018). Increased Amazon freshwater discharge during late Heinrich Stadial 1. *Quaternary Science Reviews*, *181*. https://doi.org/10.1016/j.quascirev.2017.12.005

Cruz, F. W., Burns, S. J., Jercinovic, M., Karmann, I., Sharp, W. D., & Vuille, M. (2007). Evidence of rainfall variations in Southern Brazil from trace element ratios (Mg/Ca and Sr/Ca) in a Late Pleistocene stalagmite. *Geochimica et Cosmochimica Acta*, *71*(9). https://doi.org/10.1016/j.gca.2007.02.005

Cruz, F. W., Karmann, I., Viana, O., Burns, S. J., Ferrari, J. A., Vuille, M., Sial, A. N., & Moreira, M. Z. (2005). Stable isotope study of cave percolation waters in subtropical Brazil: Implications for paleoclimate inferences from speleothems. *Chemical Geology*, *220*(3–4). https://doi.org/10.1016/j.chemgeo.2005.04.001

Dansgaard, W. (2012). Stable isotopes in precipitation. *Tellus A: Dynamic Meteorology and Oceanography*, *16*(4). https://doi.org/10.3402/tellusa.v16i4.8993

de Oliveira, P. E., Magnólia, A., Barreto, F., & Suguio, K. (1999). Late Pleistocene=Holocene climatic and vegetational history of the Brazilian caatinga: the fossil dunes of the middle São Francisco River. In *Palaeogeography, Palaeoclimatology, Palaeoecology* (Vol. 152).

de Oliveira, G., Araújo, M. B., Rangel, T. F., Alagador, D., & Diniz-Filho, J. A. F. (2012). Conserving the Brazilian semiarid (Caatinga) biome under climate change. *Biodiversity and Conservation*, *21*(11), 2913–2926. https://doi.org/10.1007/s10531-012-0346-7

Denton, G. H., Anderson, R. F., Toggweiler, J. R., Edwards, R. L., Schaefer, J. M., & Putnam, A. E. (2010). The last glacial termination. In *Science* (Vol. 328, Issue 5986). https://doi.org/10.1126/science.1184119

Deplazes, G., Lückge, A., Peterson, L. C., Timmermann, A., Hamann, Y., Hughen, K. A., Röhl, U., Laj, C., Cane, M. A., Sigman, D. M., & Haug, G. H. (2013). Links between tropical rainfall and North Atlantic climate during the last glacial period. *Nature Geoscience*, *6*(3). https://doi.org/10.1038/ngeo1712

Domínguez-Villar, D., Baker, A., Fairchild, I. J., & Edwards, R. L. (2012). A method to anchor floating chronologies in annually laminated speleothems with U-Th dates. *Quaternary Geochronology*, *14*. https://doi.org/10.1016/j.quageo.2012.04.019

Dupont, L. M., Schlütz, F., Ewah, C. T., Jennerjahn, T. C., Paul, A., & Behling, H. (2010). Two-step vegetation response to enhanced precipitation in Northeast Brazil during Heinrich event 1. *Global Change Biology*, *16*(6). https://doi.org/10.1111/j.1365-2486.2009.02023.x

Edwards, R. L. (1988). *High precision thorium-230 ages of corals and the timing of sea level fluctuations in the late Quaternary*.

Edwards, R., Chen, J., & Wasserburg, G. (1987). U-238-U-234-Th-230-Th-232 systematics and the precise measurement of time over the past 500,000 years. *Earth and Planetary Science Letters*.

Fairchild, I. J., Borsato, A., Tooth, A. F., Frisia, S., Hawkesworth, C. J., Huang, Y., McDermott, F., & Spiro, B. (2000). Controls on trace element (Sr-Mg) compositions of carbonate cave waters: Implications for speleothem climatic records. *Chemical Geology*, *166*(3–4). https://doi.org/10.1016/S0009-2541(99)00216-8

Fairchild, I. J., & Treble, P. C. (2009). Trace elements in speleothems as recorders of environmental change. *Quaternary Science Reviews*, *28*(5–6). https://doi.org/10.1016/j.quascirev.2008.11.007

Frisia, S., Borsato, A., Drysdale, R. N., Paul, B., Greig, A., & Cotte, M. (2012). A re-evaluation of the palaeoclimatic significance of phosphorus variability in speleothems revealed by high-resolution synchrotron micro XRF mapping. *Climate of the Past*, *8*(6). https://doi.org/10.5194/cp-8-2039-2012

Gascoyne, M. (1983). Trace-element partition coefficients in the calcite-water system and their paleoclimatic significance in cave studies. *Journal of Hydrology*, *61*(1–3). https://doi.org/10.1016/0022-1694(83)90249-4

Harris, S. E., & Mix, A. C. (1999). Pleistocene precipitation balance in the Amazon Basin recorded in deep sea sediments. *Quaternary Research*, *51*(1). https://doi.org/10.1006/qres.1998.2008

Hartland, A., Fairchild, I. J., Lead, J. R., Borsato, A., Baker, A., Frisia, S., & Baalousha, M. (2012). From soil to cave: Transport of trace metals by natural organic matter in karst dripwaters. *Chemical Geology*, *304–305*. https://doi.org/10.1016/j.chemgeo.2012.01.032

Hastenrath, S., & Heller, L. (1977). Dynamics of climatic hazards in northeast Brazil. *Quarterly Journal of the Royal Meteorological Society*, *103*(435). https://doi.org/10.1002/qj.49710343505

Hastenrath, S. (1990). Prediction of Northeast Brazil Rainfall Anomalies. *Journal of Climate*, *3*(8). https://doi.org/10.1175/1520-0442(1990)003<0893:ponbra>2.0.co;2

Haug, G. H., Hughen, K. A., Sigman, D. M., Peterson, L. C., & Röhl, U. (2001). Southward migration of the intertropical convergence zone through the holocene. *Science*, *293*(5533). https://doi.org/10.1126/science.1059725

He, C., Liu, Z., Otto-Bleisner, B., Brady, E., Zhu, C., Tomas, R., Buizert, C., & Severinghaus, J (2021). Abrupt Heinrich Stadial 1 cooling missing in Greenland oxygen isotopes. Science Advances, 7(25). http://doi/10.1126/sciadv.abh1007

Heinrich, H. (1988). Origin and consequences of cyclic ice rafting in the Northeast Atlantic Ocean during the past 130,000 years. *Quaternary Research*, *29*(2). https://doi.org/10.1016/0033-5894(88)90057-9

Hemming, S. R. (2004). Heinrich events: Massive late Pleistocene detritus layers of the North Atlantic and their global climate imprint. *Reviews of Geophysics*, *42*(1). https://doi.org/10.1029/2003RG000128

Hendy, C. H. (1971). The isotopic geochemistry of speleothems-I. The calculation of the effects of different modes of formation on the isotopic composition of speleothems and their applicability as palaeoclimatic indicators. Geochimica et Cosmochimica Acta, 35(8). https://doi.org/10.1016/0016-7037(71)90127-X

Hodell, D. A., Nicholl, J. A., Bontognali, T. R. R., Danino, S., Dorador, J., Dowdeswell, J. A., Einsle, J., Kuhlmann, H., Martrat, B., Mleneck-Vautravers, M. J., Rodríguez-Tovar, F. J., & Röhl, U. (2017). Anatomy of Heinrich Layer 1 and its role in the last deglaciation. Paleoceanography, 32(3). https://doi.org/10.1002/2016PA003028

Huang, Y., Fairchild, I. J., Borsato, A., Frisia, S., Cassidy, N. J., McDermott, F., & Hawkesworth, C. J. (2001). Seasonal variations in Sr, Mg and P in modern speleothems (Grotta di Ernesto, Italy). Chemical Geology, 175(3–4). https://doi.org/10.1016/S0009-2541(00)00337-5

Huang, J., Wan, S., Li, A., & Li, T. (2019). Two-phase structure of tropical hydroclimate during Heinrich Stadial 1 and its global implications. *Quaternary Science Reviews*, *222*. https://doi.org/10.1016/j.quascirev.2019.105900

Hulbe, C. L. (1997). An ice shelf mechanism for Heinrich layer production. Paleoceanography, 12(5). https://doi.org/10.1029/97PA02014

Hulbe, C. L., MacAyeal, D. R., Denton, G. H., Kleman, J., & Lowell, T. v. (2004). Catastrophic ice shelf breakup as the source of Heinrich event icebergs. Paleoceanography, 19(1). https://doi.org/10.1029/2003pa000890

Jaeschke, A., Rühlemann, C., Arz, H., Heil, G., & Lohmann, G. (2007). Coupling of millennial-scale changes in sea surface temperature and precipitation off northeastern Brazil with high-latitude climate shifts during the last glacial period. Paleoceanography, 22(4). https://doi.org/10.1029/2006PA001391

Jaffey, A. H., Flynn, K. F., Glendenin, L. E., Bentley, W. C., & Essling, A. M. (1971). Precision {Measurement} of {Half}-{Lives} and {Specific} {Activities} of 235Uand 238U. *Physical Review C*, *4*(5).

Jennerjahn, T. C., Ittekkot, V., Arz, H. W., Behling, H., Pätzold, J., & Wefer, G. (2004). Asynchronous terrestrial and marine signals of climate change during Heinrich events. Science, 306(5705). https://doi.org/10.1126/science.1102490

Kendall, C., & McDonnell, J. J. (1998). Isotope tracers in catchment hydrology. In *Isotope tracers in catchment hydrology*. https://doi.org/10.1029/99eo00193

Klimchouk, A., Auler, A. S., Bezerra, F. H. R., Cazarin, C. L., Balsamo, F., & Dublyansky, Y. (2016). Hypogenic origin, geologic controls and functional organization of a giant cave system in Precambrian carbonates, Brazil. *Geomorphology*, *253*. https://doi.org/10.1016/j.geomorph.2015.11.002

Klimchouk, A., Ford, D., Palmer, A., & Dreybrodt, W. (2000). Speleogenesis under deep-seated and confined settings. In *Speleogenesis: Evolution of Karst Aquifers* (pp. 244–260).

Leal, I. R., da Silva, J. M. C., Tabarelli, M., & Lacher, T. E. (2005). Changing the course of biodiversity conservation in the caatinga of northeastern Brazil. In *Conservation Biology* (Vol. 19, Issue 3, pp. 701–706). https://doi.org/10.1111/j.1523-1739.2005.00703.x

Ledru, M. P., Mourguiart, P., Ceccantini, G., Turcq, B., & Sifeddine, A. (2002). Tropical climates in the game of two hemispheres revealed by abrupt climatic change. *Geology*, *30*(3). https://doi.org/10.1130/0091-7613(2002)030<0275:TCITGO>2.0.CO;2

Li, D., Tan, L., Cai, Y., Jiang, X., Ma, L., Cheng, H., Edwards, R. L., Zhang, H., Gao, Y., & An, Z. (2019). Is Chinese stalagmite δ18O solely controlled by the Indian summer monsoon? *Climate Dynamics*, *53*(5–6). https://doi.org/10.1007/s00382-019-04671-x

Li, W. X., Lundberg, J., Dickin, A. P., Ford, D. C., Schwarcz, H. P., McNutt, R., & Williams, D. (1989). High-precision mass-spectrometric uranium-series dating of cave deposits and implications for palaeoclimate studies. *Nature*, *339*(6225). https://doi.org/10.1038/339534a0

Liang, Y., Zhao, K., Edwards, R. L., Wang, Y., Shao, Q., Zhang, Z., Zhao, B., Wang, Q., Cheng, H., & Kong, X. (2020). East Asian monsoon changes early in the last deglaciation and insights into the interpretation of oxygen isotope changes in the Chinese stalagmite record. *Quaternary Science Reviews*, *250*. https://doi.org/10.1016/j.quascirev.2020.106699

Lisiecki, L. E., & Raymo, M. E. (2005). Pliocene-Pleistocene stack of globally distributed benthic stable oxygen isotope records. *Paleoceanography.*, *20*.

MacAyeal, D. R. (1993). Binge/purge oscillations of the Laurentide Ice Sheet as a cause of the North Atlantic's Heinrich events. *Paleoceanography*, *8*(6). https://doi.org/10.1029/93PA02200

Marcott, S. A., Clark, P. U., Padman, L., Klinkhammer, G. P., Springer, S. R., Liu, Z., Otto-Bliesner, B. L., Carlson, A. E., Ungerer, A., Padman, J., He, F., Cheng, J., & Schmittner, A. (2011). Ice-shelf collapse from subsurface warming as a trigger for Heinrich events. *Proceedings of the National Academy of Sciences of the United States of America*, *108*(33). https://doi.org/10.1073/pnas.1104772108

Marengo, J. A., Torres, R. R., & Alves, L. M. (2017). Drought in Northeast Brazil—past, present, and future. *Theoretical and Applied Climatology*, *129*(3–4). https://doi.org/10.1007/s00704-016-1840-8

Martín-Chivelet, J., Muñoz-García, M. B., Cruz, J. A., Ortega, A. I., & Turrero, M. J. (2017). Speleothem Architectural Analysis: Integrated approach for stalagmite-based paleoclimate research. In *Sedimentary Geology* (Vol. 353). https://doi.org/10.1016/j.sedgeo.2017.03.003

Masson-Delmotte, V., Jouzel, J., Landais, A., Stievenard, M., Johnsen, S. J., White, J. W. C., Werner, M., Sveinbjornsdottir, A., & Fuhrer, K. (2005). Atmospheric science: GRIP deuterium excess reveals rapid and orbital-scale changes in greenland moisture origin. *Science*, *309*(5731). https://doi.org/10.1126/science.1108575

McManus, J. F., Oppo, D. W., & Cullen, J. L. (1999). A 0.5-Million-year record of millennial-scale climate variability in the North Atlantic. *Science*, *283*(5404). https://doi.org/10.1126/science.283.5404.971

Menviel, L., Spence, P., Yu, J., Chamberlain, M. A., Matear, R. J., Meissner, K. J., & England, M. H. (2018). Southern Hemisphere westerlies as a driver of the early deglacial atmospheric CO2 rise. *Nature Communications*, *9*(1). https://doi.org/10.1038/s41467-018-04876-4

Muller, J., McManus, J. F., Oppo, D. W., & Francois, R. (2012). Strengthening of the Northeast Monsoon over the Flores Sea, Indonesia, at the time of Heinrich event 1. *Geology*, *40*(7). https://doi.org/10.1130/G32878.1

Oriani, F., Treble, P. C., Baker, A., & Mariethoz, G. (2022). WICount: Geological lamination detection and counting using an image analysis approach. *Computers and Geosciences*, *160*. https://doi.org/10.1016/j.cageo.2022.105037

Orland, I. J., Bar-Matthews, M., Kita, N. T., Ayalon, A., Matthews, A., Valley, J. W., Orland, I. J., Kita, N. T., & Valley, J. W. (2009). Climate deterioration in the Eastern Mediterranean as revealed by ion microprobe analysis of a speleothem that grew from 2.2 to 0.9 ka in Soreq Cave, Israel. *Quaternary Research*, *71*(1), 27–35. https://doi.org/10.1016/j.yqres.2008.08.005

Orland, I. J., Burstyn, Y., Bar-Matthews, M., Kozdon, R., Ayalon, A., Matthews, A., & Valley, J. W. (2014). Seasonal climate signals (1990-2008) in a modern Soreq Cave stalagmite as revealed by high-resolution geochemical analysis. *Chemical Geology*, *363*. https://doi.org/10.1016/j.chemgeo.2013.11.011

Partin, J. W., Cobb, K. M., Adkins, J. F., Clark, B., & Fernandez, D. P. (2007). Millennial-scale trends in west Pacific warm pool hydrology since the Last Glacial Maximum. *Nature*, *449*(7161). https://doi.org/10.1038/nature06164

Peterson, L. C., Haug, G. H., Hughen, K. A., & Rohl, U. (2000). Rapid changes in the hydrologic cycle of the tropical Atlantic during the last glacial. *Science*, *290*(5498). https://doi.org/10.1126/science.290.5498.1947

Proctor, C. J., Baker, A., Barnes, W. L., & Gilmour, M. A. (2000). A thousand year speleothem proxy record of North Atlantic climate from Scotland. *Climate Dynamics*, *16*(10–11). https://doi.org/10.1007/s003820000077

Risi, C., Bony, S., & Vimeux, F. (2008). Influence of convective processes on the isotopic composition (δ18O and δD) of precipitation and water vapor in the tropics: 2. Physical interpretation of the amount effect. *Journal of Geophysical Research Atmospheres*, *113*(19). https://doi.org/10.1029/2008JD009943

Roberts, M. S., Smart, P. L., & Baker, A. (1998). Annual trace element variations in a Holocene speleothem. *Earth and Planetary Science Letters*, *154*(1–4). https://doi.org/10.1016/s0012-821x(97)00116-7

Roucou, P., de Aragão, J. O. R., Harzallah, A., Fontaine, B., & Janicot, S. (1996). Vertical motion changes related to North-East Brazil rainfall variability: A GCM simulation. *International Journal of Climatology*, *16*(8). https://doi.org/10.1002/(SICI)1097-0088(199608)16:8<879::AID-JOC56>3.0.CO;2-B

Shaffer, G., Olsen, S. M., & Bjerrum, C. J. (2004). Ocean subsurface warming as a mechanism for coupling Dansgaard-Oeschger climate cycles and ice-rafting events. *Geophysical Research Letters*, *31*(24). https://doi.org/10.1029/2004GL020968

Skinner, L. C., Waelbroeck, C., Scrivner, A. E., & Fallon, S. J. (2014). Radiocarbon evidence for alternating northern and southern sources of ventilation of the deep Atlantic carbon pool during the last deglaciation. *Proceedings of the National Academy of Sciences of the United States of America*, *111*(15). https://doi.org/10.1073/pnas.1400668111

Sliwinski, J. T., & Stoll, H. M. (2021). Combined fluorescence imaging and LA-ICP-MS trace element mapping of stalagmites: Microfabric identification and interpretation. *Chemical Geology*, *581*. https://doi.org/10.1016/j.chemgeo.2021.120397

Stern, J. v., & Lisiecki, L. E. (2013). North Atlantic circulation and reservoir age changes over the past 41,000 years. *Geophysical Research Letters*, *40*(14). https://doi.org/10.1002/grl.50679

Stríkis, N. M., Chiessi, C. M., Cruz, F. W., Vuille, M., Cheng, H., Barreto, E. A. D. S., Mollenhauer, G., Kasten, S., Karmann, I., Edwards, R. L., Bernal, J. P., & Sales, H. D. R. (2015).

Timing and structure of Mega-SACZ events during Heinrich Stadial 1. *Geophysical Research Letters*, *42*(13). https://doi.org/10.1002/2015GL064048

Tan, M., Baker, A., Genty, D., Smith, C., Esper, J., & Cai, B. (2006). Applications of stalagmite laminae to paleoclimate reconstructions: Comparison with dendrochronology/climatology. *Quaternary Science Reviews.*, *25*(17–18), 2103–2117. https://doi.org/10.1016/j.quascirev.2006.01.034

Toggweiler, J. R., Russell, J. L., & Carson, S. R. (2006). Midlatitude westerlies, atmospheric CO2, and climate change during the ice ages. *Paleoceanography*, *21*(2). https://doi.org/10.1029/2005PA001154

Treble, P. C., Schmitt, A. K., Edwards, R. L., McKeegan, K. D., Harrison, T. M., Grove, M., Cheng, H., & Wang, Y. J. (2007). High resolution Secondary Ionisation Mass Spectrometry (SIMS) δ18O analyses of Hulu Cave speleothem at the time of Heinrich Event 1. *Chemical Geology*, *238*(3–4), 197–212. https://doi.org/10.1016/J.CHEMGEO.2006.11.009

Treble, P., Shelley, J. M. G., & Chappell, J. (2003). Comparison of high resolution sub-annual records of trace elements in a modern (1911-1992) speleothem with instrumental climate data from southwest Australia. Earth and Planetary Science Letters, 216(1–2). https://doi.org/10.1016/S0012-821X(03)00504-1

Vidal, L., Labeyrie, L., Cortijo, E., Arnold, M., Duplessy, J. C., Michel, E., Becqué, S., & Weering, T. C. E. van. (1997). Evidence for changes in the North Atlantic Deep Water linked to meltwater surges during the Heinrich events. *Earth and Planetary Science Letters*, *146*(1–2). https://doi.org/10.1016/s0012-821x(96)00192-6

Wang, X., Auler, A. S., Edwards, R. L., Cheng, H., Cristalli, P. S., Smart, P. L., Richards, D. A., & Shen, C.-C. (2004). Wet periods in northeastern Brazil over the past 210 kyr linked to distant climate anomalies. *Nature*, *432*(7018), 740–743. https://doi.org/10.1038/nature03067

Wang, Y. J., Cheng, H., Edwards, R. L., An, Z. S., Wu, J. Y., Shen, C. C., & Dorale, J. A. (2001). A high-resolution absolute-dated late pleistocene monsoon record from Hulu Cave, China. *Science*, *294*(5550). https://doi.org/10.1126/science.1064618

Wendt, K. A., Li, X., & Edwards, R. L. (2021). Uranium-thorium dating of speleothems. *Elements (Quebec)*, *17*(2), 87–92. https://doi.org/10.2138/gselements.17.2.87

Wendt, K. A. (2015). *Heinrich Stadials recorded in Northeast Brazilian Stalagmites*.

Zhang, H., Griffiths, M. L., Chiang, J. C. H., Kong, W., Wu, S., Atwood, A., Huang, J., Cheng, H., Ning, Y., & Xie, S. (2018). East Asian hydroclimate modulated by the position of the westerlies during Termination I. *Science*, *362*(6414). https://doi.org/10.1126/science.aat9393

Supplementary Figures:

Supplemental Figure 1: Ceiling rock pendants in TBR cave are indicative of hypogenic cave formation. Picture taken by Daniel Menin.

30-40 WICOUNT

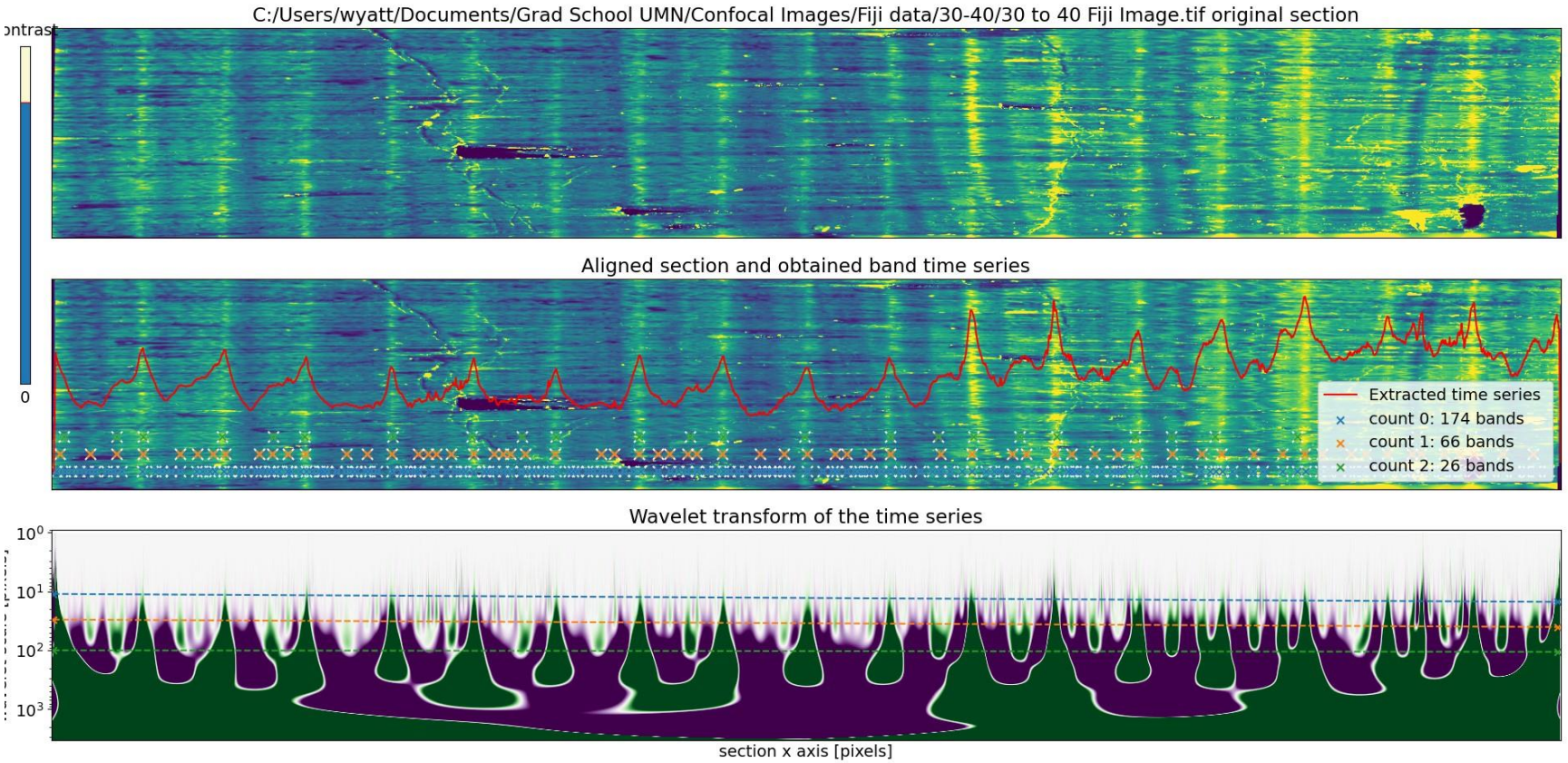

Supplementary Figure 2: Example of WICOUNT Process.

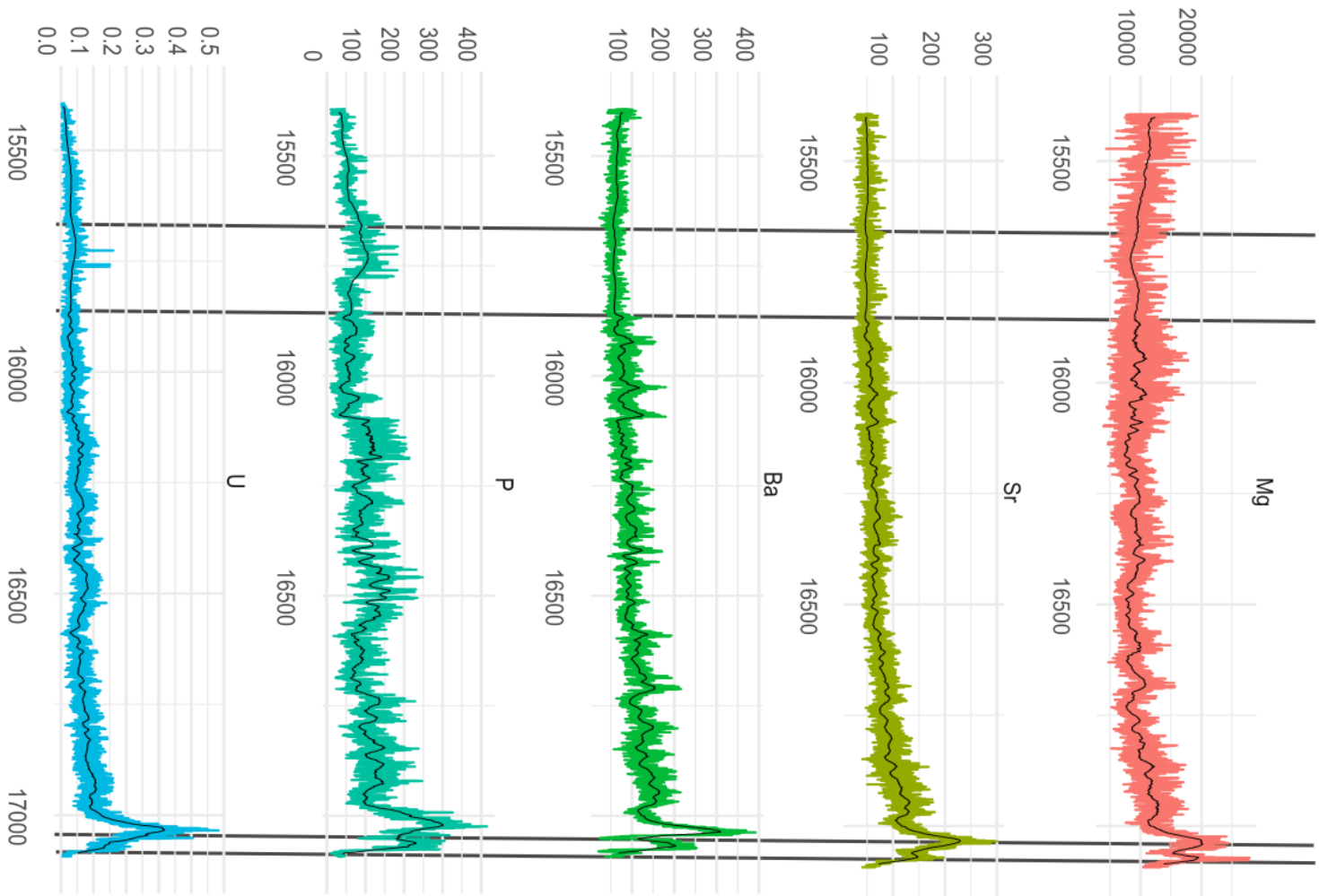

Supplemental Figure 3: Trace metal concentrations throughout the whole record

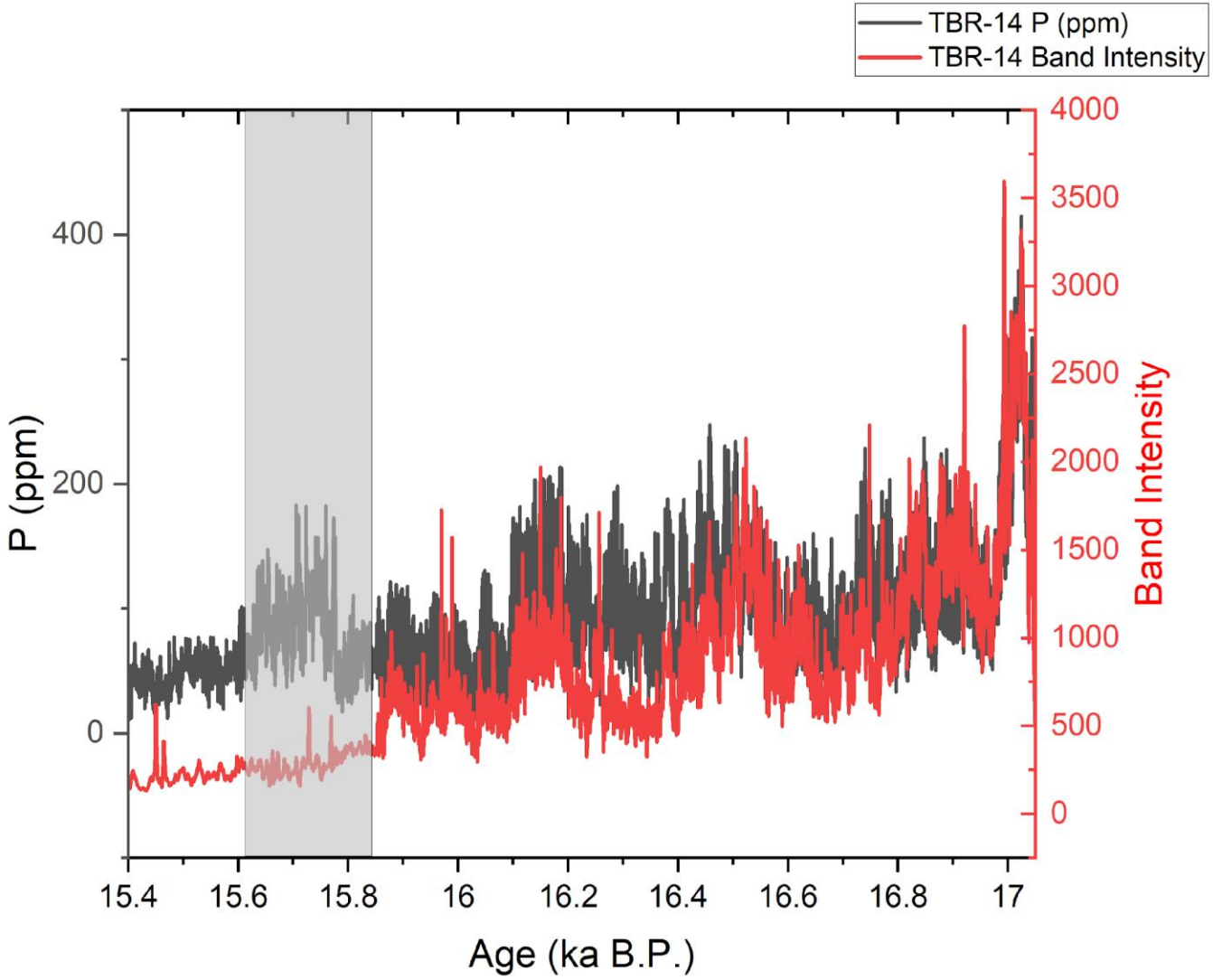

Supplemental Figure 4: Fluorescent band intensity (red) and phosphorous concentrations (black) throughout the whole record. The grey rectangle is during a hiatus and therefore cannot be interpreted.

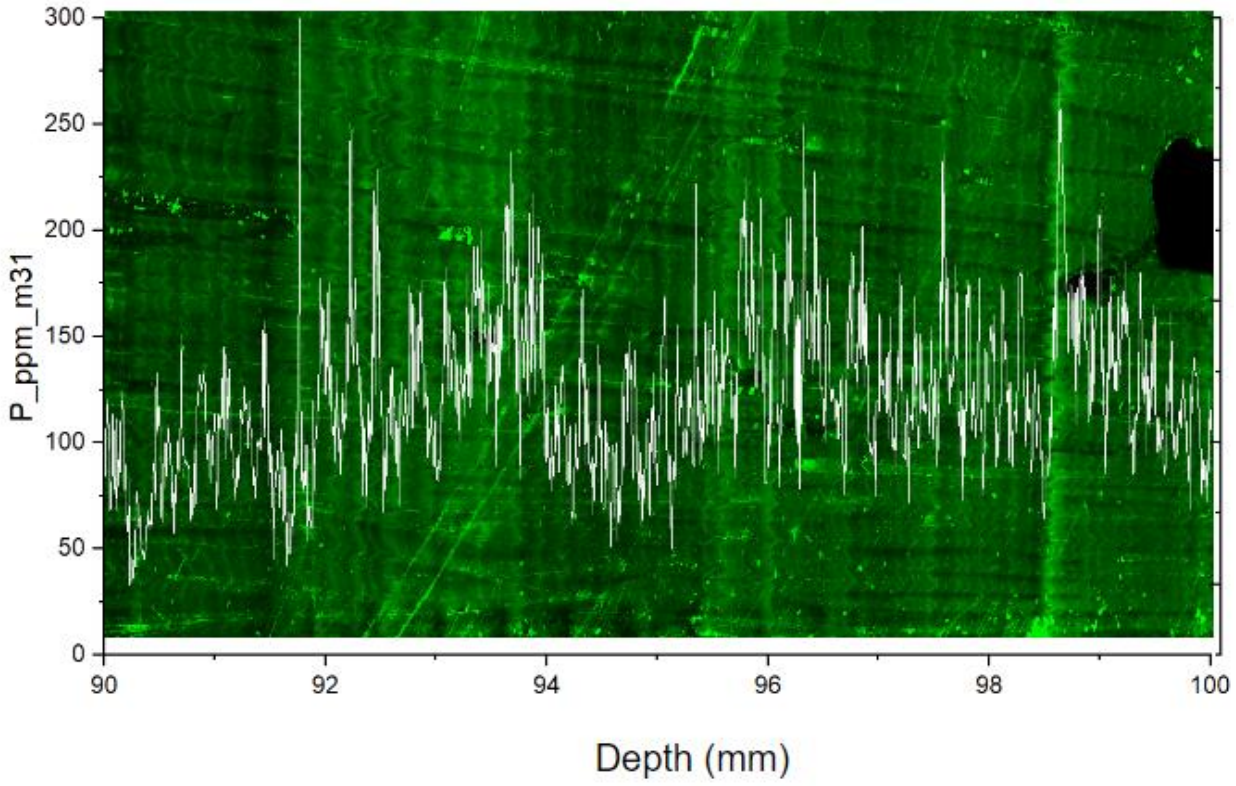

Supplemental Figure 5: Hiatus visible at 98.5 mm dft in the confocal banding image (background) and P values (white).

Supplemental Figure 6: Brighter banding in the first part of the record is partly due to loss of the annual signal. Bands blurring together result in brighter banding. Brightness is not indicative of higher rainfall in this case.

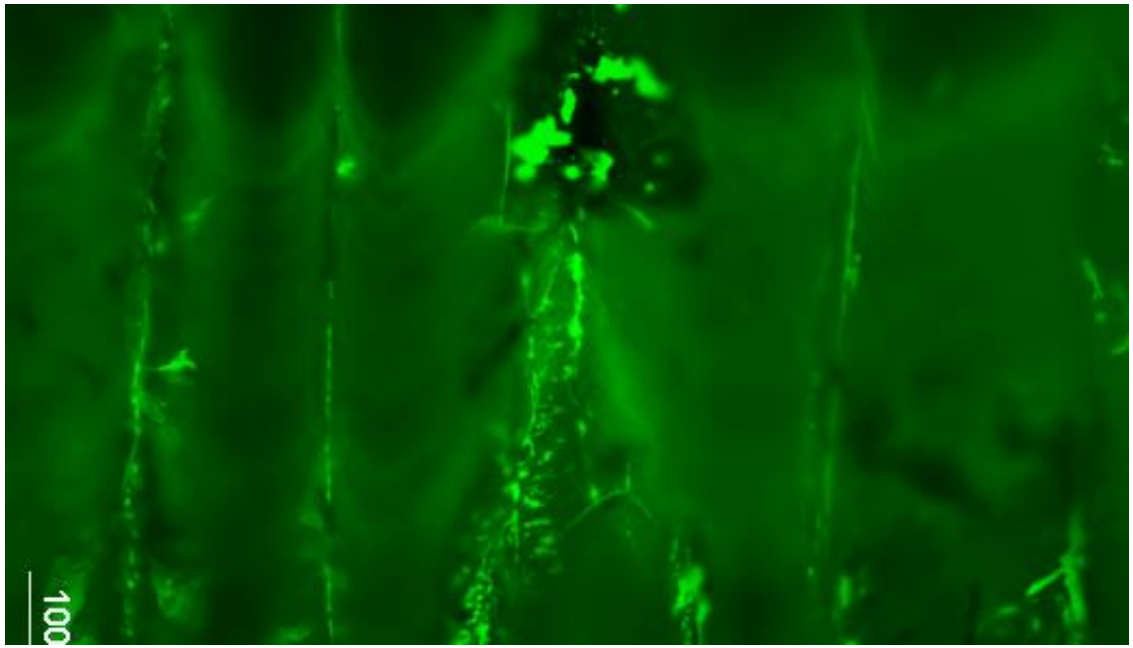

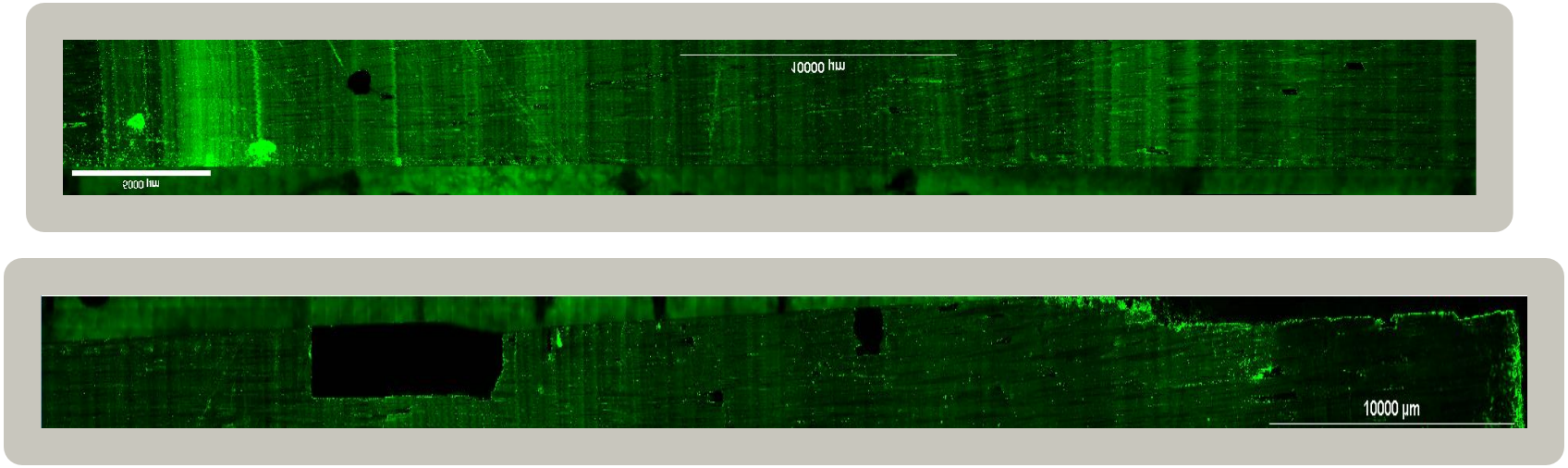

Supplemental Figure 7: Confocal Fluorescence scan of the whole TRB-14 HS1 record. Top: Composite Scan of the bottom of HS1 growth. Time is moving down the image. Top is 110 mm dft (pre-HS1 growth) and ends at 60 mm dft (~16.36 kyr B.P). Bottom: Composite scan to the top of HS1 growth and the speleothem. Top is 60 mm dft (16.36 kyr B.P.) and the bottom is 2.4 mm dft (~15.4 kyr B.P.).

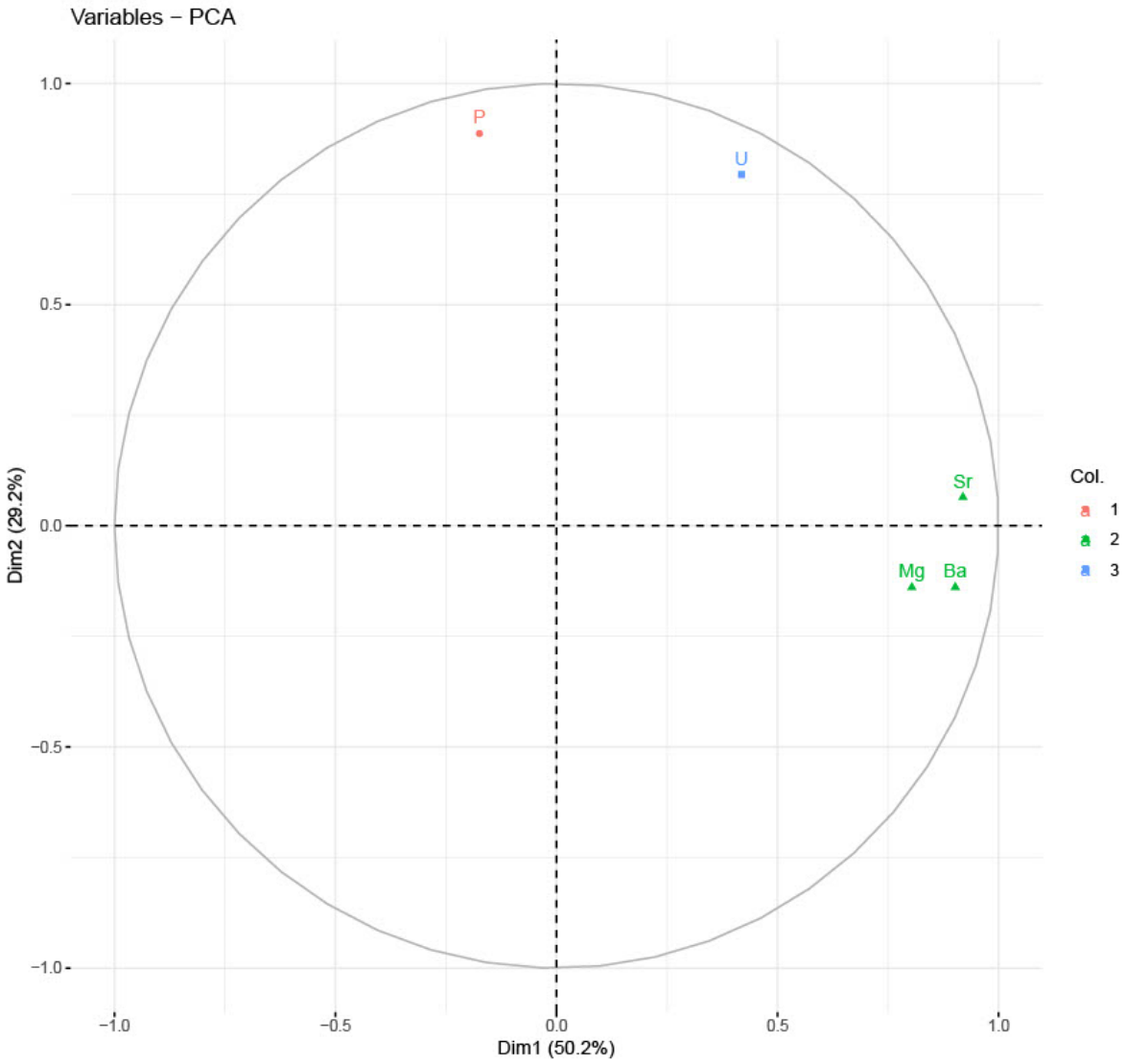

Supplemental Figure 8: Example of PCA. PCA of Section 1.